Experiments with Bose-Einstein Condensates in Microgravity

D i s s e r t a t i o n

zur Erlangung des akademischen Grades
d o c t o r r e r u m n a t u r a l i u m
(Dr. rer. nat.)
im Fach Physik
Spezialisierung: Experimentalphysik

eingereicht an der
Mathematisch-Naturwissenschaftlichen Fakultät
der Humboldt-Universität zu Berlin

von
Dipl.-Phys. Christoph Grzeschik

Präsidentin der Humboldt-Universität zu Berlin:
Prof. Dr.-Ing. Dr. Sabine Kunst

Dekan der Mathematisch-Naturwissenschaftlichen Fakultät:
Prof. Dr. Elmar Kulke

Gutachter/innen:
1. Prof. Achim Peters, Ph.D.
2. Prof. Dr. Kai Bongs
3. Prof. Dr. Heinz-Wilhelm Hübers

Tag der mündlichen Prüfung: 08.05.2017

Abstract

Atom interferometers offer the possibility to measure accelerations with unprecedented precision. Applications in fundamental research include gravitational wave detectors, the determination of physical constants, or tests of the weak equivalence principle. The sensitivity of an atom interferometer testing the weak equivalence principle scales quadratically with the time of free evolution of the atoms during the interferometer sequence. By using Bose-Einstein condensates with ultra-low expansion rates as test masses and operating the experiment in microgravity, one can enhance the sensitivity by orders of magnitude.

QUANTUS-2 is the second generation mobile atom interferometer to be operated at the drop tower in Bremen and serves as a pathfinder for future cold atom experiments in space. The high-flux atomic rubidium source is based on a $2D^+$MOT and a three-layer atom chip which allows to produce Bose-Einstein condensates with 10^5 atoms within 1 s. It is envisaged to test the weak equivalence principle by a differential measurement of the acceleration of rubidium and potassium by means of atom interferometry.

Within this thesis, the rubidium laser system was set up. It is based on micro-integrated laser modules and compact electronics. Qualification tests were performed with a dedicated capsule in two drops and seven catapult flights at the drop tower in Bremen. After integration into the QUANTUS-2 capsule, 200 drops and catapult flights were conducted at the drop tower. These are demonstrating the robustness of the complete experiment when being subjected to accelerations of up to 43 g during a catapult flight. The dynamics of the condensate were analyzed and the mean kinetic energy was reduced in all three dimensions by means of a magnetic lens, which relies on a delta-kick cooling approach. Expansion rates equivalent to a thermal ensemble having a temperature below 120 pK have been reached and represent the lowest value ever achieved in all three dimensions. The results prove the availability of relevant key concepts for future high-precision quantum sensors on a satellite platform.

Keywords: Bose-Einstein condensation, delta-kick cooling, atom interferometry, diode laser systems

Zusammenfassung

Atominterferometer erlauben es, Beschleunigungen mit bisher nicht erreichter Präzision zu messen. Anwendungen in der Grundlagenforschung beinhalten Gravitationswellendetektoren, die Bestimmung von Naturkonstanten oder Tests des schwachen Äquivalenzprinzips. Die Sensitivität eines Sensors für Tests des schwachen Äquivalenzprinzips skaliert quadratisch mit der Zeit der freien Entwicklung der Atome während der Interferometersequenz. Durch die Verwendung von Bose-Einstein-Kondensaten mit stark reduzierter Ausdehnungsgeschwindigkeit sowie dem Betrieb in Schwerelosigkeit kann die Sensitivität um Größenordnungen verbessert werden.

Das QUANTUS-2 Experiment stellt die zweite Generation eines mobilen Atominterferometers dar, welches am Fallturm in Bremen zum Einsatz kommt. Es dient als Wegbereiter für zukünftige Experimente mit kalten Atomen auf Satelliten. Die Rubidiumquelle mit einem hohen atomaren Fluss basiert auf einer $2D^+$MOT und einem dreilagigen Atomchip. Sie erlaubt eine Erzeugung von Bose-Einstein-Kondensaten mit 10^5 Atomen in 1 s. Durch differentielle Messung der Beschleunigung zwischen Rubidium und Kalium mit Hilfe der Atominterferometrie soll das schwache Äquivalenzprinzip getestet werden.

Im Rahmen dieser Arbeit wurde das auf mikro-integrierten Diodenlasern sowie einer kompakten Elektronik basierende Rubidiumlasersystem aufgebaut. Anschließend wurde das Lasersystem in einer eigenen Kapsel mit zwei Abwürfen und sieben Katapultflügen am Fallturm in Bremen qualifiziert. Nach erfolgter Integration in die QUANTUS-2 Kapsel, wurden über 200 Abwürfe und Katapultflüge am Fallturm absolviert. Diese demonstrieren die Robustheit des Experimentes unter Beschleunigungen von bis zu 43 g während eines Katapultfluges. Die Dynamik des Kondensates wurde in Schwerelosigkeit untersucht und die Ausbreitungsgeschwindigkeit in allen drei Raumrichtungen mit Hilfe einer magnetischen Linse verringert. Diese beruht auf dem Prinzip der Delta-Kick Kühlung. Die dabei erreichten Ausbreitungsgeschwindigkeiten entsprechen effektiven Temperaturen von unter 120 pK eines thermischen Ensembles. Dieser stellt den niedrigsten in allen drei Raumrichtungen erreichten Wert dar. Die gezeigten Ergebnisse demonstrieren somit die Verfügbarkeit wichtiger Schlüsselkonzepte zukünftiger hochpräziser Quantensensoren auf Satelliten.

Schlagwörter: Bose-Einstein-Kondensation, Delta-Kick Kühlung, Atominterferometrie, Diodenlasersysteme

Contents

Abbreviations

abbreviation	definition	reference
AOM	acousto-optic modulator	Sec. 4.3
ARP	adiabatic rapid passage	Sec. 5.6
BC	base chip	Sec. 3.3
BEC	Bose-Einstein condensate	Sec. 2.1
COM	center of mass	
COMM	center of mass motion	
DDS	direct digital synthesis	Sec. 4.4.1
DFB	distributed-feedback laser	Sec. 2.1
DKC	delta-kick cooling	Sec. 2.2.2
EEP	Einstein equivalence principle	Sec. 1.1
ECDL	external cavity diode laser	Sec. 4.2.1
FBH	Ferdinand-Braun-Institut	
	Leibniz-Institut für Höchstfrequenztechnik	Sec. 4.1
FPGA	field-programmable gate array	Sec. 3.2.2
HG	Hermite-Gaussian	Sec. 6.4.4
MioB	micro-optical bench	Sec. 4.2.2
MO	master oscillator	Sec. 4.2.3
MOPA	master oscillator power amplifier	Sec. 4.2.3
MOT	magneto-optical trap	Sec. 3.3
PA	power amplifier	Sec. 4.2.3
PID	proportional-integral-derivative	Sec. 4.4.1
PBS	polarizing beam splitter	
preTOF	time of flight before the lens	Sec. 6.2
PXI	PCI extensions for instrumentation	Sec. 3.2.2
QUANTUS	quantum gases in microgravity	Sec. 1.5
ROI	region of interest	Sec. 6.3
SC	science chip	Sec. 3.3
SCBC	science and base chip in conjunction	Sec. 3.3
TA	tapered amplifier	Sec. 4.2.3
TF	Thomas-Fermi	Sec. 2.1.3
TOF	time of flight	Sec. 5.3
UFF	universality of free fall	Sec. 1.1
WEP	weak equivalence principle	Sec. 1.1

1 Introduction

1.1 The search for quantum gravity

Two fundamental theories, developed in the beginning of the 20th century laid the foundation of our today's picture of the world in physics. General Relativity, which was developed by Albert Einstein, gives a mathematical interpretation of the macroscopic effects associated with gravity, while quantum mechanics as a joint effort of numerous physicists allows for a deep understanding of microscopic effects mediated by the electro-magnetic, the weak and strong interaction. Both fundamental theories have been well tested and did not show any deviation from physical reality within the sensitivity of a myriad of experiments, so far. An elementary problem arises when trying to incorporate the gravitational force within the framework of quantum mechanics. Modern theories of Quantum Gravity, such as the string theory or quantum loop theory, offer the possibility to describe the gravitational force in a unified frame. At small scales, however, they predict violations of the fundamental underlying principle of general relativity – the Einstein equivalence principle (EEP). It is therefor of fundamental interest to search for these predicted violations in order to gain evidence for potential theories of quantum gravity and discriminate between them, to find out which theory is making the better description of physical reality.

To get an understanding of the EEP, we quickly review its three basic fundamental principles [1]:

- **Universality of free fall (UFF):** The UFF, also called the "weak equivalence principle", states that all kind of structureless massive particles fall in the same way within a gravitational field – independent of their constitution and mass.
- **Local position invariance:** The local position invariance states that all kind of clocks based on non-gravitational physics behave in the same way when being transported through a non-uniform gravitational potential. The gravitational redshift, which is an effect that makes a clock on Earth tick slower than a clock in space, is a manifestation of this local position invariance.
- **Local Lorentz invariance:** The results of comparable small-scale experiments are independent of their orientation or their state of motion of the lab frame of reference. A striking consequence is the constancy of the speed of light in every lab frame – independent of its state of motion.

All these three principles have been tested in great detail without showing any hint of a violation. A strong motivation for the work carried out within this thesis originates from the search for violations of the universality of free fall. For the sake of completeness, we first describe experiments that have been carried out so far testing the other two principles before putting our focus on tests of the universality of free fall.

Experiments testing the local position invariance are based on the comparison of the ticking of two clocks at two different positions in a non-uniform gravitational potential. General relativity states that two clocks initially located at the same position and running at the same frequency ν, show a frequency difference $\Delta\nu$ when being placed apart with a difference in the gravitational potential ΔU

$$\frac{\Delta\nu}{\nu} = \frac{\Delta U}{c^2}, \tag{1.1}$$

with c being the speed of light. That is to say that a clock placed on the surface of the Earth is running slower compared to a clock in space. The most exact measurement to date comparing two clocks at a different gravitational potential has been conducted within the "Gravity Probe A" mission [2]. The frequency of two hydrogen masers, one on ground and another one being launched up to a height of 10 000 km with a rocket, has been compared to a relative uncertainty of 7×10^{-5}. Together with another series of experiments, comparing the frequency of hydrogen masers with separate cesium and rubidium fountain clocks over a time of eight years, no evidence for a violation has been found yet [3].

One of the first notable scientific experiments yielding a strong evidence for the constancy of the speed of light and thus hinting to the local Lorentz invariance was the Michelson-Morley experiment, first carried out in 1881 [4]. Modern experiments have been conducted by measuring the anisotropy of light by comparing the frequency difference between two lasers locked to two orthogonal rotating optical cavities. Results showing the anisotropy of the speed of light down to a level of $\Delta c/c \sim 1 \times 10^{-17}$ have been achieved [5].

Testing the universality of free fall

To test the weak equivalence principle, one needs to measure the differential acceleration $a_1 - a_2$ between two different test masses initially located at the same spacetime coordinate. The figure of merit that expresses to which level the universality of free fall holds, is the so-called Eötvös ratio. It was named after Loránd Eötvös, who first used torsion balance experiments to test the weak equivalence principle, and is zero if it holds [6]:

$$\eta = 2\left|\frac{a_1 - a_2}{a_1 + a_2}\right|. \tag{1.2}$$

First known experiments testing the weak equivalence principle were conducted by Galileo Galilei who compared the motion of two different test masses rolling down an inclined plane. Modern tests have been performed by comparing the acceleration of a beryllium and titanium mass in a torsion balance setup testing the weak equivalence principle to an uncertainty of $\eta = 0.3(18) \times 10^{-13}$ [7]. Another approach has been taken by comparing the free fall of Earth and Moon towards the sun by measuring the distance between the Moon and Earth [8]. Retroreflectors placed on the Moon within the Apollo missions allow for a measurement of the distance between Moon and Earth. The calculated acceleration of both celestial bodies towards the sun can be used to test the universality of free fall. So far, no evidence for any violation of the equivalence principle has been found ($\eta = 0.8(13) \times 10^{-13}$).

All these experiments rely on the use of classical test masses. In contrast to these, a new field of research gained widespread interest. It is making use of cold atomic ensembles as test masses. In the following section we will introduce how atom interferometry can make use of cold atoms to measure the differential acceleration between two different isotopes using quantum effects. Afterwards, we will show that Bose-Einstein condensates are an excellent choice as an input state for atom interferometry. We will then argue that by conducting experiments in space, the precision of an experiment searching for violations of the universality of free fall can be pushed to yet unprecedented levels. Finally, the QUANTUS collaboration will be introduced, which is conducting research in this field and is the subject of this thesis.

1.2 Atom interferometry

The onset of interference when overlapping two coherent electro-magnetic waves has given rise to numerous technical applications as well as experiments investigating fundamental questions of physics. In 1960, the advent of the laser as a source for light with pronounced spatial and temporal coherence has given a remarkable boost in the field of interferometry. The Michelson-Morley interferometer demonstrating the isotropy of the speed of light and the gravitational wave detector LIGO, which was for the first time directly measuring the existence of gravitational waves [9], are two of the most prominent examples for seminal experiments relying on optical interferometers .

While these experiments are based on the interference of electro-magnetic waves, another class of interferometers has become an important mean especially in fundamental research. IT makes use of the wave nature of massive particles, which becomes evident at low temperatures. French physicist and later Nobel laureate Louis de Broglie proposed in 1924 the wave-particle duality, stating that all matter, apart from showing a particle behavior, also exhibits a wave character [10]. The wavelength of the matter wave, according to de Broglie's hypothesis, is given as the ratio of the Planck constant

h to the particle's momentum p

$$\lambda = \frac{h}{p}. \tag{1.3}$$

One of the first experimental setups that demonstrated the interference of massive particles, was a neutron interferometer. Silicon crystals were used for the diffraction of the neutron matter wave. The interferometer was used by Colella et al. in 1975 to measure the gravitational field [11]. A recreation of Young's double slit experiment was shown by Carnal et al. in 1991. It demonstrated interference of a hot beam of metastable helium behind a micro-fabricated structure [12]. Interference of biomolecules as well as fluorofullerene molecules consisting of 108 atoms has been shown behind a gold grating by Hackermüller et al. in 2003 [13]. In the following, however, we will put the focus on atom interferometers based on light pulses.

Light pulse atom interferometer

Interferometers based on the diffraction of atoms by pulses of light were developed in the beginning of the 90's. We will describe the basic principle of operation by looking at a gravimeter described by Kasevich in 1992 [14], followed by some examples of atom interferometer experiments and their application in fundamental physics as well as in geodesy.

A sample of cold atoms is prepared within a vacuum chamber. The temperature has to be low enough so that the wave nature of the atoms is becoming resolvable. Sufficient low temperatures in the lower microkelvin regime are easily reachable for alkali atoms using laser cooling techniques such as a three-dimensional magneto-optical trap [15] and an optical molasses [16].[1] A typical Mach-Zehnder atom interferometry sequence for measuring accelerations, like for example the gravitational acceleration, is depicted in Fig. 1.1. The prepared atomic ensemble is subjected to counter-propagating laser pulses having wave vectors $k_1 = 2\pi/\lambda_1$ and $k_2 = 2\pi/\lambda_2$ with λ being the respective wavelength. These are driving two-photon transitions that are coupling two hyperfine ground state levels $|1\rangle$ and $|2\rangle$ in a Raman scheme via an intermediate excited level. When a transition to another internal state occurs, the momentum of the atom is changed by $2\hbar k_{\text{eff}} = 2\hbar(k_1 + k_2)$ due to the absorption and subsequent stimulated emission of one photon from each light field. While being illuminated by the counter-propagating beams, the transition probability between the two ground states $|1\rangle$ and $|2\rangle$ coupled by the two-photon transition is undergoing so-called Rabi oscillations [18]. By tuning the pulse duration, one can selectively excite and transfer momentum to all atoms using a so-called π-pulse. It is also possible to excite and transfer momentum to half of the atoms, which in turn is called a $\pi/2$-pulse. Since a $\pi/2$-pulse is creating a coherent superposition of two states with a different internal state and momentum,

[1] In 1997 the Nobel Prize in Physics was awarded to Steven Chu, Claude Cohen-Tannoudji and William D. Phillips for the development of the fundamental laser cooling techniques [17].

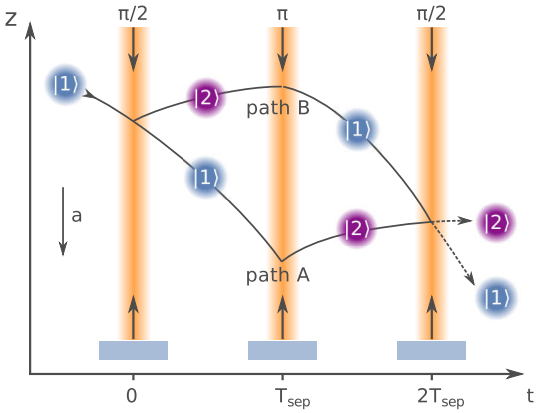

Figure 1.1: Mach-Zehnder atom interferometer for measuring an acceleration a: three laser pulses equally spaced by a time T_{sep} with the effective wave vector $k_{\text{eff}} = k_1 + k_2$ serve as beam splitters and mirror. These transfer a momentum $\hbar k_{\text{eff}}$ and change the internal state of half ($\pi/2$-pulse) or all of the atoms (π-pulse). After recombination, the relative population in the two output ports depends on a phase shift $\Delta\Phi = k_{\text{eff}} a {T_{\text{sep}}}^2$ accumulated between the two interferometer paths A and B.

it is referred to as a beam splitter, whereas a π-pulse is called a mirror pulse since it changes the momentum and internal state of all atoms.

There are two distinct types of light pulse atom interferometers that are using different atomic transitions. When driving two-photon transitions in a Raman scheme between two different hyperfine ground states via an intermediate excited level, the momentum state is becoming coupled to the internal state. This scheme is referred to as Raman interferometry with internal state labeling [19]. It is also possible to transfer momentum to the atoms by driving a two-photon transition between the same hyperfine ground state. This is referred to as Bragg interferometry [20]. For the further description, we will focus on Raman interferometry.

In a Mach-Zehnder interferometer scheme, a first $\pi/2$-pulse at $t = 0$ generates a coherent superposition of two momentum states $|1, \mathbf{p}\rangle$ and $|2, \mathbf{p} + \hbar\mathbf{k}_{\text{eff}}\rangle$, thus creating two internally state-labeled interferometer arms. The clouds in the two interferometer arms are then spatially separating because of the difference in momentum. A π-pulse after a time T_{sep} is used to recombine the two interferometer arms while also flipping the internal state between both arms. A final $\pi/2$-pulse at $t = 2T_{\text{sep}}$ overlaps the two output ports at the end of the interferometer sequence. The internal state population $P_{|2\rangle}$ in each output port then depends on a phase shift $\Delta\Phi$ between the two interferometer arms

$$P_{|2\rangle} = \frac{1}{2}(1 - C\cos\Delta\Phi), \tag{1.4}$$

with C being the contrast of the interferometer. The phase shift is arising from contributions of the free evolution between the laser pulses, a term stemming from the interaction of the atoms with the laser pulses and a contribution from a possible insufficient overlap of the two output ports at the end of the sequence:

$$\Delta\Phi = \Delta_{\text{free}} + \Delta_{\text{laser}} + \Delta_{\text{sep}}. \tag{1.5}$$

Δ_{free} is zero for a constant acceleration a [21]. When neglecting the term Δ_{sep}, the overall phase shift only depends on the interaction with the laser fields

$$\Delta\Phi = (k_{\text{eff}}a - \alpha){T_{\text{sep}}}^2, \tag{1.6}$$

with a being a constant acceleration, for example due to gravity [14]. The factor α is the chirp rate of the frequency difference between the two counter-propagating lasers during the interferometer sequence and is necessary to compensate for the Doppler shift. It is now possible to adjust the chirp rate α to tune the phase shift to zero. The acceleration a can be then calculated from the chirp rate using Eqn. (1.6).

Applications

The scheme described above is typically used for measuring an acceleration exerted on the atoms. To be more precise, it is measuring the projection of the acceleration onto the direction of the light beams. In this sense, depending on the orientation of the atom interferometer, one can measure the gravitational acceleration when aligning the beams vertical. The absolute value of the gravitational acceleration has been measured with an uncertainties $\Delta g/g \approx 3 \times 10^{-9}$ with an atomic fountain setup gravimeter [22]. Mobile apparatus have been developed [23] and commercial transportable gravimeter setups are available [24, 25]. Applications in geodesy include the determination of the absolute local gravitational field to unprecedented levels for analyzing the constitution of the Earth crust below. Rotations of the experimental setup can be measured by using a Sagnac-like interferometer topology. Sensitivities of up to 6.1×10^{-7} rad/s $\text{Hz}^{-1/2}$ have been measured [26]. By operating two gravimeters in a differential setup it is also possible to measure gravity gradients [27].

All these interferometers serve as novel instruments for geodesy and inertial sensing. On the other hand, atom interferometers find many applications in fundamental physics. By measuring the recoil velocity of atoms after interaction with a laser light field, the fraction h/m can be measured, whereas h is the Planck constant and m the mass of the atom. This is especially interesting since it can be related to the fine structure constant α, which is of now a fundamental constant but might be subject to fluctuations. The value of the fine structure constant has been determined with a relative uncertainty of 6.6×10^{-10} [28]. A gravity gradiometer can be also used to measure the Newtonian gravitational constant G [29]. There also exist proposals to use atom interferometers for detecting gravitational waves [30, 31]. The research concerning gravitational waves has gained a lot of attention after their first direct observation with the laser interferometer LIGO in 2016 [9].

As already mentioned, atom interferometers can be correlated to each other for differential measurements. It is possible to correlate two interferometers using different atomic species and measuring their differential acceleration to test the universality of

free fall. To this end, two cold ensembles of different atomic species are prepared in a common setup. These are then interrogated simultaneously with individual laser pulses to measure the differential acceleration between both species. In such a setup, common-mode noise sources and phase contributions arising mostly from vibrations are strongly suppressed [32].

Sensitivity and limitations

The sensitivity of a differential atom interferometer is given by [33]:

$$\Delta a = \sqrt{\frac{2t_c}{N}} \frac{1}{C k_{\text{eff}} {T_{\text{sep}}}^2}. \tag{1.7}$$

From this we can deduce the important aspects we have to keep in mind, when constructing an experimental apparatus for high-precision measurements:

- **Cycle time $\mathbf{t_c}$:** The precision can be increased by averaging over many cycles. It is desired to reduce the time needed for a single measurement. A fast preparation of the atomic ensemble is thus mandatory.
- **Atom number N:** According to the shot noise limit, the sensitivity scales with $1/\sqrt{N}$. It is therefor not only necessary to produce the atomic ensemble in a rapid fashion but also with a high atom number.
- **Contrast of the measurement C:** The interferometer contrast is depending largely on the beam splitter efficiency. Due to the spatial distribution of the atomic ensemble, the cloud is experiencing a spatially dependent Rabi frequency along the transversal beam profile of the laser pulses. As a consequence, only a fraction of the atoms experiences a perfect beam splitter or mirror pulse. Furthermore, due to the finite momentum width of the atomic ensemble, not all atoms are in resonance with the two-photon transition. Thus, a reduction of the size and momentum width of the atomic sample is beneficial [34].
- **Effective wave vector $\mathbf{k_{eff}}$:** An increase in momentum transfer during the laser pulses yields an increase of the area covered between the two interferometer arms and thus an increase in sensitivity. When using Bragg transitions, it is possible to transfer more than just two photon recoil momenta by using high-order transitions [35]. The efficiency of these large momentum beam splitters is again depending critically on the momentum width and size of the atomic sample. Furthermore, the enclosed interferometer area between both arms can be enlarged, for example, by using techniques like Bloch oscillations [36].
- **Pulse separation time $\mathbf{T_{sep}}$:** By Prolonging the pulse separation time, the enclosed interferometer area can be enlarged. This leads to an increase of the sensitivity which scales $\propto {T_{\text{eff}}}^2$.

One of the biggest limitations when testing the universality of free fall with a dual-species atom interferometer operating on ground is the pulse separation time T_{sep}. In Sec. 1.4 we will show that this limitation can be overcome by conducting such experiments in microgravity. Furthermore, the momentum width of the atomic ensemble is limiting the maximum pulse separation time because of the ballistic expansion of the ensemble reducing the interferometer contrast. It is therefor desired to reduce the mean kinetic energy of the ensemble to a minimum. As we will show in the next section, a Bose-Einstein condensate represents an excellent input state for atom interferometry with pulse separation times of several seconds since it offers two advantages: a small initial size and reduced momentum width.

1.3 Bose-Einstein condensation

The phenomenon of Bose-Einstein condensation was first described by Albert Einstein in 1924 after applying the theory of photon statistics developed by Satyendranath Bose to a gas of non-interacting massive bosons [37, 38].[2] Albert Einstein stated that once the temperature would drop below a specific critical temperature, a macroscopic number of particles would occupy the lowest energy single-particle state.

A descriptive explanation of the phenomenon is shown in Fig. 1.2. Starting with a number of massive particles trapped within a box at room temperature, we can describe the thermodynamic properties by treating it as an ideal gas. The particles are interacting via elastic collisions with each other as well as with the walls. A decrease in temperature is then understood as a reduction of the mean kinetic energy of the particles. As stated in Sec. 1.2, every particle can also be described as a matter wave with the wavelength $\lambda = h/p$. For the non-relativistic case we can express the wavelength in terms of the temperature T of the ensemble as the thermal de Broglie wavelength

$$\lambda_{\mathrm{dB}} = \frac{h}{\sqrt{2\pi m k_B T}}. \tag{1.8}$$

The process of Bose-Einstein condensation is manifesting when the temperature is lowered to a level at which the thermal de Broglie wavelength is becoming comparable with the interparticle spacings $(V/N)^{1/3}$, whereas N is the number of particles trapped in a volume V. At this point the wave packages start to overlap. The overlap increases when lowering the temperature further. Below a critical temperature T_c, more and more atoms will occupy the ground state when asymptotically approaching $T = 0$. The individual atoms lose their identity and can be expressed mathematically in terms of a single ground state wave function. The Pauli exclusion principle is ruling out the possibility that two fermions are occupying the same quantum-mechanical state. As a

[2] Every particle can be attributed to either of two classes: fermions having a half-integer spin and bosons having an integer spin.

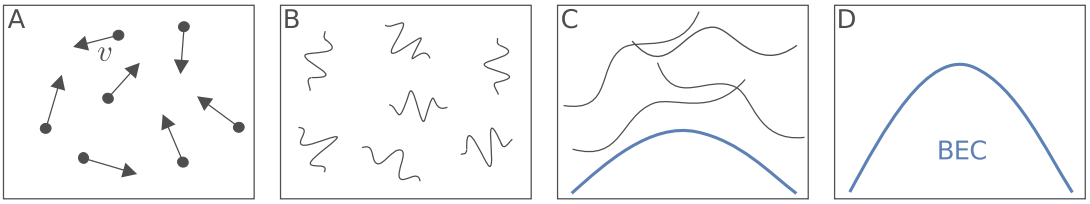

Figure 1.2: Transition from a kinetic gas to a Bose-Einstein condensate: (A) Classical ideal gas at room temperature. The atoms are moving around with a mean velocity v. (B) When cooling down the gas, the wave nature of the particles becomes apparent. Each particle can be represented as a wave packet having a de Broglie wavelength of $\lambda_{\mathrm{dB}} = h/mv$. (C) Further decrease of the temperature close to the critical temperature T_c increases the wavelength of the particles. They start to overlap and populate the ground state (blue). (D) At $T = 0$ all particles are condensed into the ground state forming a macroscopic matter wave – the Bose-Einstein condensate. (adapted from [39])

consequence, only bosons are able to undergo Bose-Einstein condensation at ultra-low temperatures.

Although the theory of this phenomenon has been already discovered in 1924, it took over 70 years to experimentally proof its existence. In 1938, Fritz London suggested a connection between superfluidity of liquid helium and Bose-Einstein condensation [40]. But because of the density in liquid Helium being very high, particle interactions would only allow for a very small part of the atoms being accommodated in the ground state. Another candidate for Bose-Einstein condensation was spin-polarized hydrogen, as proposed by Hecht in 1959 [41]. Interactions between the gaseous hydrogen atoms with their spin aligned would reduce to a minimum. Important techniques such as evaporative cooling of magnetically trapped atoms were developed within the research concerning spin-polarized hydrogen. With the advent of laser cooling in the 1980's, it became possible to make a great step towards achieving Bose-Einstein condensation in dilute gases of alkali atoms with a strong occupation of the ground state.

Laser cooling offered an extremely fast and efficient way to lower the temperature of atoms down into the microkelvin regime. But it is inherently limited in its minimal temperature by the radiation pressure and photon recoil limit [42]. The technique of evaporative cooling, which was already used in the experiments with spin-polarized hydrogen, opened the gate to temperatures within the nanokelvin regime. By applying radio-frequency driven evaporation, precooled atoms could be removed selectively from a magnetic trap [43]. Through progressively "cutting" away more and more of the hottest atoms and subsequent rethermalization, the phase space density could be increased to a level of onset of the Bose-Einstein condensation. The first observations have been achieved in 1995 by the Wiemann and Cornell group (JILA, Boulder) for rubidium [44], the Ketterle group (MIT, Boston) for sodium [45] and for spin-polarized lithium (Rice University, Houston) [46]. A picture of the onset of Bose-Einstein con-

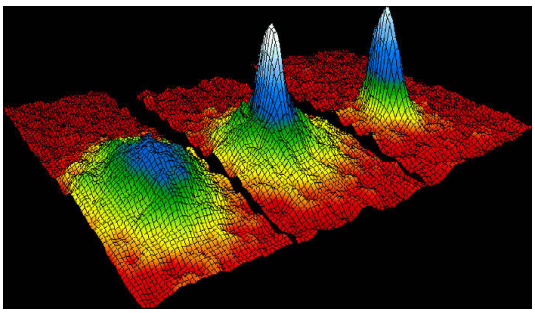

Figure 1.3: Density profiles of atomic samples showing the onset of Bose-Einstein condensation: Pictures were taken with decreasing temperature from left to right. The emergence of a sharp central peak within the thermal background is a clear evidence of Bose-Einstein condensation. Due to the minimal energy of the atoms in the ground state, the velocity distribution after release from the trap is causing a bimodal profile. (taken from JILA/NIST [48])

densation is shown in Fig. 1.3 in which the emergence of a sharp peak within a background of thermal atoms provides evidence for Bose-Einstein condensation. This peak arises from the narrow momentum width of the atoms in the ground state. In 2001, Eric A. Cornell, Wolfgang Ketterle and Carl E. Wiemann were awarded with the Nobel Prize in Physics for the first achievement of Bose-Einstein condensation in dilute gases of alkali atoms and first fundamental studies of its properties [47].

The experimental realization of Bose-Einstein condensation has shed light onto a new interesting field of quantum physics. Additionally, a BEC offers some features that are interesting for atom interferometry. Due to its narrow velocity distribution and small size, a Bose-Einstein condensate offers the possibility to improve beam splitter efficiencies and thus increase the contrast of an atom interferometer based on light pulses [34]. Because of the low expansion rate of the cloud, interrogation times of multiple seconds become feasible. Thanks to the compact size of a BEC, systematic effects arising from the cloud sampling spatially dependent wavefront aberrations are reduced. On the other hand, inter-atomic interactions in the dense ensemble can lead to additional systematic phase shifts in an atom interferometer. Furthermore, a BEC experiment features a higher level of complexity and lower atomic flux. Therefor, one has to find a reasonable trade-off when planning an experiment.

1.4 From ground-based experiments to space

The following section will give an overview of the current status of experiments testing the equivalence principle on ground and how they can benefit from a microgravity environment. Recently proposed missions aiming towards space operation will be introduced and are compared with state-of-the-art lab experiments. A list with such experiments can be found in Tab. 1.1.

Today's most precise measurements searching for violations of the UFF have been conducted using classical test masses. By measuring continuously the acceleration difference of beryllium and titanium test masses towards common reference masses at a variety of distances in a torsion balance experiment, a value of the Eötvös parameter

experiment	location	test masses	η	ref.
lunar laser ranging	lab	Earth, Moon	$0.8(13) \times 10^{-13}$	[7]
torsion balance	lab, Seattle	Be, Ti	$0.3(18) \times 10^{-13}$	[49]
AI vs. classical	lab, Stanford	^{133}Cs, FG5	$7.0(7) \times 10^{-9}$	[21]
ICE	0g airplane	^{39}K, ^{87}Rb	$0.9(30) \times 10^{-4}$	[50]
ATLAS	lab, Hannover	^{39}K, ^{87}Rb	$0.3(54) \times 10^{-7}$	[51]
10m fountain	lab, Wuhan	^{85}Rb, ^{87}Rb	$0.28(30) \times 10^{-7}$	[52]
MICROSCOPE	satellite	Ti, Pt/Rh	10^{-15}	[53]
10m fountain	lab, Stanford	^{85}Rb, ^{87}Rb	1.0×10^{-15}	[54]
VLBAI	lab, Hannover	^{87}Rb, ^{170}Yb	7×10^{-13}	[55]
QTEST	ISS	^{85}Rb, ^{87}Rb	5×10^{-16}	[56]
STE-QUEST	satellite	^{85}Rb, ^{87}Rb	2×10^{-15}	[57]
Galileo Galilei	satellite	TBD	10^{-17}	[58]

Table 1.1: Experiments testing the universality of free fall. Current experimental results are listed in the upper part, while planned or proposed experiments can be found in the lower part. Experiments utilizing atom interferometers (AI) are printed in bold face. Future missions are increasingly aiming for satellite missions.

of $\eta = 0.3(18) \times 10^{-13}$ could be measured [7]. Another classical test is done by lunar laser ranging. Evaluating the rate of fall of the Earth and the Moon towards the Sun by measuring the distance between the Moon and Earth with the help of retroreflector mirrors placed on the Moon during the Apollo missions, a value of $\eta = 0.8(13) \times 10^{-13}$ could be achieved [49]. Lunar laser ranging and the torsion balance experiment still represent the most precise tests of the UFF.

Atom interferometers in space promise to trump the sensitivity of current experiments by orders of magnitude. First measurement setups are already testing the equivalence principle on ground using dual-species atom interferometry. Values of $\eta = 0.3(54) \times 10^{-7}$ have been achieved by dropping two different cold atomic species clouds of ^{39}K and ^{87}Rb and measuring their differential acceleration [51, 52]. The sensitivity of these ground-based tests is limited by gravity, which is putting a stringent limit on the maximum time of free evolution. To circumvent this problem to a certain degree, atomic fountain setups have been conceived, using up to 10 m high vacuum drop tubes and launching the atoms from the bottom to increase the time of free evolution [52, 54]. Future ground-based experiments could possibly rely on a trapped interferometer scheme. An approach with strontium atoms using Bloch oscillations to hold the atoms against gravity in the middle of the interferometer sequence has been shown lately [59].

Microgravity offers an enhancement of the time of free evolution in an atom interferometer way beyond the reach of typical lab experiments. The potential trapping the atoms is no longer affected by the gravitational sag and therefor, lower trap fre-

quencies are possible in microgravity and allow for a further reduction of the mean kinetic energy of the ensemble by adiabatic decompression of the trap [60]. A further reduction of the expansion rate of the atomic ensemble is possible using a "delta-kick cooling" approach [61]. By pulsing on the initial trapping potential quickly some time after the release of the atoms from the trap, it is possible to reduce the kinetic energy of the ensemble while conserving the atom number. This short pulse creates a lensing force. Terms like beam quality, coma and astigmatism, typically used in geometrical optics, find their representation when collimating the expansion of a matter wave. The term "magnetic lens" is used to describe the technique of manipulating the shape of cold atom ensembles using magnetic fields. In a typical lab experiment, the atoms are falling away from the trapping potential after the release and thus, a magnetic lens on ground features only a limited performance. In microgravity, however, ultra-low expansion rates in all three dimensions can be reached due to the better overlap of the position of the lensing potential and the atomic ensemble.

Another advantage when conducting experiments in microgravity is arising from the fact that when trapping two different species in a common trap in a lab environment, the minimum position of the trap differs for both species due to their different mass. The initial collocation can be enhanced in a dual-species atom interferometer in microgravity. Finally, using a retroreflection atom interferometer setup in microgravity leads to a double diffraction scheme, which not only enhances the momentum transfer but also suppresses interferometer noise and systematic uncertainties [62, 63, 64].

A series of microgravity experiments have been proposed so far. Different platforms are available, each offering specific advantages. Drop towers, for example, are installations allowing to drop an experiment capsule from multiple tens of meters and recapturing it safely at the bottom of the tower. One of the few towers in the world is operated by the Center of Applied Space Technology and Microgravity (ZARM) in Bremen. It not only offers the possibility to drop the experiment from a height of 110 m but also allows for catapulting it to achieve a microgravity time of up to 9 s. During the flight, residual accelerations are preferably low at a level of 10^{-5} g, while repetition rates are low due to the fact that the drop tube has to be evacuated for each drop. As a consequence, only few drops can be conducted per day. Another possibility to conduct experiments in microgravity are parabolic flights with an airplane. Although parabolic flights offer a decent repetition rate of about 90 parabolas per session, each having a microgravity duration of about 20 s, they suffer from high vibrational noise at a level of about 10^{-2} g [65]. The interferometer contrast is limited by the vibrations of the setup, but a reconstruction of the fringe is possible to a certain level by measuring the vibrations with an additional accelerometer. Values of $\eta = 0.9(30) \times 10^{-4}$ have been reached lately in a dual-species atom interferometer testing the UFF on parabola flights with a plane [50].

To circumvent the problems connected with a limited microgravity time and vibrational noise, a transition to experiments operated on a satellite platform is desired. The

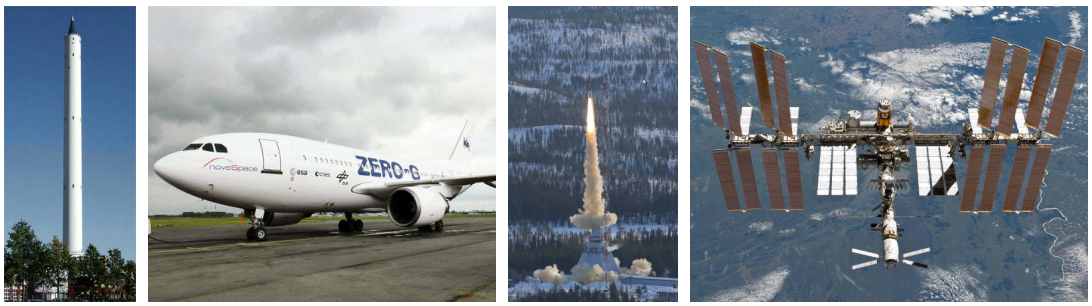

Figure 1.4: Examples of microgravity platforms: drop tower [66], zero-g Airbus A310 [67], sounding rocket [68], International Space Station ISS [69].

Space-Time Explorer and Quantum Equivalence Principle Space Test (STE-QUEST) is a proposal for a satellite-based test of general relativity [57]. It includes an atomic clock for testing the gravitational redshift and a dual-species atom interferometer. By measuring the differential acceleration between ^{85}Rb and ^{87}Rb with the atom interferometer, the universality of free fall is intended to be tested to a level of $\eta = 2 \times 10^{-15}$. The fundamental increase in sensitivity stems from the prolonged time of free evolution between the interferometry pulses of $T_{\mathrm{sep}} = 5\,\mathrm{s}$. Residual accelerations on a satellite platform would be below $10^{-6}\,\mathrm{g}$ with mission durations spanning several years. Another proposed mission is the Quantum Test of the Equivalence principle and Space Time (QTEST) to be operated on the International Space Station. By pushing the pulse separation time to $T_{\mathrm{sep}} = 10\,\mathrm{s}$, a sensitivity of $\eta = 5 \times 10^{-16}$ shall be reached [56].

In the near future, first experiments utilizing ultra-cold atomic samples will be sent into space as a pathfinder for future missions. One of these missions is the Cold Atom Laboratory (CAL), which will be operated on the International Space Station [70], and the MAIUS missions that will demonstrate matter wave interferometry with Bose Einstein condensates on a sounding rocket [71, 72].

1.5 The QUANTUS collaboration

The QUANTUS[3] collaboration was founded in 2004 with the goal in mind to perform pathfinder experiments with ultra-cold quantum gases in a microgravity environment to pave the way for missions in space. It is supported by the German Space Agency DLR with funds provided by the German Federal Ministry of Economic Affairs and Energy. All of the experiments created within the QUANTUS collaboration comprise robust and compact mobile setups. They rely on atom chip technology for a fast creation of Bose-Einstein condensates. Miniaturized laser systems and electronics allow

[3] Quantengase unter Schwerelosigkeit: quantum gases in microgravity

for a rugged and compact experimental setup. The first microgravity experiments are operated at a drop tower, while the following experiments are conducted on sounding rockets.

1.5.1 Drop tower experiments

The feasibility a cold atom experiment in microgravity was demonstrated within the ATKAT pilot project at the drop tower in Bremen [73]. It featured a magneto-optical trap and served as a pathfinder for the first generation drop tower BEC experiment QUANTUS-1. Within QUANTUS-1, the first production and observation of a Bose-Einstein condensate in microgravity was achieved in 2007 [74, 75], followed by atom interferometry with magnetically lensed atoms [76]. Furthermore, studies showing the feasibility of Bragg beam splitters in a double-diffraction scheme have been published [64]. 441 drops have been performed until July 2013 and the experiment is now used for measurements on ground [77].

QUANTUS-1 featured only a single atomic species and the possibility to only drop the experiment resulting in a microgravity time of 4.7 s. The follow-up second generation apparatus QUANTUS-2, which is the subject of this thesis, is designed for a dual-species operation with rubidium and potassium and offers the possibility to prolong the microgravity time up to 9 s by using the catapult mode of the tower. To this end, the experiment had to be fitted into a smaller capsule and a new laser system for rubidium and potassium as well as a 2D magneto-optical trap for a rapid Bose-Einstein condensate production had to be designed. In 2009 the construction of the experiment began and the first drop was conducted in July 2014. Since then, over 200 drops and catapult flights have been performed, demonstrating the robustness of the fast Bose-Einstein condensate source as well as the precise control of the condensate dynamics. Furthermore, the reduction of the residual expansion rate of the condensate by means of a magnetic lens has been studied. In the future, it is planned to conduct dual-species atom interferometry to test the universality of free fall in microgravity.

1.5.2 Sounding rocket missions

To further extend the microgravity time and to conduct first experiments in space, the MAIUS[4] project was founded as a part of the QUANTUS family. Three sounding rocket missions are planned, with the first one already launched in January 2017. MAIUS-1 successfully created the first Bose-Einstein condensate in space. The following missions will comprise dual-species setups for performing tests of the weak equivalence principle in a sequential measurement within the second mission and a simultaneous measurement within the third mission. The microgravity time on the

[4]Materiewelleninterferometrie unter Schwerelosigkeit: matter wave interferometry in microgravity

sounding rocket can be stretched to six minutes. This will allow for interferometry sequences with unprecedented times of free evolution in the range of multiple seconds.

1.6 Motivation for this thesis and outline

This thesis is centered around the QUANTUS-2 experiment, which serves as a pathfinder for future high-precision matter wave interferometers on a satellite platform. To achieve the long-term goal of testing the Einstein equivalence principle in space with yet unprecedented sensitivity, the following selected key requirements have to be fulfilled:

- compact and robust experimental setup
- fast production of ultra-cold atom ensembles
- ultra-low rate of expansion of the released ensemble
- precise control of the atomic wave packet
- demonstration of long times of free evolution of multiple seconds

All these elements are subject of this thesis and have been investigated in great detail. The construction as well as the operation of QUANTUS-2 was a group effort. The physics package was designed and constructed by colleagues at the Leibniz Universität in Hannover. Technical concepts and scientific results regarding the performance of the experiment on ground have been published within two PhD theses [78, 79] as well as within a joint journal article [80]. Further results with a focus on the initial performance of the QUANTUS-2 experiment can be found in [79], whereas the absorption imaging detection systems are presented in greater detail in [81]. The adiabatic rapid passage as well as the technical aspects of the capsule supply will be discussed in [82]. Within the work for this thesis, over 200 drops and catapult flights have been performed at the drop tower in Bremen. The QUANTUS-2 drop tower team included Christian Deppner, Alexander Grote, Jan Rudolph, Tammo Sternke, Waldemar Herr and myself.

In addition to the team work, I contributed the following achievements:

- A compact and robust rubidium laser system was provided for the QUANTUS-2 apparatus to conduct experiments at the drop tower in Bremen. The setup was qualified within two drops and seven catapult flights at the drop tower in terms of its performance during a drop tower routine. Afterwards, the laser system was integrated into the QUANTUS-2 experiment.

- Key technologies, such as micro-integrated laser modules and compact laser system electronics, were used for the first time in a cold atom experiment in microgravity. By demonstrating their applicability, they could be qualified for future missions towards space.
- The dynamics of the magnetic lensing potential were investigated to get a comprehension of the observed experimental data. The excitation spectrum of density oscillations of the condensate was calculated and compared with observed data to get an understanding of the influence of the in-trap oscillations on the magnetic lens.
- The free evolution of the atomic ensemble after the lens was analyzed using a Hermite-Gaussian decomposition. This allows for a more precise characterization of the collimation quality of the lensed ensemble.
- Trajectories for a fast transport of the condensate were simulated and compared with experimental data. This represents valuable input for the further improvement of the transport routine.

The results presented in this thesis serve as a major contribution towards future experiments testing fundamental physics in space.

This thesis is structured as follows:

In Chapter 2 the fundamental theoretical concepts necessary to understand the scientific results are explained. In the first part, the phenomenon of Bose-Einstein condensation is presented. Expressions for the description of fundamental properties of a Bose-Einstein condensate as well as its dynamic behavior will be derived. The second part will deal with the magnetic trapping of neutral atoms. A description of the kinetic energy of an atomic ensemble released from a trap will be given in terms of an effective temperature. The concept of delta-kick cooling will be introduced, which allows for a reduction of the expansion rate of an atomic ensemble by making use of transient potentials.

The scientific results of this thesis have been achieved with the QUANTUS-2 experiment. It is introduced in Chapter 3 together with a discussion of the requirements on the experiment set by the drop tower environment. An overview of the physics package, which allows for a fast Bose-Einstein condensate production in microgravity, will be given.

A description of the catapult-capable laser system and the accompanying electronics will be subject of Chapter 4. A detailed description of all the subcomponents is followed

by a discussion of qualification drop and catapult tests that were conducted at the drop tower.

The experiment sequence for a rapid production of rubidium Bose-Einstein condensates in microgravity will be discussed in Chapter 5. An analysis of the performance of the complete setup in microgravity is followed by an examination of the Bose-Einstein condensate dynamics after the release from the trap.

In Chapter 6, it will be shown that a further reduction of the expansion rate of the released condensate can enhance the sensitivity of a matter wave interferometer. Strategies to reduce the kinetic energy in three dimensions by magnetic lensing are presented. Two different magnetic lens implementations were used and have been analyzed.

A discussion of the results as well as a wrap-up of this thesis can be found in the last Chapter 7. An outlook on further steps and concepts will be given.

2 Theory

In the first part of this chapter, we will elucidate the important theoretical concepts necessary to understand the phenomenon of Bose-Einstein condensation. The second part of this chapter deals with the magnetic trapping of neutral atoms. The reduction of the mean kinetic energy by means of a magnetic lens is introduced. Finally, some important remarks concerning the application of the concept of temperature in the field of ultra-cold atoms will be given.

2.1 Bose-Einstein condensation

Starting with a non-interacting Bose gas, we will describe the process of Bose-Einstein condensation, before taking into account atomic interactions for a more precise description of the condensate wave function. We will then derive expressions for the fundamental excitation spectrum of a Bose-Einstein condensate trapped in an anisotropic potential.

2.1.1 The non-interacting Bose gas

Following the spin statistics of quantum mechanics, every particle can be classified as either a boson having integer spin or a fermion having half-integer spin. A fundamental statistic is associated to each class of particles. For a number of non-interacting bosons in thermodynamic equilibrium, the mean occupation number of the single-particle state ν is given by the Bose distribution

$$f^0(\epsilon_\nu) = \frac{1}{e^{(\epsilon_\nu - \mu)/k_B T} - 1}, \tag{2.1}$$

whereas ε_ν is the energy of the single-particle state, k_B the Boltzmann constant and T the temperature of the ensemble [83]. The chemical potential μ is determined by the normalization condition of the distribution for Eqn. (2.1) and is defined as the energy necessary to add a particle to the ensemble. At high temperatures, the Bose distribution can be approximated by the Boltzmann distribution

$$f^0(\epsilon_\nu) \simeq e^{-(\epsilon_\nu - \mu)/k_B T}. \tag{2.2}$$

This is conform with the correspondence principle that states that quantum theory transitions to classical physics for large energies. For high temperatures, the energy of the lowest single-particle state is large compared to the chemical potential since the mean occupation number of any state is much less than unity. When lowering the temperature the chemical potential rises and the mean occupation numbers increase. To prevent the Bose distribution to yield negative values, the chemical potential always has to stay below the energy of the lowest single-particle state. If the overall number of particles accommodating excited states is less than the total number in all states, the remaining particles have to occupy the single-particle ground state. For ever lower temperatures, more atoms are thus condensed in the ground-state. Due to the Pauli exclusion principle, this so called Bose-Einstein condensation can only occur with bosons, while fermions do not show this behavior. The transition temperature T_c, at which the ground state is becoming macroscopically occupied, is defined as

$$k_B T_c = \frac{\hbar \bar{\omega} N^{1/3}}{\zeta^{1/3}(3)}, \tag{2.3}$$

with $\zeta(\alpha = 3) = 1.202$ being the Riemann zeta function ($\alpha = 3$ for 3D harmonic potentials), N the particle number and $\bar{\omega} = (\omega_x \omega_y \omega_z)^{1/3}$ being the geometric mean of the frequencies of the harmonic trapping potential for the three Cartesian coordinates. The occupation of the ground state is depending on the temperature and for a three-dimensional harmonic oscillator is given by the condensate fraction

$$N_0(T) = N \left(1 - \left(\frac{T}{T_c} \right)^3 \right). \tag{2.4}$$

For non-interacting particles, the density profile of the ground state is solely given by the single-particle density multiplied by the number of atoms in the ground state N_0

$$n(\mathbf{r}) = N_0 |\phi_0(\mathbf{r})|^2. \tag{2.5}$$

For a three-dimensional harmonic potential of the form

$$V(\mathbf{r}) = \frac{1}{2} m(\omega_x^2 x^2 + \omega_y^2 y^2 + \omega_z^2 z^2) \tag{2.6}$$

the single particle wave function $\phi_0(\mathbf{r})$ of the ground state takes the simple form of a Gaussian distribution

$$\phi_0(\mathbf{r}) = \frac{1}{\pi^{3/4}(a_x a_y a_z)^{1/2}} e^{-x^2/2a_x^2} e^{-y^2/2a_y^2} e^{-z^2/2a_z^2}. \tag{2.7}$$

Here we introduced the characteristic length of the harmonic oscillator a_j for the three Cartesian dimensions $j = \{x, y, z\}$ depending on the trapping frequencies ω_j in the respective direction

$$a_j = \sqrt{\frac{\hbar}{m\omega_j}}. \tag{2.8}$$

In contrast to a thermal ensemble trapped in a harmonic potential, the width of a trapped non-interacting Bose-Einstein condensate only depends on the trapping frequencies of the potential. This becomes evident at the onset of condensation when a sharp narrow density peak starts to emerge from the thermal ensemble background due to the condensate representing the compact ground state wave function of the harmonic oscillator. This bimodal density distribution is a clear indication for Bose-Einstein condensation. A second peculiarity becomes evident when releasing an ensemble from an anisotropic trapping potential. While a released thermal ensemble shows an isotropic density distribution after sufficient time of free evolution due to its isotropic velocity distribution, a Bose-Einstein condensate shows an anisotropic density profile. The observed inversion of the aspect ratio of the cloud when releasing the condensate from the trap was another clear evidence for the onset of Bose-Einstein condensation.

2.1.2 Interactions and the Gross-Pitaevskii equation

Till now, we assumed an ensemble of non-interacting bosons. However, in a typical lab experiment, the densities are at a level at which inter-atomic interactions can no longer be neglected. To get a better understanding of the condensate wave function, we now introduce interactions between the atoms. Since we want to avoid calculating short-range effects between the atoms, we introduce an effective interaction, which considers only binary collisions at low energy scales. This is a valid approach when dealing with diluted gases where interactions are very small for the typical particle separation lengths. The interaction potential V_{int} can be thus expressed by a contact interaction potential with $\mathbf{r}$ and $\mathbf{r}'$ being the position of the two interacting particles

$$V_{\text{int}}(\mathbf{r}' - \mathbf{r}) = U_0 \delta(\mathbf{r}' - \mathbf{r}), \tag{2.9}$$

using a pseudo-potential

$$U_0 = \frac{4\pi\hbar^2 a}{m}, \tag{2.10}$$

whereas a is the s-wave scattering length for the given atomic isotope. The many-body Hamiltonian H with an interaction potential $V_{\text{int}}(\mathbf{r}-\mathbf{r}')$ can be written as

$$H = \int d\mathbf{r}\ \Psi^\dagger(\mathbf{r}) \left[-\frac{\hbar^2}{2m}\nabla^2 + V(\mathbf{r}) \right] \Psi(\mathbf{r}) + \frac{1}{2}\int d\mathbf{r}d\mathbf{r}'\ \Psi^\dagger(\mathbf{r})\Psi^\dagger(\mathbf{r}')V_{\text{int}}(\mathbf{r}-\mathbf{r}')\Psi(\mathbf{r}')\Psi(\mathbf{r}). \tag{2.11}$$

$\Psi^\dagger(\mathbf{r})$ and $\Psi(\mathbf{r})$ are the field operators for the creation and annihilation of a boson at position $\mathbf{r}$. The calculation of the ground state starting from this Hamiltonian is in principle possible but can be very cumbersome for large particle numbers. It is possible to use a Hartree or mean-field approach to solve the Schrödinger equation [84]. This approach was formulated by Bogoliubov in 1947 for a dilute Bose gas and offers quantitative predictions for the static, dynamic and thermodynamic properties of a trapped Bose gas. Using this approach, one can find a nonlinear Schrödinger equation for the description of the condensate by minimizing the energy

$$E(\psi) = \int d\mathbf{r} \left(\frac{\hbar^2}{2m}|\nabla\psi(\mathbf{r})|^2 + V(\mathbf{r})|\psi(\mathbf{r})|^2 + \frac{1}{2}U_0|\psi(\mathbf{r})|^4 \right), \tag{2.12}$$

under the condition that the total number of particles is constant [83]:

$$N = \int d\mathbf{r}|\psi(\mathbf{r})|^2. \tag{2.13}$$

This can be done by using the method of Lagrange multipliers by applying $\delta E - \mu\delta N = 0$, whereas the chemical potential μ serves as the Lagrange multiplier. This minimization results in a nonlinear Schrödinger equation, which describes the condensate wave function:

$$\mu\psi(\mathbf{r}) = \left(-\frac{\hbar^2}{2m}\nabla^2 + V(\mathbf{r}) + U_0|\psi(\mathbf{r})|^2 \right) \psi(\mathbf{r}). \tag{2.14}$$

This is the so-called time-independent Gross-Pitaevskii equation, which was derived independently by Gross and Pitaevskii in 1961 [85, 86].

2.1.3 Thomas-Fermi approximation

The Gross-Pitaevskii equation can be solved for example by numerical integration or a variational calculation. A convenient approximation is given by neglecting the kinetic energy term in the Gross-Pitaevskii equation. This so called Thomas-Fermi approximation is valid for positive scattering lengths and large atom numbers so that the condition $Na/\bar{a} \gg 1$ is fulfilled. Under this condition the time-independent Gross-Pitaevskii Eqn. 2.14 reduces to

$$\mu\psi(\mathbf{r}) = \left(V(\mathbf{r}) + U_0|\psi(\mathbf{r})|^2 \right) \psi(\mathbf{r}). \tag{2.15}$$

The solution of this equation has the simple form

$$|\psi_{\mathrm{TF}}(\mathbf{r})|^2 = \frac{\mu - V(\mathbf{r})}{U_0} \qquad \forall \qquad \mu > V(\mathbf{r}) \tag{2.16}$$

$$|\psi_{\mathrm{TF}}(\mathbf{r})|^2 = 0 \qquad \forall \qquad \mu < V(\mathbf{r}) \tag{2.17}$$

For a harmonic trapping potential, the probability density $n(\mathbf{r}) = |\psi(\mathbf{r})|^2$ thus shows the form of an inverted parabola with the surface of the condensate defined by the relation $V(\mathbf{r}) = \mu$ where the chemical potential can be derived from the normalization of $n(\mathbf{r})$:

$$\mu = \frac{\hbar\bar{\omega}}{2}\left(\frac{15Na}{\bar{a}}\right)^{2/5}. \tag{2.18}$$

Here we introduced the characteristic length

$$\bar{a} = \sqrt{\frac{\hbar}{m\bar{\omega}}}. \tag{2.19}$$

The chemical potential depends on the trapping frequencies as well as the atom number. The spatial extent of the parabola shaped density along direction $j = \{x, y, z\}$ is given in terms of the Thomas-Fermi radius

$$R_j^2 = \frac{2\mu}{m\omega_j^2}. \tag{2.20}$$

Inserting the chemical potential (2.18) in the equation for the Thomas-Fermi radius, we can calculate the Thomas-Fermi radius in dependence of the atom number and the trapping frequencies

$$R_j = \bar{a}\left(\frac{15Na}{\bar{a}}\right)^{1/5}\frac{\bar{\omega}}{\omega_j}. \tag{2.21}$$

For repulsive interaction, an increase in atom number is thus not just adding more particles to the ground state of the quantum harmonic oscillator but also increases the size of the ensemble due to the inter-atomic interactions. It is often desired to rescale the radius R of a condensate in the Thomas-Fermi limit with atom number N to a normalized atom number N_0. The normalized radius R_0 is given by

$$R_0 = R\left(\frac{N_0}{N}\right)^{1/5}. \tag{2.22}$$

2.1.4 Scaling approach

It is often of interest to calculate the evolution of the size of a trapped Bose-Einstein condensate under change of the confining potential. A simple approach was given

by Castin et al. [87], which offers the possibility of not having to solve the time-dependent Gross-Pitaevskii equation – but simply solving three differential equations. Since a variation of the trapping potential would convert potential energy into kinetic energy, it could be no longer neglected when using a Thomas-Fermi approximation approach. The problem can be circumvented by finding a unitarian transformation that eliminates excessive kinetic energy. The Bose-Einstein condensate can be modeled as a classical gas with a spatial density $\rho_{cl} = (\mathbf{r}, t)$, which is normalized to the particle number N and the pseudo-potential U_0

$$\mathbf{F}(\mathbf{r}, t) = -\nabla(V(\mathbf{r}, t) + U_0\rho_{cl}(\mathbf{r}, t)). \tag{2.23}$$

At time $t = 0$, the condensate shall be in equilibrium ($\mathbf{F} = 0$) and thus resembles the density given by the Thomas-Fermi approximation $\rho_{cl}(\mathbf{r}, 0) = N|\Phi_{TF}(\mathbf{r}, 0)|^2$. For $t > 0$ the change of the size of the condensate can be attributed to a simple scaling of the initial size $R_j(0)$ with a time dependent factor $\lambda_j(t)$

$$R_j(t) = \lambda_j(t)R_j(0). \tag{2.24}$$

The evolution of the classical density can be thus represented as

$$\rho_{cl}(\mathbf{r}, t) = \frac{1}{\lambda_x(t)\lambda_y(t)\lambda_z(t)} \cdot \rho_{cl}((r_j/\lambda_j(t)), 0). \tag{2.25}$$

Applying Newton's law $m\ddot{R}_j(t) = F_j(\mathbf{R}(t), t)$ on the trajectory Eqn. (2.24) implies

$$m\ddot{\lambda}_j(t)R_j(0) = -\partial_{r_j}V(\mathbf{R}(t), t) + \frac{1}{\lambda_j\lambda_x\lambda_y\lambda_z}\partial_{r_j}V(\mathbf{R}(0), 0). \tag{2.26}$$

Given that the potential $V(\mathbf{r}, t)$ can be expressed in a harmonic form

$$V(\mathbf{r}, t) = \frac{1}{2}\sum_{j=x,y,z} m\omega_j^2(t)r_j^2, \tag{2.27}$$

Eqn. (2.26) holds if the scaling factors $\lambda_j(t)$ satisfy the system of differential equations

$$\ddot{\lambda}_j = \frac{\omega_j^2(0)}{\lambda_j\lambda_x\lambda_y\lambda_z} - \omega_j^2(t)\lambda_j. \tag{2.28}$$

This system of differential equations describes the evolution of the time-dependent scaling factors for any time-dependent harmonic trapping potential. It should be mentioned that the scaling coefficients are taking into account all dynamics of the macroscopic wave function and yields results close to solutions of the time-dependent Gross-Pitaevskii equation [84].

2.1.5 Excitations of the atomic ensemble

The equilibrium properties of the BEC are described by the time-independent Gross-Pitaevskii equation (2.14). We already described the evolution of the size of the condensate under change of the trapping potential using a scaling approach in the previous section. To get a description of the dynamic properties and the excitation spectrum of the condensate in a trap, we turn to a time-dependent Gross-Pitaevskii equation:

$$i\hbar\frac{\partial}{\partial t}\psi(\mathbf{r},t) = \left(-\frac{\hbar^2}{2m}\nabla^2 + V(\mathbf{r}) + U_0|\psi(\mathbf{r},t)|^2\right)\psi(\mathbf{r},t) \tag{2.29}$$

An explicit analytical expression for the excitation frequency spectrum of a condensate has been given by Stringari [88]. A follow-up approach by Pérez-García et al. [89] gives analytical solutions for the excitation frequencies following a Ritz's optimization procedure on the time-dependent Gross-Pitaevskii equation. It is taking into account anisotropic trapping potentials as well as variable interaction strengths and atom numbers.

We consider a cigar shaped trap having two equal radial trapping frequencies $\omega_r = \omega_x = \omega_y$ and an axial trapping frequency ω_z. The anisotropic harmonic trapping potential can be expressed with anisotropy factors λ_j with $j = x, y, z$

$$V(\mathbf{r}) = \frac{1}{2}m\omega_r(\lambda_x^2x^2 + \lambda_y^2y^2 + \lambda_z^2z^2). \tag{2.30}$$

For a trap with radial symmetry, we define the anisotropy factors $\lambda_x = \lambda_y = 1$ and $\lambda_z = \omega_z/\omega_r$. The time dependent Gross-Pitaevskii equation can be solved by minimizing the Lagrangian density

$$\mathcal{L} = \frac{i}{2}\hbar\left(\Psi\frac{\partial\Psi^*}{\partial t} - \Psi^*\frac{\partial\Psi}{\partial t}\right) - \frac{\hbar^2}{2m}|\nabla\Psi|^2 + V(r)|\Psi|^2 + \frac{2\pi a\hbar^2}{m}|\Psi|^4. \tag{2.31}$$

As a trial function, we use a product of Gaussians since they resemble the ground state probability distribution when interactions are absent:

$$\Psi(x,y,z,t) = A(t)\prod_{j=x,y,z} e^{-\frac{[j-j_0(t)]^2}{2w_j^2} + ij\alpha_j(t) + ij^2\beta_j(t)}. \tag{2.32}$$

The trial function is depending on the parameters $A(t)$ for the amplitude, w_j for the width of the trial function, $\alpha_j(t)$ for the slope and $\beta_j(t)$ for the curvature. Using this trial function one can minimize the effective Lagrangian

$$L = \langle\mathcal{L}\rangle = \int_{-\infty}^{\infty}\mathcal{L}\quad d^3\mathbf{r}. \tag{2.33}$$

As a first result we get a differential equation for the motion of the center of the condensate that can be expressed as

$$\ddot{j}_0 + \lambda_j^2 \omega_r^2 j_0 = 0 \quad , \quad (j = x, y, z). \tag{2.34}$$

The motion of the center of the condensate thus undergoes simply a harmonic oscillation around the trap center with the trapping frequencies ω_j. It does not depend on the particle number and can be therefor seen as the classic motion of a single particle within a harmonic potential. The evolution of the widths of the condensate are governed by

$$\ddot{w}_x + \lambda_x^2 \omega_r^2 w_x = \frac{\hbar^2}{m^2 w_x^3} + \sqrt{\frac{2}{\pi}} \frac{a\hbar^2 N}{m^2 w_x^2 w_y w_z}. \tag{2.35}$$

Equations for the other two directions can be obtained by cyclic permutations of the indices x, y, z. We can now make a transition to dimensionless variables by introducing $\tau = \omega_r t$, $w_j = a_0 v_j$. The interactions are described by $P = \sqrt{2/\pi} N a/\bar{a}$. The evolution of the width of the condensate is then given by

$$\frac{d^2}{d\tau^2} v_x + \lambda_x^2 v_x = \frac{1}{v_x^3} + \frac{P}{v_x^2 v_y v_z}. \tag{2.36}$$

Again, equations for the other two directions can be obtained by cyclic permutations of the indices x, y, z. We focus now on anisotropic traps with a cigar shape ($\lambda_x = \lambda_y = 1$). The equilibrium points v_0 of Eqn. (2.36) satisfy the equations

$$v_0 = \frac{1}{v_0^3} + \frac{P}{v_0^3 v_{0z}}, \tag{2.37}$$

$$\lambda_z^2 v_{0z} = \frac{1}{v_{0z}^3} + \frac{P}{v_{0z}^2 v_0^2}, \tag{2.38}$$

whereas $v_0 = v_{0x} = v_{0y}$. These equations yield only one stable equilibrium point for positive scattering lengths. We can now expand equations (2.36) around these equilibrium points to find the low lying excitation frequencies for the radial quadrupole (ω_{rq}), quadrupole (ω_q, negative sign) and breathing mode (ω_b, positive sign)

$$\omega_{rq} = 2\omega_r \sqrt{1 - 2P_{4,1}} \tag{2.39}$$

$$\omega_{q,b} = 2\omega_r \left[\frac{1}{2}(1 + \lambda_z^2 - P_{2,3}) \pm \frac{1}{2} \sqrt{(1 - \lambda_z^2 + P_{2,3})^2 - 8P_{3,2}} \right]^{1/2} \tag{2.40}$$

These fundamental density oscillation modes changing the width of the condensate are depicted in Fig 2.1.

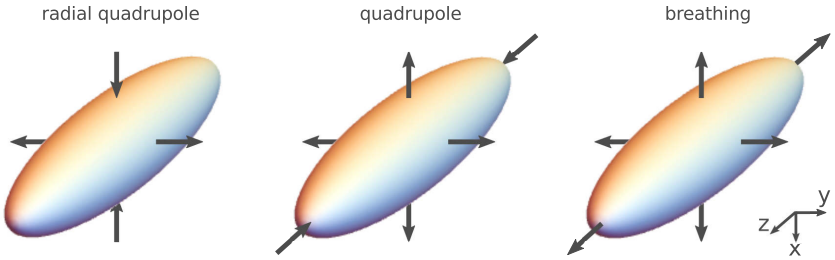

Figure 2.1: Fundamental density oscillations of a Bose-Einstein condensate in a cigar shaped trap with two fast radial and one slow axial trapping frequency.

2.2 Confining and collimating atomic ensembles

In the following sections, the trapping of neutral atoms using magnetic potentials will be introduced. The reduction of the kinetic energy of an atomic ensemble by means of a magnetic lens will be described. The chapter ends with a short discussion about the applicability of the thermodynamic temperature in context with ultra-cold atoms.

2.2.1 Magnetic traps

In classical physics, the interaction potential between a magnetic moment $\boldsymbol{\mu}$ of a neutral atom and a magnetic field $\mathbf{B}(\mathbf{r})$ is given by

$$V(\mathbf{r}, \theta) = -\boldsymbol{\mu}\mathbf{B}(\mathbf{r}) = -\mu B(\mathbf{r}) \cos\theta, \tag{2.41}$$

with θ being the angle between the magnetic field and the magnetic moment [90]. In quantum mechanics, only certain values for the projection of the vector of the magnetic moment onto the magnetic field vector are allowed and the interaction energy is thus

$$V(\mathbf{r}, m_F) = g_F \mu_B m_F B(\mathbf{r}), \tag{2.42}$$

where m_F is the quantum number for the projection, μ_B the Bohr magneton and g_F the Landé factor. If an atom is now placed into a magnetic field, it will move upward or downward the gradient, depending on the sign of the product $g_F m_F$ to minimize its potential energy, while atoms in the state $|m_F = 0\rangle$ do not experience a force to first order. Since Maxwell's equations do not allow a maximum in the magnetic field in free space, only so called weak-field seekers with $g_F m_F > 0$ are trappable using a magnetic field minimum.

Trap losses

By inducing transitions to non-trappable states with $g_F m_F \leq 0$ we can expel atoms from the trap. This technique is used for evaporative cooling of an ensemble by removing the hottest atoms. This can be done, for example, by driving selectively atomic transitions to a non-trappable state using a radio frequency. Subsequent rethermalization leads to a lower temperature of the ensemble. However such trap losses can also occur in regions of the trap where the magnetic field is too weak. Classically, such spin-flip losses are induced, when the change of the angle θ between the atoms magnetic moment and the external magnetic field is fast compared to the Larmor frequency ω_L

$$\frac{d\theta}{dt} < \omega_L = \frac{\mu B}{\hbar}. \tag{2.43}$$

These so-called *Majorana losses* can occur at the trap bottom, when the magnetic field strength is getting close to zero.

Quadrupole trap

The most simple magnetic trap geometry for confining neutral atoms is the quadrupole trap. Around the vicinity of its center, the magnetic field can be expressed as a linear function of the magnetic field gradient B'

$$\mathbf{B} = B'_x x\mathbf{e_x} + B'_y y\mathbf{e_y} + B'_z z\mathbf{e_z}. \tag{2.44}$$

This trap configuration features a zero magnetic field at its field minimum and can give rise to Majorana losses. Thermal ensembles with a sufficient high temperature are anyway not affected since the probability of an atom to rest at the field minimum is negligible due to the high mean velocity.

Ioffe-Pritchard trap

A trap geometry offering a non-zero magnetic field at its minimum is the Ioffe-Pritchard trap [91]. Its magnetic field can be expressed as follows:

$$\mathbf{B} = B_0 \begin{pmatrix} 1 \\ 0 \\ 0 \end{pmatrix} + B' \begin{pmatrix} 0 \\ -y \\ z \end{pmatrix} + \frac{B''}{2} \begin{pmatrix} x^2 - \frac{1}{2}(y^2 + z^2) \\ -xy \\ -xz \end{pmatrix}. \tag{2.45}$$

The field modulus around the vicinity of the minimum for $x \ll \sqrt{B_0/B'}$ and $y, z \ll B_0/B'$ is given by

$$B \approx B_0 + \frac{B''}{2}x^2 + \frac{1}{2}\left(\frac{B'^2}{B_0} - \frac{B''}{2}\right)(y^2 + z^2). \tag{2.46}$$

The trapping frequency of a harmonic potential can be written in terms of the second derivative of the potential or the magnetic field, respectively

$$\omega_j = \sqrt{\frac{1}{m}\frac{d^2V}{dr_j^2}} = \sqrt{\frac{\mu}{m}\frac{d^2B}{dr_j^2}}. \tag{2.47}$$

The Ioffe-Pritchard trap thus offers an axial symmetry with one trapping frequency ω_a along the axis of symmetry and two equal trapping frequencies ω_r along the radial direction

$$\omega_a = \sqrt{\frac{\mu}{m}B''}, \qquad \omega_r = \sqrt{\frac{\mu}{m}\left(\frac{B'^2}{B_0} - \frac{B''}{2}\right)}. \tag{2.48}$$

The aspect ratio $\lambda = \omega_a/\omega_r$ can be tuned to generate a cigar-shaped, isotropic or pancake-shaped trap geometry by adjusting the ratio between B'' and B'^2/B_0.

Trapping frequencies and eigensystem

Given a function $V(\mathbf{r})$ with an existing continuous second derivative with a local minimum in $\mathbf{r_0}$, we can write a Taylor expansion around $\mathbf{r_0}$ till second order as

$$V(\mathbf{r}) \approx V(\mathbf{r_0}) + \frac{1}{2}(\mathbf{r}-\mathbf{r_0})^T H(\mathbf{r_0})(\mathbf{r}-\mathbf{r_0}), \tag{2.49}$$

where the first order term is zero due to $\mathbf{r_0}$ being a critical point. Furthermore, we made use of the Hessian matrix $H(\mathbf{r})$, which is defined by the second derivative of $V(\mathbf{r})$:

$$H(\mathbf{r}) = \begin{pmatrix} \frac{\partial^2 V(\mathbf{r})}{\partial x^2} & \frac{\partial^2 V(\mathbf{r})}{\partial x \partial y} & \frac{\partial^2 V(\mathbf{r})}{\partial x \partial z} \\ \frac{\partial^2 V(\mathbf{r})}{\partial y \partial x} & \frac{\partial^2 V(\mathbf{r})}{\partial y^2} & \frac{\partial^2 V(\mathbf{r})}{\partial y \partial z} \\ \frac{\partial^2 V(\mathbf{r})}{\partial z \partial x} & \frac{\partial^2 V(\mathbf{r})}{\partial z \partial y} & \frac{\partial^2 V(\mathbf{r})}{\partial z^2} \end{pmatrix}. \tag{2.50}$$

If we assume now $V(\mathbf{r})$ being a trapping potential with a trap minimum at $\mathbf{r_0}$ and a Hessian matrix $H(\mathbf{r_0})$, by evaluating the eigenproblem for $H(\mathbf{r_0})$ we can calculate the eigenvectors and eigenvalues for the potential at the minimum. The eigenvectors span an ellipsoid with the eigenvalues defining the size of the ellipsoid. We can identify the eigenvalues λ_j of the diagonalized Hessian matrix with the trapping frequencies:

$$\omega_j = \sqrt{\frac{\lambda_j}{m}}. \tag{2.51}$$

Furthermore, the eigenvectors of the trapping potential at the minimum can be rotated against the lab coordinate system, depending on the configuration of the magnetic field creating structures.

Anharmonicities

The harmonic approximation for the Ioffe-Pritchard type magnetic field is just valid around the vicinity of the field minimum. The general potential in dimension can be expressed as a polynomial series to a degree n, taking into account deviations from the harmonic approximation:

$$V(x) = V_0 + \frac{1}{2}m\omega_x^2(x - x_0)^2 + \sum_{n=3}^{\infty} \frac{1}{n} \frac{1}{(L_n)^{n-2}} m\omega_x^2(x - x_0)^n. \tag{2.52}$$

The coefficients L_n give a measure at which distance the force created of a term of higher order is comparable to the force arising from the harmonic expression.

2.2.2 Delta-kick cooling approach

Let us assume an ensemble of atoms trapped in a harmonic potential $V(x) = \frac{1}{2}m\omega^2 x^2$. The Hamiltonian is given by

$$H = \frac{p^2}{2m} + V(x) \quad \forall t < 0. \tag{2.53}$$

At $t = 0$ the trapping potential is extinguished. The particles will move freely along with their individual velocity $\dot{x}(t = 0)$. After a sufficient long evolution time $t_0 \gg 0$ the particles will show a distinct correlation between their position and velocity $v(x) = x/t_0$. At the time t_0 we pulse the initial trapping potential $V(x)$ using a Gaussian function in time

$$\tilde{V}(x, t) = V(x) \cdot \exp\left[-\frac{(t - t_0)^2}{2t_k^2}\right], \tag{2.54}$$

whereas t_k denotes the pulse duration. For sufficient small times t_k we can write the Hamiltonian with the transient potential exerting a kick on the atoms as

$$H = \frac{p^2}{2m} + \sqrt{2\pi}t_k V(x)\delta(t - t_0), \tag{2.55}$$

where we expressed the kicking potential $\tilde{V}(x, t)$ in terms of the initial potential $V(x)$ multiplied by a delta-function and a factor $\sqrt{2\pi}t_k$, which depends on the kick duration t_k and describes the strength of the kick. The force created by the transient potential depends linearly from the position of the atoms. Due to the linear correlation between the position and the velocity of the atoms after the time t_0, the motion of all the atoms can be minimized under the condition that the kick time t_k fulfills the relation

$$\sqrt{2\pi}t_k\omega^2 t_0 \approx 1. \tag{2.56}$$

This technique has been introduced as delta-kick cooling by Ammann et al. in 1997 [92], owing to the delta function form of the kicking potential and has been first described in 1986 by Chu et al. [61]. While first considered as an optical cooling technique, this scheme can be used for any harmonic trapping potential. It should be noted that it is impossible to increase the phase space density using time-dependent conservative potentials. As a consequence, it is not possible to achieve Bose-Einstein condensation using delta-kick cooling [93].

Rate of expansion and effective temperature

The equipartition theorem states that in thermal equilibrium, every degree of freedom contributes a mean energy $\frac{1}{2}k_BT$ to the total energy of the ensemble with T being the temperature. The mean total energy thus depends on the number of degrees of freedom f

$$\langle E\rangle = \frac{1}{2}fk_BT. \tag{2.57}$$

For a three-dimensional ideal monatomic gas trapped in a flat box potential, its mean energy is given by

$$\langle E\rangle = \frac{1}{2}m\langle v^2\rangle = \frac{3}{2}k_BT. \tag{2.58}$$

The temperature of the ensemble is thus related to its mean kinetic energy. The probability distribution for a single component of the velocity vector of an atom is given by the Maxwell-Boltzmann distribution

$$f_v(v) = \sqrt{\frac{1}{2\pi\dot{\sigma}^2}}\exp\left[-\frac{1}{2}\frac{v^2}{\dot{\sigma}^2}\right], \tag{2.59}$$

which is a Gaussian centered around zero with the standard deviation of the velocity

$$\dot{\sigma} = \sqrt{\frac{k_BT}{m}}. \tag{2.60}$$

If we extinguish the box-like trapping potential, the atoms move freely along in accordance with the Maxwell-Boltzmann distribution and after sufficient time, the spatial density of atoms resembles a Gaussian distribution with σ being the standard deviation of the distribution. It is then possible to calculate the temperature T of the ensemble before the release from the measured rate of expansion $\dot{\sigma}$ after the release. To be exact and in line with thermodynamics, one should understand that a temperature cannot be attributed to an expanding ensemble since it is not in thermodynamic equilibrium. Anyhow, the expansion rate is often quantified in terms of an "effective temperature" in the cold atom community using Eqn. (2.60).

The concept of an effective temperature as a mean to quantify the rate of expansion

can be also applied to a BEC. In this case, some small important considerations have to be taken care of. For a thermal ensemble, we used the standard deviation σ to describe the spatial extent of the distribution. Its rate of expansion $\dot{\sigma}$ is given in terms of the time derivative of the standard deviation. However, the typical parameter describing the size of a BEC deeply in the Thomas-Fermi regime is the TF radius R. When comparing the rate of expansion of a BEC with a thermal ensemble, we would end up with an overestimation of the expansion rate of the BEC when using the time derivative of the TF radius $\dot{R}$ since it represents the outer rim of the distribution rather than the mean quadratic deviation. We are therefor interested in the temporal evolution of the standard deviation of the Thomas-Fermi distribution. Given a normalized Thomas-Fermi-like probability distribution with radius R and center μ

$$f_{\mathrm{TF}}(x) = \frac{3}{4R}\left(1 - \frac{(x-\mu)^2}{R^2}\right) \qquad \forall -R < x < R, \quad \text{otherwise } 0, \tag{2.61}$$

the mean squared deviation σ is given by the square root of the variance of the Thomas-Fermi distribution

$$\sigma = \sqrt{\mathrm{Var}(X)} = \left(\int_{-R}^{R} (x-\mu)^2 f_{\mathrm{TF}}(x)dx\right)^{1/2}. \tag{2.62}$$

Evaluating this expression yields the conversion factor to calculate the standard deviation of a Thomas-Fermi distribution σ from its Thomas-Fermi radius R

$$\sigma = \sqrt{\frac{1}{5}} \cdot R \approx 0.447 \cdot R \tag{2.63}$$

According to Eqn. (2.60), we will use the time derivative of the standard deviation of the Thomas-Fermi distribution to attribute an effective one-dimensional temperature to the BEC

$$T_{\mathrm{1D}} = \frac{m}{k_B} \times \dot{\sigma}^2 = \frac{m}{k_B} \times \left(\sqrt{\frac{1}{5}}\frac{dR}{dt}\right)^2. \tag{2.64}$$

It is important to note that in comparison to a thermal ensemble, a BEC can feature three independent rates of expansion for each Cartesian dimension depending on the initial trapping frequencies. Furthermore, a temperature is not defined for a BEC since thermodynamics are dealing with multipartite systems, whereas a BEC resembles a single macroscopic quantum object. The attribution of an effective temperature serves only as a figure of merit for comparing the rate of expansion with a thermal ensemble. We will thus in general try to avoid the term “temperature” and rather use the time derivative of the standard deviation of the spatial distribution $\dot{\sigma}$ to characterize the rate of expansion.

3 Compact and robust high-flux source for ultra-cold atoms

QUANTUS-2 is the second generation BEC drop capsule to be operated at the drop tower in Bremen. While QUANTUS-1 was exclusively operated in the drop mode, the second generation experiment extends the microgravity time to 9 s using the catapult mode of the drop tower. Just like its predecessor, QUANTUS-2 is relying on the use of the atom chip technology that allows for a fast and efficient creation of a BEC in a mobile setup. Novel features of the second generation experiment include a three-layer atom chip, which not only features a wider range of magnetic field configurations but also can create a quadrupole field for the magneto-optical trap (MOT) by means of mesoscopic wire structures. Large anti-Helmholtz coils are therefor not necessary. Also, the second generation features a $2D^+$MOT for fast loading of the 3D-MOT in the science chamber. In addition to this, QUANTUS-2 is designed to operate with two atomic species, rubidium and potassium, to test the universality of free fall by means of differential atom interferometry. A novel catapult-capable laser system is making use of micro-integrated diode laser modules as well as new compact laser system electronics. Thanks to these technological improvements, it was possible to fit the experiment in the catapult capsule, which is by a factor of about two smaller than the first generation experiment drop capsule of QUANTUS-1 [94].

In the following sections, the requirements defined by the drop tower facility as well as the technical solutions will be described. An overview of the experiment will be given and relevant components of the physics package as well as the accompanying electronics will be introduced. A more detailed description of the physics package can be found in [78]. The laser system will be subject of Chapter 4 since the implementation and testing was a central part of the work of this thesis. After the catapult capsule and laser system has been introduced, we will turn to the basic experiment sequences and principles of operation in microgravity in Chapter 5.

3.1 The drop tower facility

The drop tower in Bremen offers the possibility to conduct experiments in microgravity on earth. It is run by the Center of Applied Space Technology and Microgravity (ZARM) and is part of the University of Bremen. A schematic of the drop tower and the experiment capsules is shown in Fig. 3.1. The outer concrete tower has a total height of 145 m and contains a 120 m tall metal tube in which the experiments can be dropped or alternatively catapulted from the bottom. To reduce air friction and residual accelerations during the flight, the inner metal tube is evacuated to a pressure of about 20 Pa within 90 min. Depending on the desired drop tower operation mode, the experiments have to be integrated in a drop or catapult capsule, whereas the catapult capsule offers the possibility to use both operation modes. At the end of the flight sequence, the capsule is landing in a deceleration container filled with polystyrene pellets. The accelerations working on the experiment are depicted in Fig. 3.2. There are two basic modes of operation:

Drop mode

The experiment is dropped from the top of the tower from a height of 110 m. This yields a microgravity time of about 4.7 s. The capsule is subjected to accelerations of up to 50 g during deceleration in the container. During the evacuation of the drop tube, the experiment is hanging at the top of the tube and connected to an umbilical that provides electrical connections for loading some of the batteries and access to a chiller for water cooling. Although the microgravity time can be expanded by using the catapult mode, the drop mode offers a less complicated operation routine since the capsule is simply released from the top of the tower. This also results in lower capsule rotation rates during the microgravity time.

Catapult mode

A pneumatic catapult is installed at the drop tower bottom. This offers the possibility to shoot the experiment upwards, thus extending the available microgravity time to about 9 s. Just like in drop operation, the capsule is connected to an umbilical while sitting on the catapult piston during evacuation. Approximately 15 min before the launch, the capsule is disconnected from the umbilical and the piston is lowered below the surface by about 11 m while the catapult pressurizes. During the launch, the experiment is subjected to accelerations of up to 40 g. This defines a critical requirement for the experiment because full operability has to be guaranteed immediately after the catapult launch. Furthermore, catapult flights can be only done using the smaller capsule version demanding an even more integrated experimental setup. Since the capsule is sitting on the catapult piston on its bottom nose cone without any lateral

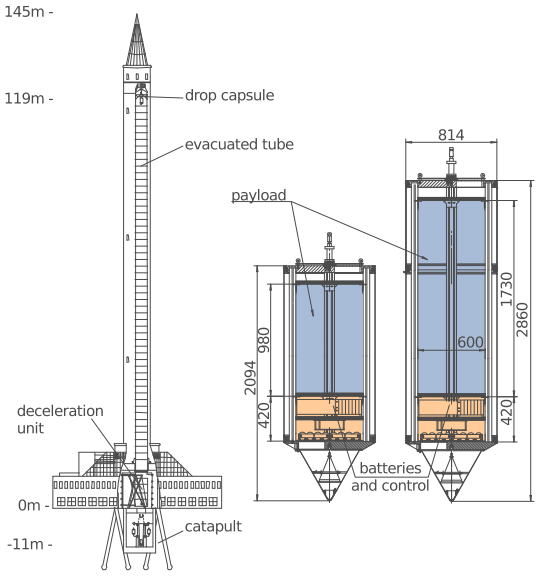

Figure 3.1: Schematic of the drop tower in Bremen (left) and the available experiment capsules (right). The 119 m tall metal drop tube is installed within a concrete tower. A catapult at the bottom of the drop tube allows for shooting up the experiment. The drop tube has to be evacuated. Two capsule sizes are available: a small catapult capsule that is used for QUANTUS-2 (left) and a larger drop capsule that was used for the predecessor experiment (right). The available volume for the payload inside the capsule is marked in blue. The area marked in orange is reserved for the capsule support and batteries. (picture taken from [95])

guiding, the center of mass must not divert more than one millimeter from the central symmetry axis. The placement of the components and subsequent taring of the capsule is crucial to make sure that the capsule is flying in a controlled fashion. Last, compared to the flight in drop mode, stronger capsule rotations are induced when catapulting the experiment. Rotation rates of up to $0.9\,^\circ\,\mathrm{s}^{-1}$ could be observed using a fiber-gyro inertial measurement unit [*iMar iIMU-FCR-03*].

After the capsule has been recaptured in the deceleration container, the tower has to be vented again. Usually this takes around 30 min. The capsule can then be salvaged from the deceleration container and is brought back to lab for battery charging and inspection. The whole drop routine from lab-to-lab takes around three hours. This allows for a maximum of three drops or two catapult flights per day.

Given all these boundary conditions, we end up with the following critical requirements defined for the experimental setup in catapult operation:

- maximum payload weight: 164 kg
- maximum volume of experiment: 341 L
- maximum acceleration during launch: 40 g
- maximum acceleration during recapture: 50 g
- center of mass within one millimeter from central axis
- remote controllable
- battery powered

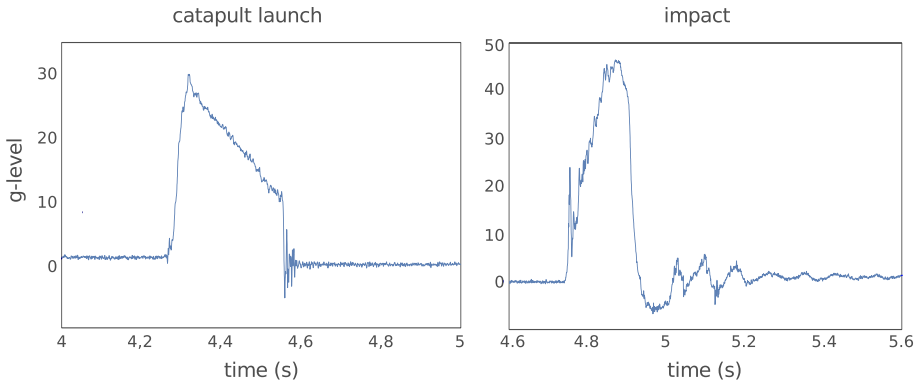

Figure 3.2: Accelerations during a catapult launch (left) and the impact in the deceleration container (right). (picture taken from [95])

In the following sections the crucial technical concepts will be introduced.

3.2 Capsule infrastructure

An overview of the catapult capsule is shown in Fig. 3.3. The basic structure consists of four aluminum stringers, freely configurable platforms, a capsule base housing the capsule control system and batteries. Not shown are the nose cone, the outer hull and the capsule lid. The whole capsule is pressurized at one atmosphere to facilitate cooling by air convection. Furthermore, none of the diode lasers are encapsuled and as a consequence, are not designed to run in a vacuum environment.

3.2.1 Capsule base and batteries

The capsule base not only constitutes the mechanical foundation of the entire capsule structure, but it also houses a bulk of the batteries and a PXI[1] system that serves as a capsule control system. Usually the capsule control system is used for most of the monitoring and control of a drop tower experiment. Because of the complexity of the QUANTUS-2 apparatus, however, a second PXI system for controlling the experiment is installed. A whole set of rechargeable batteries are housed in the capsule base providing different voltages in the range of $+1\mathrm{S}, \pm 2\mathrm{S}, \pm 4\mathrm{S}$ and $\pm 6\mathrm{S}$, with S being the nominal voltage of 3.2 V for the used batteries [*lithium iron phosphate batteries* ($LiFePo_4$)]. The usage of this extended set of rechargeable batteries was necessary due to the fact that the custom-made laser electronics need a whole range of different voltages for operation. The generation of the different voltages from a higher main voltage by using voltage regulators or switched-mode DC/DC converters was neglected

[1] PCI extensions for instrumentation

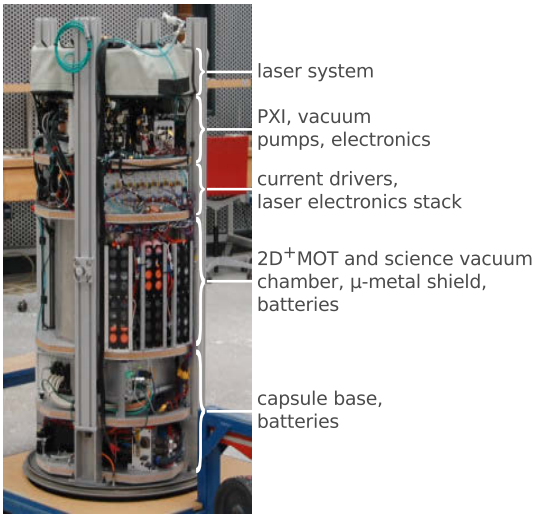

Figure 3.3: Overview of the catapult capsule. The capsule base houses a control computer, batteries and read-out electronics. On the next platform the 2D$^+$MOT and the science vacuum chamber are integrated within a two-layer mu-metal shield. Located above are the current drivers for the atom chip and coils as well as the laser electronics stack. The platform above houses the vacuum pumps as well as additional electronics. The laser system is sitting on top of the capsule.

because of their high power dissipation or generation of high frequency voltage noise, respectively.

3.2.2 PXI real-time control system

The timing and experiment sequence control as well as most of the data acquisition is done by a dedicated PXI system [*NI PXI-1036DC*], which is equipped with a real-time controller [*NI PXI-8101*]. The centerpiece is the FPGA[2] controller [*NI PXI-7854R*]. It outputs digital triggers, creates analog control voltages, e.g. for the atom chip and Helmholtz coil current drivers and also provides the digital interface for the laser system electronics stack. The FPGA controller is running at a clock frequency of 50 MHz, thus yielding a timing resolution of 20 ns. An arbitrary waveform generator [*NI PXI-5421*] creates the radio frequency ramps for the evaporation. The two cameras of the absorption imaging are read out by camera-link frame grabber cards [*NI PXI-1428*]. An analog out and digital in/out card [*NI PXI-6723*] is used mostly for controlling RF attenuators for the laser system and the evaporation. The experimental sequence start is triggered by an integrated circuit single-axis accelerometer as soon as the experiment transitions into microgravity.

3.2.3 Thermal design

Most of the electrical components with a high power dissipation, like the PXI control computer and the laser system electronics stack, are air-cooled by means of fans. During drop operation, the capsule is closed air-tight within a metal hull. Without

[2] field-programmable gate array

external cooling, the temperature inside the capsule would rise rapidly. Care has been taken to transport the accumulated heat out of the experiment. To this end, a water cooling system has been installed in the capsule. Water in- and outlets are mounted in the capsule lid and allow to attach the capsule cooling system to an external chiller while being connected to the umbilical during drop tower evacuation. The water is flowing through a series of copper thermal couplers mounted to critical parts such as the laser system distribution module, the PXI control computer and the capsule platforms and stringers. In this way, a major part of the produced heat can be removed from the capsule and temperature sensitive components are thermally stabilized. Anyhow, parts of the capsule like the mu-metal shield heat up to temperatures of about 30 °C during drop tower operation but the most critical parts like the laser system keep a temperature of about 23 °C. During lab operation the capsule is connected to a dedicated lab chiller with the outer hull and lid removed to facilitate convective cooling.

3.3 Vacuum system and atom chip

A technical drawing of the vacuum chamber is shown in Fig. 3.4. The centerpiece of the vacuum system is the science chamber, which houses the atom chip. Attached to the chamber are three pairs of Helmholtz coils to produce homogeneous magnetic fields. The science chamber has in total eight optical accesses including one big front window located opposite of the atom chip. These accesses are used for coupling in collimated laser light for the optical cooling, interferometry and detection. For faster loading of the magneto-optical trap (MOT) inside the science chamber, a $2D^+$MOT is connected to the science chamber. The $2D^+$MOT has an axial setup in which the atoms are getting cooled in two transversal directions [96]. In addition to this classical 2D-MOT operation, the $2D^+$MOT allows for an additional cooling in the axial direction by two counterpropagating beams called pusher and retarder. Due to a lower power in the retarder beam in respect to the pusher beam, the atoms get pushed along the axial direction into the science chamber. By adjusting the power ratio between pusher and retarder, one can tailor the velocity distribution of the produced cold atom beam for optimal loading of the 3D-MOT. A differential pumping stage interconnects both chambers and allows for a vacuum pressure difference of up to three orders of magnitude. In this way the rubidium vapor pressure in the $2D^+$MOT is high enough to ensure an optimal flux of precooled atoms and on the other hand allows for an ultra-high vacuum pressure in the science chamber to reduce unwanted collisions of the atomic ensemble with background atoms. Interferometry light can be coupled into the vacuum chamber from the top of the science chamber. The collimated light is pointing downwards and is being retroreflected by a mirror and a quarter-wave plate located underneath the science chamber.

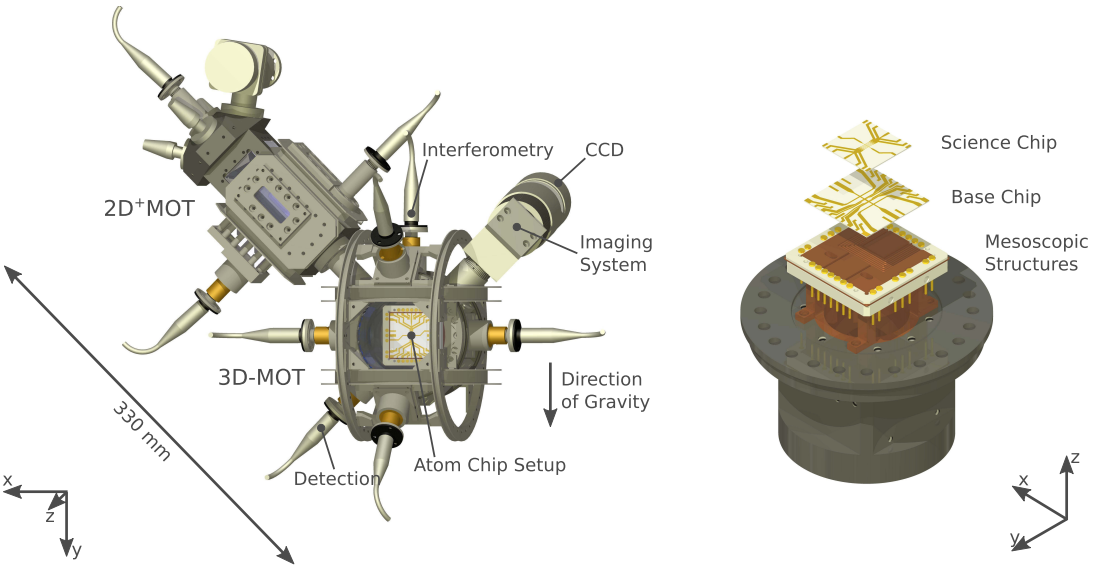

Figure 3.4: Technical drawing of the vacuum system (left) and the three-layer atom chip (right): The second detection system, which sits in front of the large window of the 3D-MOT chamber, is not shown. Mesoscopic copper wire structures constitute the lowest level of the atom chip. They are used for the quadrupole field of the MOT and the first magnetic trap. Glued on top are the base chip and the science chip. (adapted from [80])

Since the atoms are sensitive to magnetic fields, the 2D$^+$MOT and science chamber, the oven as well as the detection optics are housed inside a two-layer mu-metal shield.[3] The shielding factor of the two-layer magnetic shield has been simulated to be around a factor of 12 000 in the radial direction and a factor of about 6000 along the axial direction of the cylindrical capsule [97]. Measurements, however, showed that the attenuation is a lot less than simulated, reaching values of between 220 to 660 in the radial and 120 along the axial direction [78]. All the components inside the mu-metal shield are made from non-magnetic metal. Vacuum components located outside the mu-metal shield include a UHV sensor [*Pfeiffer IKR270*], an ion pump [*Vinci Meca 2000 PID 25, modified*], a passive pump [*SAES Getters CapaciTorr D200*] and a titanium sublimation pump [*VG Scienta SBST110*]. Together these allow to keep the pressure inside the science chamber below 10^{-10} mbar.

The heart of the QUANTUS-2 experiment is the atom chip [90, 98, 99]. It offers the possibility to create a variety of magnetic potentials with steep gradients at low power consumption. Available trapping frequencies in the low kilohertz regime allow for a fast evaporation and rapid BEC production. While the first generation experiment QUANTUS-1 used a single atom chip, the new generation features a three layer setup

[3] Mu-metal is a soft-magnetic alloy of very high permeability.

consisting of mesoscopic structures and two atom chips called "base" and "science chip". Furthermore, the surface of the chip is reflection coated. This is necessary since the MOT in the science chamber is created by mirroring one pair of the MOT beams over the chip in a 45° angle. This "mirror MOT" scheme allows for cooling in all three spatial dimensions with just two MOT beam pairs [100]. Furthermore, it allows for a reflection of one of the absorption detection beams on the chip surface. The mesoscopic atom chip structures are formed by copper wires and are used in conjunction with the Helmholtz coils to create the magnetic quadrupole field for the MOT using a U-structure as well as for the initial magnetic trap with an H-structure. Thanks to the mesoscopic wires, there is no need for Anti-Helmholtz coils. High coil currents are usually necessary for the creation of sufficient large magnetic field gradients and in consequence, due to high power dissipation, an active cooling of the Anti-Helmholtz coils is necessary. The base and science chip have dimensions of $35 \times 35\,\mathrm{mm}^2$ and $25 \times 25\,\mathrm{mm}^2$, respectively. Both chips feature an aluminum nitride substrate with electroplated gold structures. The science chip features the more delicate wire structures with a width of the central wires of $50\,\mu\mathrm{m}$. Both chips are sitting on top of the mesoscopic chip structure and offer a plethora of different magnetic field gradient configurations. Z-like wire structures are used in this experiment for the magnetic trap. A dedicated U-structure of the base chip is used as a radio frequency antenna for the evaporation.

The atom chips are delicate structures regarding the maximum current they can handle. The base and science chip are rated for a maximum current of 6 A and 2 A, respectively. To make sure that the chips are not destroyed by excessive currents, a programmable chip fuse is taking care of electronically limiting the currents by disconnecting the structures when exceeding a certain value. Furthermore hardware fuses are installed, in case that one of the electronic circuitries fail. Moreover a programmable timing circuit takes care that the chip fuse is just open for a limited amount of time. The timing firmware is programmed onto a CPLD[4]. Residual output generated by the current drivers in idle state will create spurious magnetic fields. Especially magnetic field gradients will disturb the atoms after the release from the trap. To suppress these residual current, the atom chip structures as well as the coils can be electronically disconnected by means of solid-state relays to reduce unwanted magnetic fields. This is important especially for longer sequences in microgravity, where the influence of residual magnetic fields become evident. Last but not least, the chip fuse offers the possibility to measure the currents running through the chips and coils, which is useful for monitoring the sequence and error diagnostics.

The currents for all the chips, coils and the mesoscopic U-structure are supplied by a set of six individual low-noise current drivers [*HighFinesse BCS, modified*]. The currents for the $2D^+$MOT and the mesoscopic H-structure are supplied by custom-

[4]Complex programmable logic device.

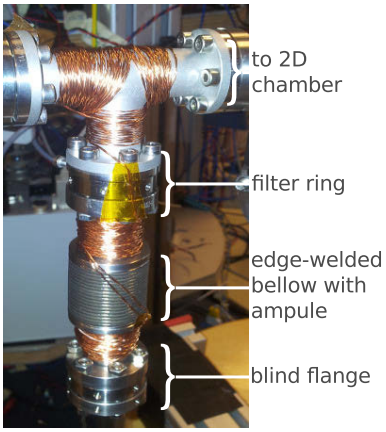

Figure 3.5: Picture of the oven setup: The rubidium ampule is held inside an edge-welded bellow that can be flexed to break the ampule. Insulated copper wire allows for heating up the oven to a desired temperature of around 60 °C. A filter ring made of sintered bronze is sitting above the ampule to prevent substantial lumps of rubidium leaking from the oven. A cylindrical cover mounted around the oven fixes the bellow (not shown in picture).

made current drivers since the requirements regarding the noise level are more relaxed for these two current drivers [101]. The current drivers for the coils and atom chip are supplied by dedicated batteries to achieve the lowest possible current noise level at the output of the drivers by isolating the individual current drivers galvanically. These additional batteries are distributed around the mu-metal shield.

3.4 Oven

The initial Swagelok-based oven concept used in the lab did not have the capability to withstand the accelerations during a catapult flight. It has been replaced by an edge-welded bellow based oven. The oven section is attached to the 2D$^+$MOT via an intermediate all-metal valve to allow replacing the oven without breaking the vacuum on the 2D and 3D chamber side. Later, this will become important when a second oven will be installed for potassium. A twisted heating wire wound around the oven allows for heating it up to increase the rubidium partial pressure in the 2D$^+$MOT. At an oven temperature of around 60 °C, the partial pressure is sufficient for the operation of the 2D$^+$MOT. A higher temperature would increase the risk of contaminating the 2D chamber with excessive rubidium. A glass ampule filled with rubidium is held within the bellow. After attaching the oven and subsequent baking out and vacuum pumping, the ampule has been broken by flexing the bellow. To prevent broken glass or substantial amounts of rubidium from moving outside the oven, a filter of sintered bronze is placed above the oven. The oven setup is depicted in Fig. 3.5. For sake of completeness it should be mentioned that there are also three dispensers attached to the 2D$^+$MOT – two for rubidium and one for potassium. However, the dispensers did not allow an operation without deteriorating the vacuum quality inside the science chamber.

3.5 Detection systems

The atomic ensembles can be detected by either a fluorescence detection or one of two absorption imaging systems.

3.5.1 Fluorescence detection

To detect fluorescence of the atoms, collimated light resonant with the transition $|F = 2\rangle \rightarrow |F' = 3\rangle$ is subjected to the atoms via the detection port of the 3D chamber. The isotropically irradiated fluorescence light is focused by a lens system onto a photodiode [*Hamamatsu S5107*]. The lens system with the photodiode is located at the large window in front of the atom chip. The photocurrent is transformed to a voltage U by means of a transimpedance amplifier [*Femto DLPCA-200*] with a programmable transimpedance gain G. From the measured voltage U, the known solid angle covered by the photodiode Ω, the spectral responsitivity S as well as the scattering rate γ one can calculate the atom number

$$N = \frac{4\pi \cdot U}{\Omega \cdot S \cdot G \cdot \hbar\omega \cdot \gamma}, \tag{3.1}$$

with the scattering rate being

$$\gamma = \frac{\Gamma}{2} \frac{I/I_{\mathrm{sat}}}{1 + 4(\Delta/\Gamma)^2 + (I/I_{\mathrm{sat}})}. \tag{3.2}$$

Here, Δ denotes the detuning from resonance, I_{sat} the saturation intensity and Γ the natural linewidth. For most of the time the fluorescence detection was used for monitoring of the MOT or optimizing the performance of the experiment with an evolutionary algorithm [102], without having the need to evaluate absorption images. However the main part of this work will deal with data taken with the absorption imaging systems.

3.5.2 Absorption imaging

Information about the fraction of condensed atoms, the size, position and shape of the ensemble is essential. To get quantitative values for these properties, two absorption imaging systems have been installed. The first absorption detection is oriented in a 45° angle in respect to the interferometry beams. It is thus impossible to detect spatial fringes arising from two overlapping condensates after Bragg interferometry in an asymmetric Mach-Zehnder configuration. A second imaging system has been installed with the detection beam propagating in the horizontal plane to allow for the imaging of spatial fringes (see Fig. 3.6). Since the access ports in the horizontal plane of the science chamber are already occupied by the MOT telescopes, the imaging beam

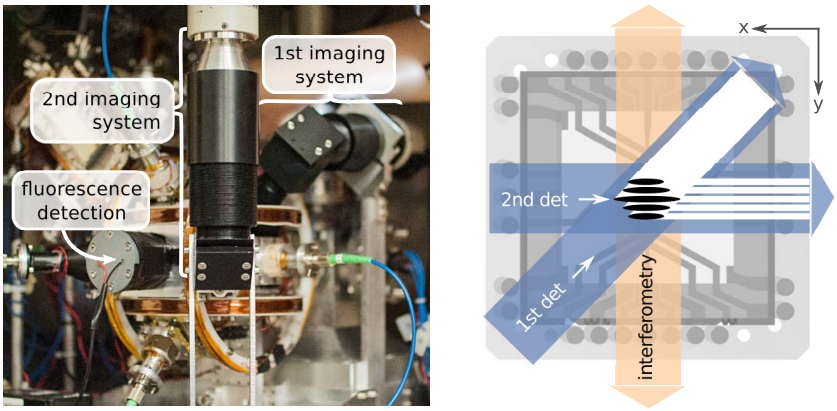

Figure 3.6: Picture of the two absorption imaging systems and the photodiode for the fluorescence detection (left). The photodiode sits directly in front of the large window of the science chamber facing the atom chip. (right) Facing the front of the chip, the 1st detection points upward in a 45° angle along the chip. In contrast to the second detection, the first detection cannot resolve spatial fringes of two overlapping condensates after Bragg interferometry. The 2nd detection is reflected in the horizontal plane over the chip.

is inputted via the big window in front of the atom chip and reflected over the surface of the atom chip. In this way it will be also possible to get information about the position, size and shape of the ensemble in all three dimensions.

Both absorption imaging systems make use of a digital CCD camera [*Hamamatsu C8484-15C*]. These offer a pixel size of 6.45 µm, a dynamic range of 12 bit and a resolution of 1344×1024 pixel. Due to a magnification of the two-lens imaging system by a factor 1.8, the absorption images taken have an effective pixel size of 3.58 µm. The imaging system has a resolution limit of about 5.52 µm [78]. Although care has been taken to mount the absorption imaging systems in the most rigid way, there is still a movement of the visible frame after each impact or catapult launch. To correct for these translations, a position correction routine takes care of rotating and translating the absorption pictures to a predefined frame to ensure reproducible position results. Interference fringes created by impurities on the vacuum windows serve as reference points for the position correction routine.

The interplay between both imaging systems has not yet been fully understood and is subject of further investigations. An influence on the position and atom number as well as an additional heating of the condensate has been observed when using both imaging systems in conjunction. Due to the fact that there exists no common magnetic quantization field for both imaging systems, only one imaging system has been used at a time within this thesis. The second detection imaging system has been used mostly just to acquire qualitative information due to the reflection of the detection beam over the chip [103]. The two absorption imaging systems as well as the fluores-

cence detection are depicted in Fig. 3.6.

After having introduced the most important components of the physics package, we will now focus in Chapter 4 on the catapult-capable laser system before we turn to the first results achieved with the experimental setup in microgravity in Chapter 5.

4 Catapult-capable compact rubidium laser system

In the following chapter, the catapult-capable QUANTUS-2 rubidium laser system will be described. The construction, setup and testing of the system constitutes a major part of work within this thesis. After a description of the requirements defined for the laser system, a design will be deduced from these, followed by the description of the subcomponents. The last part of this chapter is dealing with the novel ultra-compact laser system electronics. Within this thesis we will deal mostly with the rubidium subpart of the complete system. While the production of the potassium system is already under way, the documentation and description of it will be left for future publications. Anyhow, a short description of the main differences of the potassium system shall be given at the end of this chapter.

4.1 Requirements and concept

The design of the rubidium laser system is heavily influenced by constraints set by the catapult capsule. Following requirements had to be met:

- **Volume:** Most of the volume of the capsule is occupied by the physics package including the vacuum chamber and pumps, control computers as well as batteries and electronics. A volume of about 46 liters in the upper part of the capsule has been reserved for the laser system – excluding the laser system electronics.
- **Payload mass:** The total payload mass should not exceed 164 kg. Since the motion of the catapult piston during launch is controlled and matched to the capsule weight, any additional mass will result in an unwanted reduction of microgravity time during a catapult flight.
- **Power efficiency:** During drop and catapult campaigns, the whole experiment will be battery-powered. The lasers thus have to provide sufficient optical output power at lowest electrical power consumption possible. An experiment uptime of about two hours with the whole laser system running provides sufficient time for a drop or catapult routine.
- **Mechanical stability:** The mechanical stability is of utmost importance due to the fact that the catapult capsule will be subjected to accelerations of up

to 40g during catapult launch and 50g at recapture. Not only should the laser system withstand these accelerations without mechanical failure but also the laser frequency locks as well as the optical power at the output of the laser system has to be stable enough to ensure experiment operation immediately after the catapult launch.

- **Optical output power:** The laser system should generate an optical output power of 60 mW of cooling light for optimal 3D-MOT operation and 70 mW of cooling light for the $2D^+$MOT, whereas a higher output power for the $2D^+$MOT would increase the atomic flux and is therefor desired. Few milliwatt of repumping light are sufficient for operation of both magneto-optical traps. Both absorption imaging systems require an optical power of about 2 mW.
- **Spectral properties of the lasers:** The frequency of the lasers should be dynamically tunable over a range of few gigahertz to reduce the number of necessary lasers. Furthermore the emission linewidth should be about or less than 1 MHz to allow for efficient laser cooling and to reduce systematic effects during atom interferometry.
- **Phase-locked interferometry light:** Two light fields with a phase-locked frequency difference are necessary to drive stimulated two-photon transitions in a Raman or Bragg scheme. An optical power of 10 mW for each beam is sufficient, whereas a higher output power of the Bragg beams will allow for driving high-order transitions.

Due to the strict demands made by the drop tower environment, the laser system design is for the most part based on custom-made components since commercial parts were not available within the intended form factor. Micro-integrated laser modules are the key component of the laser system. They are based on distributed-feedback laser diodes and offer a sufficient narrow linewidth. To increase the power of the light emitted by the distributed-feedback laser diodes, a master oscillator power amplifier (MOPA) setup on a micro-integrated optical bench is being used. The design and production of these modules was done at the Ferdinand-Braun-Institut Leibniz-Institut für Höchstfrequenztechnik (FBH) in Berlin. The light emitted by the micro-integrated lasers is subsequently distributed using a concept incorporating free beam optics on compact breadboards as well as polarization maintaining fibers and fiber splitters.

In a typical lab experiment, substantial volume is taken up by the laser system electronics. A reduction in volume by a factor of 16 compared to electronics used within QUANTUS-1 could be achieved by making use of custom-made driver and controller cards in the PC104 form factor. They were developed by Dr. Thijs Wendrich at the Leibniz Universität Hannover. The cards can be stacked onto each other and feature a common bus for the communication and signal transmission.

After having introduced the general concept of the laser system, we will now turn to a detailed description of each subcomponent.

4.2 Laser modules

In the following sections, the diode laser modules will be introduced. Starting with a description of the underlying distributed-feedback laser diode technology, we will then turn to a detailed description of the master laser as well as the micro-integrated laser modules.

4.2.1 Distributed-feedback laser diodes

The QUANTUS-2 laser system makes exclusive use of diode lasers. Due to their compact form factor, low power consumption and intrinsic mechanical stability, they are an excellent choice for mobile cold-atom experiments. Anyhow, standard Fabry-Perot-type semiconductor lasers do not offer the longitudinal single-mode operation, narrow linewidth and reproducible wavelength tunability. Many cold atom experiments are relying on external cavity diode lasers (ECDL), which feature a mode selection by means of an external resonator [104]. Although ECDLs feature a narrow linewidth and compact size, they usually lack in mechanical stability due to the external resonator.

An alternative concept with a monolithic compact design is a distributed-feedback semiconductor laser (DFB). By processing a modulation of the refractive index in the active region of the semiconductor, single-mode operation can be achieved [105]. A reproducible tuning of the wavelength is then possible by setting the temperature of the laser diode and adjusting the injected current. Typically, a DFB laser offers a mode-hop free wavelength tuning over the full injection current range. Furthermore, a reduction of the linewidth down to a short-term linewidth (10 µs) of 1 MHz and a Lorentzian linewidth of about 100 kHz at injection currents of about 150 mA is possible with the diode chips used within this work [106].

4.2.2 Master laser

One master laser is providing an absolute frequency reference for each used atomic species. Three micro-integrated MOPAs are in turn stabilized in their optical frequency onto the master laser. An overview of the rubidium master laser is given in Fig. 4.1. The optical bench of the master laser is made of aluminum. The DFB master laser is fixed together with collimation optics on a micro-optical bench, which itself is glued onto a micro-Peltier element for controlling the temperature of the laser diode. The integration and collimation of the laser diode on the micro-optical bench was done at the FBH in Berlin. A double-stage micro isolator prevents reflected light from

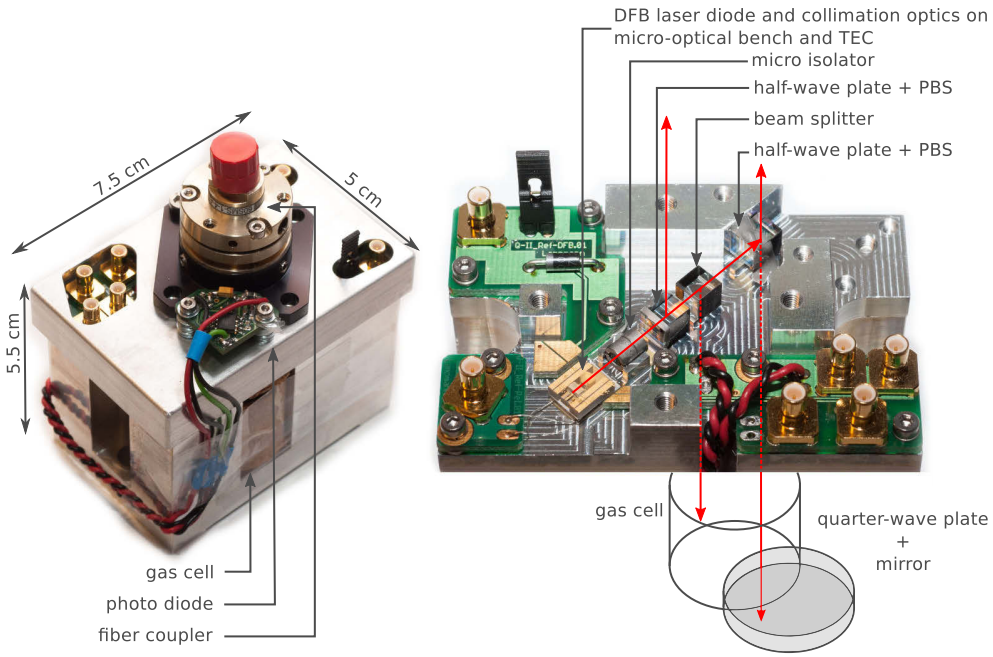

Figure 4.1: Rubidium master laser: Overview (left) and the optical bench (right). Light from the DFB laser diode passes through a micro-optical isolator. The bulk of the light is sent upwards for fiber coupling. A small fraction of the light is sent downwards for Doppler-free and Doppler-broadened spectroscopy (not implemented for rubidium). After passing a gas cell and being retroreflected, the light is sent onto a photodiode.

coupling back into the laser diode. Beam splitters distribute the main part of the light into a fiber coupler [*Schäfter+Kirchhoff SMS60*] sitting on top of the lid, while sending a small part of the light to a spectroscopy gas cell located underneath the optical bench. Half-wave plates have been glued onto the optical isolator and beam splitters to adjust the optical power in the spectroscopy path. Electrical contacts for the laser diode current, the photodiode supply voltage, the photodiode signal and the Peltier element as well as the temperature sensor are located on the optical bench.

The optical bench sits on top of the base body, which is as well made of aluminum. The spectroscopy gas cell with a length and diameter of 2.5 cm sits inside the base body. The spectroscopy light is propagating downwards through the gas cell before being retroreflected upwards by a mirror and quarter-wave plate to allow for Doppler-free absorption. Frequency modulation spectroscopy is being used to create a dispersive error signal for stabilizing the master laser onto an atomic transition [107]. Therefor, the master laser injection current is being directly modulated. After passing the gas cell, the modulated Doppler-free absorption signal is detected with a photodiode [*Hamamatsu S5971*]. A transimpedance amplifier circuit, which is mounted together

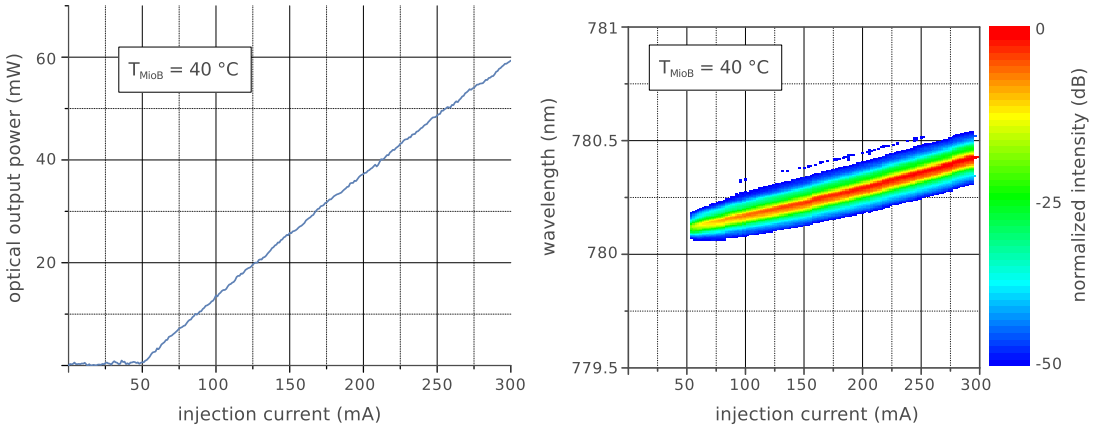

Figure 4.2: Optical characteristics of the master laser: Optical output power behind the two-stage optical micro isolator versus laser diode injection current (left). Optical emission spectrum versus laser diode injection current (right). The laser shows a mode-hop free emission spectrum over the full injection current range [108].

with the photodiode itself in the lid of the master laser, generates the spectroscopy signal from the photo current. The demodulation of the spectroscopy signal and frequency locking is then handled by the laser system electronics (see Sec. 4.4.2).

The laser diode temperature is stabilized by means of a Peltier element to 41 °C. At this temperature the laser diode runs on the rubidium D_2 line when being injected with a current of 110 mA. This yields an optical output power of 17 mW behind the optical isolator from which around 200 µW are used for the spectroscopy. Specifications for the optical output power as well as the emission spectrum are shown in Fig. 4.2. The complete master laser weighs 340 g including the fiber coupler and has dimensions of $7.5 \times 5.5 \times 5$ cm^3.

4.2.3 Master oscillator power amplifier

Although the spectral characteristics of the DFB laser diodes are appropriate for the envisaged experiments, the optical output power is insufficient. A widely used concept solving this problem is the master oscillator power amplifier (MOPA) setup. To boost the optical output power of a master oscillator (MO) while preserving its spectral characteristics, a tapered amplifier (TA) is used as an optical power amplifier (PA). A tapered amplifier is a semiconductor device offering an active gain region within a monolithic semiconductor chip. The in- and output facets are anti-reflection coated. When injected with a forward current, light coupled into the tapered amplifier is being amplified while the spectral characteristics are preserved. At the input side, the active region is tapered and features an increasing width towards the output to prevent

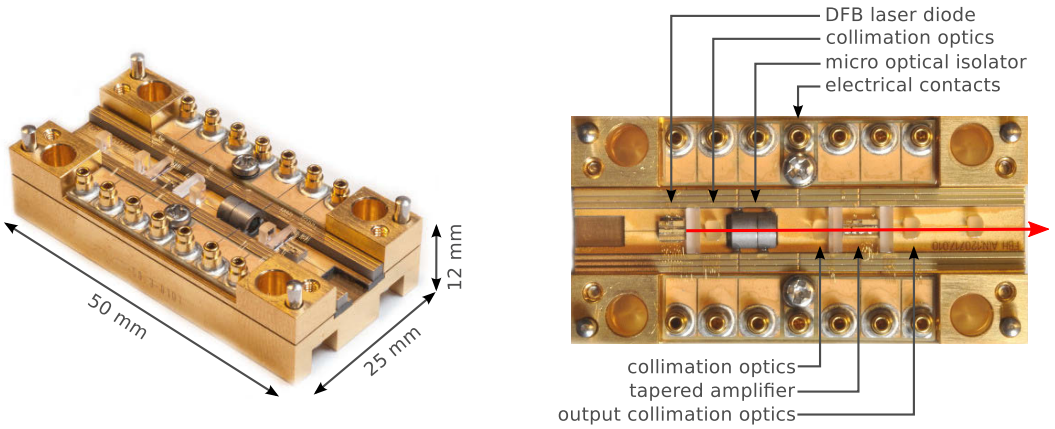

Figure 4.3: Second generation micro-integrated master oscillator power amplifier (MOPA). The aluminum nitride micro-optical bench incorporates a DFB laser diode, a micro optical isolator, optical amplifier and collimation optics. The MOPA yields an optical output power of about 1 W at a wavelength of 780 nm.

thermal damage inflicted by the increasing optical power density. An optical isolator between the master laser and the tapered amplifier prevents reflected light getting coupled back into the master laser. In a usual lab environment, a MOPA setup is realized on an optical table with macroscopic free beam optics for coupling the light between the master laser and the amplifier and collimation of the output light. Not only is such a setup unsuitable regarding its size but also does it lack in mechanical stability. A MOPA setup based on a micro-integrated concept has been developed by the FBH [109, 110]. It features a small footprint with a high mechanical stability and output power.

Hybrid-integrated setup

The complete MOPA setup is incorporated on a gold-plated aluminum nitride micro-optical bench with a footprint of $50 \times 10\text{mm}^2$. A 1.5 mm long single-quantum-well DFB laser diode serves as the master oscillator. Its front and rear facet are 0.1 % and 95 % reflection coated, respectively. Two cylindrical lenses are placed at the output of the DFB to collimate the light. After passing a single-stage optical isolator with an isolation of > 35 dB, the light is coupled into a tapered amplifier by means of two cylindrical lenses. The tapered amplifier consists of a 1 mm long straight ridge-waveguide section that acts as a mode filter, followed by a 3 mm long tapered section. Both power amplifier diode sections share a common n-contact, while individual p-contacts offer the possibility to inject separately tunable currents for the ridge-waveguide and tapered section. The input and output facets are 0.1 % reflection coated. Due to the tapered profile of the gain region, the output light of the tapered amplifier shows a

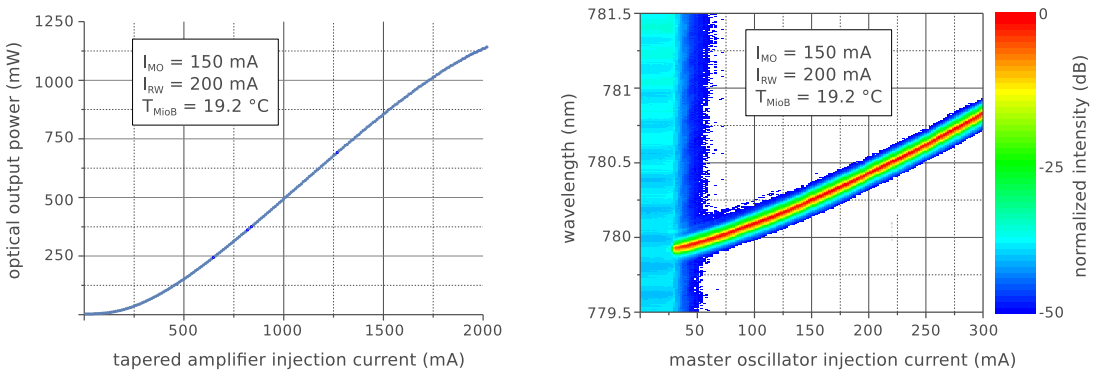

Figure 4.4: Optical characteristics of the MOPA: Optical output power versus tapered amplifier injection current. The output power is increasing almost linearly with a slight thermal roll-over starting at currents above 1.7 A (left). Optical emission spectrum versus DFB injection current (right). The DFB shows a mode-hop free emission spectrum over the full injection current range [108].

strong astigmatism at its output. Three cylindrical lenses are used to achieve a circular collimated output beam.

The bench is mounted within a gold-plated copper mount with dimensions of $25 \times 50 \times 12\text{mm}^3$. The mount offers electrical connections and is stabilized in its temperature with a Peltier element. The complete MOPA package weighs 84 g. Pictures of the MOPA setup are shown in Fig. 4.3. All rubidium MOPAs have been produced by Max Schiemangk at the FBH. A more detailed description of the MOPAs can be found in his dissertation [111].

Spectral and optical characteristics

The spectral characteristics of the emitted light at the output of the MOPA are governed by the Lorentzian linewidth of the DFB, which reflects the fundamental properties of the laser as well as a Gaussian contribution that arises from technical noise. The Lorentzian linewidth decreases with the optical output power and reaches a value of about 110 kHz at an injection current of 150 mA. The short-term (10 µs) noise attributed to technical noise contributes a width of about 1 MHz. The DFB offers a mode-hop free wavelength tuning over the full injection current range.

The MOPA is temperature stabilized to about 20 °C. At this temperature the DFB is emitting light at a wavelength of about 780.24 nm with an injection current of about 150 mA. The output power of the DFB is sufficient to operate the tapered amplifier in a well saturated regime to limit the influence of fluctuating seeding power on the MOPA output power. The emitted light has been collimated while running at an output power of 1 W at a tapered amplifier injection current of 1.7 A. An optical

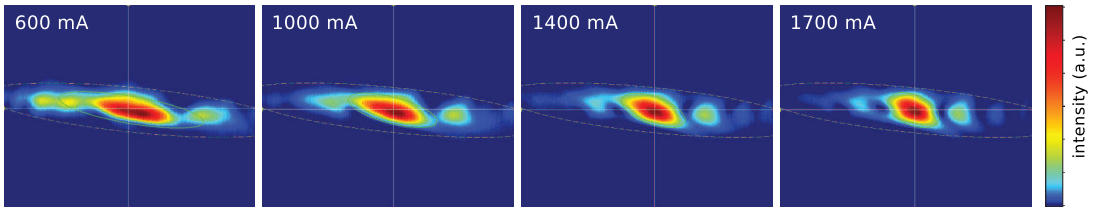

Figure 4.5: Intensity profiles of the MOPA output beam for different tapered amplifier injection currents. Best fiber coupling efficiencies could be reached at 1700 mA, for which the laser has been collimated at production. At lower currents the output beam is elliptic and shows side lobes. All pictures have been taken at a DFB (RW) injection current of 150 (200) mA.

output power of up to 3 W has been demonstrated using a tapered amplifier injection current of 4 A [109]. Due to the increased wear when running the MOPA at these high currents, TA injection currents of 1.7 A have been used in normal operation. The spectral characteristics as well as the power performance are depicted in Fig. 4.4.

As already mentioned, because of the tapered profile of the power amplifier, the output light of the MOPA shows a strong astigmatism. Since the divergence of the tapered amplifier output beam is depending on its injected current, the collimated output beam profile changes with increasing TA injection currents (see Fig. 4.5). At lower injection currents the beam profile exhibits pronounced side lobes, which vanish with increasing injection currents and reach a minimum at 1.7 A. Furthermore, the injection current of the input ridge-waveguide section of the tapered amplifier can be tuned individually. This allows for a further optimization of the output beam profile. Best fiber coupling efficiencies of up to 58 % have been achieved with standard lab optomechanics. The coupling efficiency could be even improved to 64 % using a two-lens telescope for beam expansion. Further increase of the coupling efficiency to arbitrary high values could be achieved by placing a pinhole at the position of the focus between the two lenses. However, this spatial cleaning of the transversal mode profile comes at the expense of optical power in the cleaned beam. Unfortunately there is no space for beam expansion optics in the integrated setup and general coupling efficiencies within the laser system tend to lie in the range of $30 - 40\%$.

4.3 Light distribution

The general layout of the laser system can be subdivided into the rubidium and the potassium section. Both sections are mostly a mirror-image of each other with only few slight differences. These differences will be discussed in Sec. 4.6. Each side features a master laser, a MOPA module housing three MOPAs, a distribution module and a Raman module. An overview of the laser system and its modules is depicted in Fig. 4.6.

The foundation of each module is provided by aluminum breadboards with a height

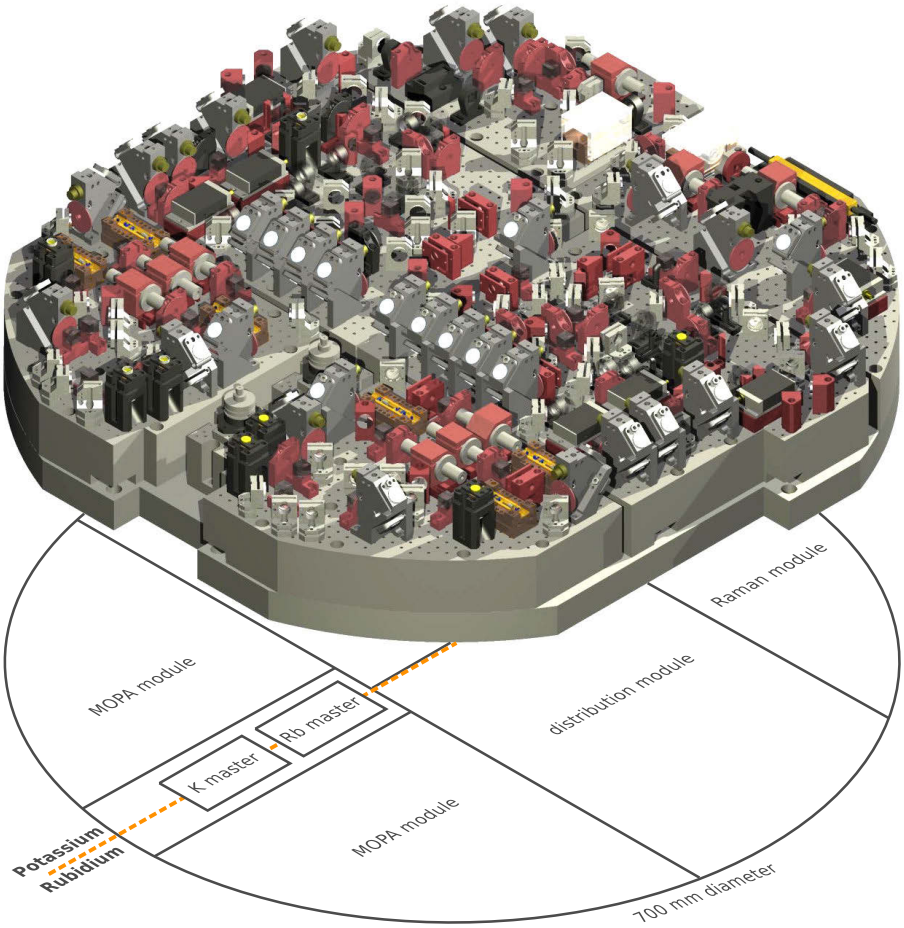

Figure 4.6: Overview of the QUANTUS-2 laser system: The laser system features three modules for each species. The MOPA module houses three MOPAs and is connected with the distribution module by optical fibers. From there the light is guided and distributed to the vacuum chamber by means of fiber splitters. For each species exists a Raman module that can be inserted between the MOPA and distribution module to provide light at the two necessary frequencies to drive stimulated Raman transitions. The optical components are fixed on honeycomb breadboards with a height of 50 mm. These are in turn fixed to the capsule platform. Two master lasers for each species provide an absolute frequency reference for the MOPA frequency offset locks.

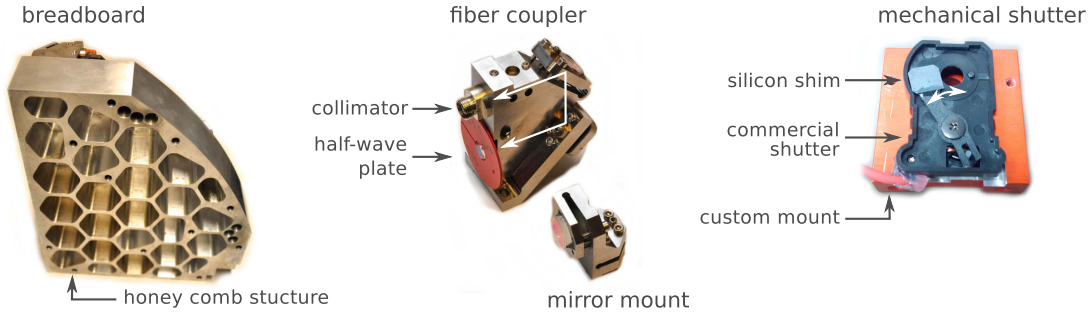

Figure 4.7: All optics are mounted on 50 mm high aluminum breadboards with honeycomb structures. Custom-made titanium fiber couplers and adjustable mirror mounts allow for superior stability and reduction in size. Mechanical shutters selectively block light from entering the vacuum chamber. The commercial shutters are fixed in a custom mount and the laser illuminated plastic part has been replaced with a silicon shim for improved power handling.

of 5 cm. These feature a honey-comb structure on the bottom side to reduce weight while maintaining the mechanical stability. All breadboards as well as the two master lasers are mounted onto a common capsule platform. Fully integrated, the complete laser system has a diameter of 70 cm a height of 12 cm, thus taking a volume of about 46 liters at a weight of about 32 kg excluding the capsule platform.

Most of the optomechanics have been custom-made to achieve a compact form factor. They also guarantee mechanically rigid free beam guiding. The adjustable flexure mirror mounts and fiber couplers are made of titanium[1]. All free beam light is guided at a height of 2 cm. The light is transferred between the modules by means of polarization-maintaining single-mode fibers [*Schäfter+Kirchhoff PMC-APC*]. Each titanium flexure mirror mount fiber coupler features a collimator with an integrated lens for mode-matching [*Schäfter+Kirchhoff 60FC*] and an adjustable half-wave plate. The fiber coupling allows for a subdivision of the laser system and thus increases the mechanical stability. Furthermore, the first fiber behind a MOPA filters the transversal mode profile and provides a clean Gaussian beam inside the distribution module. Pictures of a breadboard, an adjustable flexure mirror-mount and fiber coupler as well as a shutter are shown in Fig. 4.7.

MOPA module

The MOPA module is housing three micro-integrated MOPAs. Each MOPA is temperature stabilized by means of a Peltier element. A single-stage optical isolator [*Electro-Optics Technology*] with an isolation > 31 dB is placed behind each MOPA to prevent light from being reflected back into the MOPA. The Faraday rotator crystals

[1] Ti10V2Fe3Al, 10 % vanadium, 2 % iron, 3 % aluminum

of the optical isolator had to be glued within their mounting bracket since after some drops it became evident that the crystals became loose resulting in a degraded isolation. Few milliwatts of the MOPA light are diverted and overlapped with light coming out of the master laser fiber and focused on a fast photodiode [*Hamamatsu G4176-03*] for frequency offset locking. The major part of the light is coupled into polarization maintaining fibers for mode cleaning and to transfer the light to the distribution module. About $300 - 400$mW of optical power from each MOPA can be transferred to the distribution module.

The following tasks are handled by each MOPA:

- **MOPA1:** cooling light for the 2D$^+$MOT, absorption imaging and fluorescence detection, optical pumping for state preparation
- **MOPA2:** repumping light, Bragg interferometry beams
- **MOPA3:** cooling light for the 3D-MOT, Raman master laser

Raman module

A Raman module is provided on a dedicated breadboard. It allows for the creation of two phase-locked laser frequencies for driving two-photon transitions between the two rubidium hyperfine ground state levels via an intermediate excited level in a Raman scheme. A typical setup comprises two external cavity diode lasers (ECDL) that are phase-locked with their frequency difference equaling the hyperfine splitting of the ground state of rubidium [112]. Sufficient stable and compact ECDLs were not available during the design phase of the experiment. Thus, an alternative design based on electro-optic modulation and injection locking was conceived. It is described in depth in [113]. To generate phase-locked light with the necessary frequency difference of 6.8 GHz, MOPA3 light coming from the MOPA module can be transferred to the Raman module. The largest part of the light is looped through the Raman module, whereas about 10 mW of the light are diverted and phase-modulated in a fiber-coupled electro-optic modulator [*EOSPACE PM-0K5-10-PFA-PFA-780-UL*] with a frequency of 6.8 GHz. The first side-band of the modulated light is then used to injection lock a slave DFB laser diode [114]. This slave DFB laser diode is thus running at the desired phase-locked difference frequency. Its light is subsequently amplified in a tapered amplifier and overlapped with the untreated major part of the light from MOPA3 and sent via a fiber back to the distribution module. There, a fast photodiode [*Hamamatsu G4176-03*] offers the possibility to further stabilize the phase-lock. While the Raman module has been already characterized and tested using lab electronics, during all measurements so far, the Raman module has not yet been used to drive atomic two-photon transitions in the experiment.

Distribution module

The rubidium distribution module offers three main inputs. Two inputs are used for MOPA1 and MOPA2, whereas the third input is used for MOPA3 or, in case the Raman module is installed, for the MOPA3/Raman light. The distribution module mixes light and switches it to the desired output ports. Within the distribution module, repumping light from MOPA2 is overlapped with cooling light from MOPA1 and MOPA3 on polarizing beam splitters. Acousto-optical modulators [*Crystal Technology 3080-125*] switch the light to the desired output fiber couplers. Three AOMs are used within the distribution module. When running at 80 MHz, AOM1 provides repumping light for the 3D-MOT and AOM2 diverts overlapped repumping and cooling light to the $2D^+$MOT output. When driving AOM1 and AOM2 with 100 MHz at a small frequency difference of 15 kHz equaling the rubidium recoil-frequency for a two-photon D_2 transition, both beams can be used for creating beam splitter pulses for Bragg interferometry. After passing the AOMs, the two beams are overlapped on a polarizing beam splitter and subsequently coupled into the interferometry fiber. The AOM3 has three modes of operation. When running at 80 MHz it diverts cooling light from MOPA3 to the 3D-MOT fiber. In case that the Raman laser module is installed to create the two phase-locked laser frequencies from MOPA3 light, the Raman light coupled into the distribution module can be diverted to the interferometry output fiber coupler by running AOM3 at 100 MHz. For the case of AOM1 and AOM2 running at 100 MHz for creating the Bragg beams, AOM3 is off and just passes on the Bragg light to the interferometry output port.

To ensure a sufficient splitting of the beams for the two respective frequencies within an acceptable distance behind the AOMs, three-lens telescopes have been used (see Fig. 4.8 for the respective focal lengths). Additionally, the AOMs are used to control the optical power within the beams by attenuating the radio frequency driving the AOM by means of voltage controlled attenuators. To prevent unwanted light from entering the vacuum chamber and disturbing the atoms, mechanical shutters [*Sunnex SHT-934*] selectively block light in front of the fiber output couplers. Since the shutters are made of plastic and can handle only low power, the illuminated part of the shutter has been replaced with a silicon shim that reflects the light diffusively (see Fig. 4.7). By sending a current from the shutter driver through the shutter coil, the created magnetic field translates a permanent magnet, which in turn closes the shutter. The shutter in conjunction with the shutter controller has a reaction time of 2.6 ms and opens or closes within 0.6 ms.

Transfer of the light to the vacuum chamber

The light from the laser system is transferred to the vacuum chamber by polarization maintaining fibers or fiber splitters. A 1:4 splitter [*Canadian Instruments, custom-*

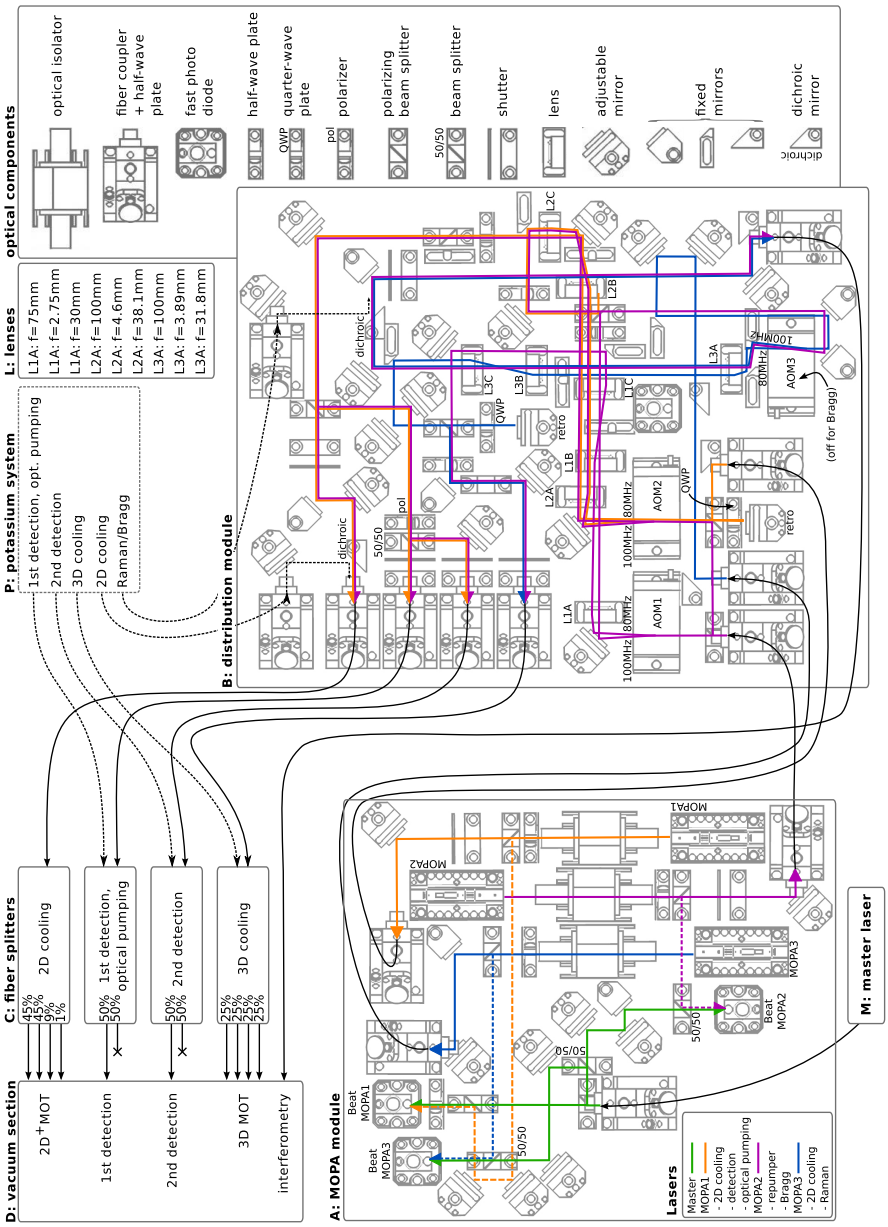

Figure 4.8: Schematic of the rubidium laser system: Part of the light from the MOPAs is overlapped with light from the master laser (M) for frequency offset locking within the MOPA module (A). From there it is transferred to the distribution module (B) via fibers. Fiber splitters (C) connect the distribution module with the vacuum chamber (D). Three-lens telescopes allow for a separation of the diffracted beams after the AOM running at two possible frequencies within a short range (L). The potassium system (P) will be integrated in a next step by connecting it to the fiber splitters and the rubidium distribution module.

made] based on evanescent coupling with an equal splitting ration of 25 % is used for the 3D-MOT. Later on, it will be replaced by a similar splitter [*Evanescent Optics, custom made*] that offers dual-wavelength operation. It will feature two inputs – one for rubidium and one for potassium. The 2D$^+$MOT requires a power splitting ratio of about 45 % for the two transversal directions and 9 % and 1 % for the pusher and retarder, respectively. Since no fiber splitters with two separate inputs were available that offer the right splitting ratio for two different input wavelengths, the potassium 2D cooling light had to be first overlapped with the rubidium 2D cooling light someplace before. Therefor, the potassium 2D cooling light is transferred from the potassium distribution module to the rubidium distribution module, where it is overlapped with the rubidium 2D cooling light on a dichroic mirror. This overlapped light is then coupled into the 2D-splitter [*OZ Optics FOBS*] that distributes the light in the desired ratio to the four output ports.

The distribution module features two separate output ports for detection light. Each port features a fiber splitter [*Evanescent Optics, custom-made*] offering two inputs for rubidium and potassium and two outputs from which only one will be used. The splitters are designed for a splitting ratio of 50:50 at a center wavelength of 774 nm. During the time of this thesis the potassium laser system had not yet been installed and simple fibers were used for the detection light. The potassium interferometry light can be coupled from the potassium distribution module into the rubidium distribution module where it is overlapped with the rubidium interferometry light on a dichroic mirror. The overlapped light is then coupled into a single fiber and sent to the vacuum chamber. An overview of the rubidium side of the laser system is shown in Fig. 4.8.

As a consequence of loss of optical power mostly at fiber couplings and acousto-optic modulators, only a fraction of the 1 W optical output power generated by the MOPAs arrives at the vacuum chamber. About 90 mW of cooling light are available within the 2D$^+$MOT and 70 mW in the 3D-MOT. The repumping light contributes about 5 % to this light. Both detection fibers transfer about 2 mW each to the science chamber. The interferometry capabilities of the laser system have not yet been used within the work of this thesis but an optical power of 2×20 mW of crossed polarization Bragg light has been coupled into the interferometry fiber. The most relevant specifications of the laser system are summarized in Tab. 4.1.

4.4 Laser system electronics

The electronics accompanying a laser system usually contribute a substantial part to the overall volume of an atom-optical experiment. Considerable development efforts were made to provide a remote-controlled system with reduced size, weight and power consumption. Therefor, a novel concept for all the electronics was designed that is based on a whole set off individual electronic modules. These come in the PC104 card

	parameter	value	comment
general specs			excluding electronics
	mass	16 kg	
	volume	23 L	
	power consumption	150 W	
optical output power			
	2D cooling	90 mW	
	2D repumping	5 mW	
	3D cooling	70 mW	
	3D repumping	4 mW	
	optical pumping	2 mW	
	Bragg	2×20 mW	crossed polarization
	detection	2×2 mW	for 1st and 2nd detection
spectral properties			
	short-term (10 µs)	1 MHz	[106]
	Lorentzian	100 kHz	[106], @ injection current 150 mA
max. acceleration			laser system fully functional
	catapult launch	27 g	
	capsule impact	43 g	

Table 4.1: Specifications of the rubidium laser system. The specified mass and volume exclude the laser system electronics. The laser system withstands accelerations as listed. The master laser and MOPAs are stable in respect to their frequency locks and there is no loss of optical power in the output fibers after the catapult launch or impact.

form factor with dimensions of $100 \times 100\text{cm}^2$ and can be stacked onto each other. The communication and power supply is realized via a common digital and analog bus. The digital bus includes all the communication, triggers and supply voltages, whereas the analog bus is reserved for signals like the control voltages for the laser frequency locks. The custom-made novel compact electronics were designed by Dr. Thijs Wendrich from the Leibniz Universität Hannover [115].[2] A picture of the stack for the rubidium laser system is shown in Fig. 4.9. All outputs on the front get connected to the laser system. Three inputs are dedicated to the stack power supply and connection to the PXI-FPGA controller. The rubidium stack has an overall length of about 30 cm and takes up a volume of about three liters. This results in a reduction in volume by about a factor of 16 compared to common lab electronics used in previous generation laser systems.

The stack is air-cooled by three fans to ensure safe operation. Although a water

[2]The electronics are developed in the framework of the LASUS project, which is funded by the German Space Agency to support the QUANTUS and MAIUS projects.

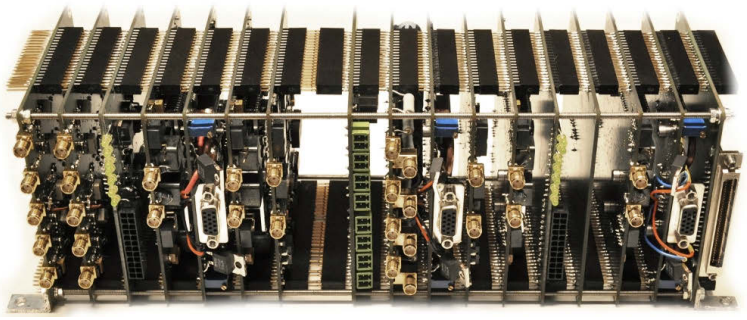

Figure 4.9: Rubidium laser system electronics stack: Each card is stacked onto each other via plug connectors that serve as the common bus for power distribution and communication. The shown stack contains all necessary cards for the rubidium laser system including current drivers, temperature controllers, shutter drivers, frequency controller for laser frequency stabilization and frequency synthesizers for the AOMs.

cooling option is provided for cards with an increased dissipation, such as the temperature controllers and the high current drivers, air-cooling has proven to be sufficient. The complete rubidium laser system dissipates an electric power of about 150 W including the electronics stack and RF amplifiers. The potassium system is envisaged to dissipate an equal amount of power.

4.4.1 Card inventory

Power interface

The main task of the power interface is to distribute the input voltages from the front receptacle to the digital bus. The input voltages comprise $+1\mathrm{S}, \pm 2\mathrm{S}, \pm 4\mathrm{S}$ and $\pm 6\mathrm{S}$ with $S = 3.2\,\mathrm{V}$ being the nominal voltage of the used rechargeable batteries. In addition to those, on-board voltage regulators generate 3 V and $\pm 15\,\mathrm{V}$ for the supply of many of the integrated circuits on the other cards. Furthermore it offers the possibility to monitor and record the input voltages as well as the electrical currents on the bus for monitoring.

FPGA input

This card has no sophisticated electronics equipped and simply distributes the digital signals between the PXI control computer FPGA card and the digital bus of the stack. The potassium laser system electronics will be most likely controlled via an Ethernet interface.

Shutter driver

The shutter driver controls the state of up to eight shutters per card. It can be programmed with a table of $2^{15} = 32\,768$ entries, each containing the state of all shutters. By applying a digital trigger on a dedicated shutter set line, the shutter increments to the next look-up table entry, while a trigger on the reset line brings the output state back to the first entry. The shutters can be driven with a selectable voltage of $\{+1, +2, +4, +6\}$S. In the used configuration, the shutters are operated with a voltage of +1S.

Temperature controller

The temperature controllers have a simple analog layout since there was no need for dynamically switching them. Only minor digital functions like resetting or bypassing an integrator as well as turning the control circuit on and off are implemented. The actual temperature measured with the attached temperature sensors as well as the temperature controller output current can be read out. The output stages for the Peltier element currents are implemented by power amplifiers commonly used for audio equipment [*TDA 2030*]. Usually inductive loads, such as loudspeakers, are hooked up and therefor care had to be taken to minimize the length of the used shielded VGA cables to prevent the output amplifier from oscillating due to the inductance of the shielded cable.

The temperature controller cards are still in operation but at one point a transition to commercial controllers [*Meerstetter TEC-1091*] is envisaged. They offer lower power dissipation by using pulse-width modulated currents for the Peltier element current. Furthermore a reduction of the card number in the stack would lower the supply voltage drop on the stack bus and the deterioration of the clock line signal, which revealed to be critical issues (discussed in greater detail in Sec. 4.5.3). The commercial temperature controllers have been tested and are ready to substitute the temperature controller cards.

DDS

Two DDS[3] cards, each with four output channels, offer the possibility to dynamically drive the four AOMs in the rubidium laser system. Each channel is running on a fixed frequency of 80 or 100 MHz with an output power of 0 dBm and can be switched on or off by hardware TTL triggers on the digital stack bus. Since the three AOMs in the distribution module need to run in states either off, at 80 or 100 MHz, a power splitter/combiner [*Mini-Circuits ZFSC-2-1-S+*] combines two DDS channels to realize the three states. The used generation of the DDS card does not yet offer the possibility

[3] direct digital synthesis

to program the amplitude, phase or frequency via a look-up table. The output power of the DDS is therefor regulated with a voltage controlled attenuator [*Mini-Circuits ZX73-2500-S+*]. The output power is then amplified with a power amplifier [*AA Opto Electronics AMPA-B-30*] to deliver around 30 dBm of RF power to the AOMs. A follow-up version of the DDS card offers the full programming of the frequency, amplitude and phase of its output. In the future, these might replace the first generation DDS in use.

Laser current drivers

The current drivers for the DFB laser diodes are based on the low-noise high-speed controller design by Libbrecht and Hall [116]. Each card can drive two laser diodes with a maximum output current of 200 mA and features hardware relays for shortening the laser diodes when not in use for protection against static discharges. A voltage controlled current control circuit behind the output stage of the driver can be used for frequency locking as well as to dynamically set the detuning of the lasers to the desired values during the experimental sequence. The current control voltage is generated by the frequency controller and is routed via the common card bus to the current driver. The control range has been configured to be about 1.6 mA for each channel. This corresponds to a frequency tuning range of 820 MHz for the master laser and 2.3 GHz for the MOPAs. For the interferometry, however, MOPA2 and MOPA3 have to be detuned by about 3−5GHz. Unlike the DDS card or the shutter driver card, the current drivers do not offer the possibility to program a state-table for dynamic switching of the output current setpoint within the experimental sequence. Therefor, an additional current reduction circuit has been soldered to the two channels of the current controller for the respective MOPAs. A digital trigger can then be used to open this current drain circuit via a MOSFET that reduces the output current by about 1.6 mA. The amount of current reduction can be controlled by means of a trim-pot on the current driver card. Sufficient detuning for interferometry is thus achievable.

Just like the current drivers for the DFB laser diodes, the high output current drivers for the amplifier section of the MOPA feature two channels with hardware relays. The two output stages can deliver in sum a current of up to 3 A. The ratio has been split for a maximum current of 500 mA for the ridge-waveguide section and 2.5 A for the tapered section.

4.4.2 Frequency controller and locking schemes

One master laser and three MOPAs have to be frequency stabilized in the rubidium system. One single card is used to stabilize the master laser in its absolute frequency by frequency modulation spectroscopy onto an atomic transition and subsequent locking of the three MOPAs in their relative frequency in reference to the master laser by

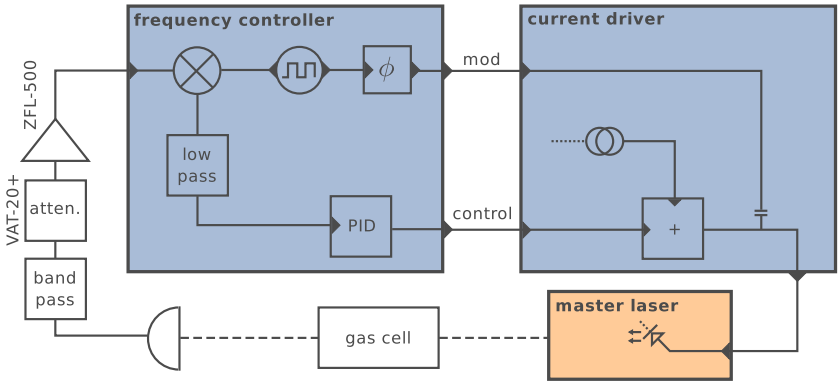

Figure 4.10: Block diagram of the digital spectroscopy lock: The modulated Doppler-free signal is detected on a photodiode and filtered by a bandpass filter. The signal is amplified by about 4 dBm and fed to the frequency controller card, where the signal is demodulated and filtered by a digital low pass. A configurable PID controller is generating the control signal, which in turn is fed to the current driver via the electronics stack bus.

using an offset locking technique. The central unit of the frequency controller is an FPGA [*Altera EP2C5T144C8N Cyclone II*] that handles all the stabilization. The modulation and demodulation for the master laser lock, the frequency counting of the MOPA-master beat notes as well as the PID controllers are implemented in the digital domain. The frequency controller FPGA is running at a clock rate of 25 MHz. It is taken directly from the 25 MHz bus clock of the stack which is derived from the 50 MHz PXI control computer FPGA clock.

Master laser spectroscopy lock

The master laser locking scheme is depicted in Fig. 4.10. For the frequency modulation spectroscopy lock, the master laser current has to be modulated. The frequency controller generates a square wave modulation signal with variable frequency and amplitude, which is coupled onto the output of the master laser current driver via a coupling capacitor. This was necessary since the designated circuit for transferring the modulation signal to the laser current driver via the analog bus was too limited regarding its bandwidth. The modulation frequency can be programmed to be $2^n \cdot 390\,\mathrm{kHz}$ with n being an integer. For the rubidium spectroscopy a modulation frequency of 6.25 MHz was found to be optimal regarding the size and slope steepness of the demodulated signal. The modulated laser is then used to generate the spectroscopy signal in a gas cell. This signal is detected with a photodiode. Its output signal is bandpass filtered by means of an L-C bandpass with a center frequency of 6.2 MHz. After optimizing the signal amplitude by means of an attenuator followed by an amplifier, the filtered signal is fed to the spectroscopy input of the frequency controller. An analog-to-digital

	external	on-board	max. input frequency
MOPA1	÷2	÷8	1.7 GHz
MOPA2	÷8	÷8	6.8 GHz
MOPA3	÷4	÷16	4.4 GHz

Table 4.2: Configuration of the external and on-board prescalers for the three MOPA offset locks and the achievable maximum offset frequency.

converter with a resolution of 12 bit and a frequency of 25 MHz is digitizing the input signal. The demodulation is done in the digital domain by multiplying the input signal with the reference modulation signal with a selectable phase shift. In this way, the derivative of the Doppler-free absorption signal is generated, which serves as the error signal for the master laser frequency lock. A PID controller generates from this error signal a control signal. It is converted by a digital-to-analog converter with a resolution of 14 bit and is fed back to the current driver via the analog bus of the electronics stack. Using this technique, the master laser is stabilized to the ^{85}Rb D_2 $|F = 3\rangle \rightarrow |F' = 3/4\rangle$ cross-over transition.

MOPA frequency offset locks

The frequency offset locks are implemented by counting the beat note frequency between the master laser and a MOPA and stabilizing it to a reference. A picture of the locking scheme is shown in Fig. 4.11. The frequency controller has three inputs for the beat signals of the MOPAs. Two programmable prescalers with division ratios ÷2 and a selectable ratio of ÷2,4,8 expand the maximum beat input frequency to about 1.1 GHz. Since for rubidium the input beat frequency can exceed values of 1.1 GHz, external programmable prescalers [*Hittite HMC862LP3E*] divide the beat frequency before inputting them into the frequency controller. The prescaler configurations for each MOPA offset lock are listed in Tab. 4.2 together with the achievable maximum offset frequency.

The gate-time is selectable and set to a value of 10 µs. The frequency controller can be programmed with a look-up table containing the desired offset lock frequencies. With a digital trigger on the set line on the bus, the frequency controller increments to the next entry in the look-up table, while a trigger on the reset line brings the controller back to the fist entry. To implement ramps with the offset frequency, the entries in the table do not only contain information about the target frequency but also if the frequency controller has to jump or ramp to the desired offset.

An overview of all the laser frequencies is given in Fig. 4.12. All the necessary detunings are set by the frequency controller card that is sending a control voltage to the respective current drivers via the common bus. MOPA2 and MOPA3 have to be detuned by a few gigahertz during the interferometry. Since this detuning

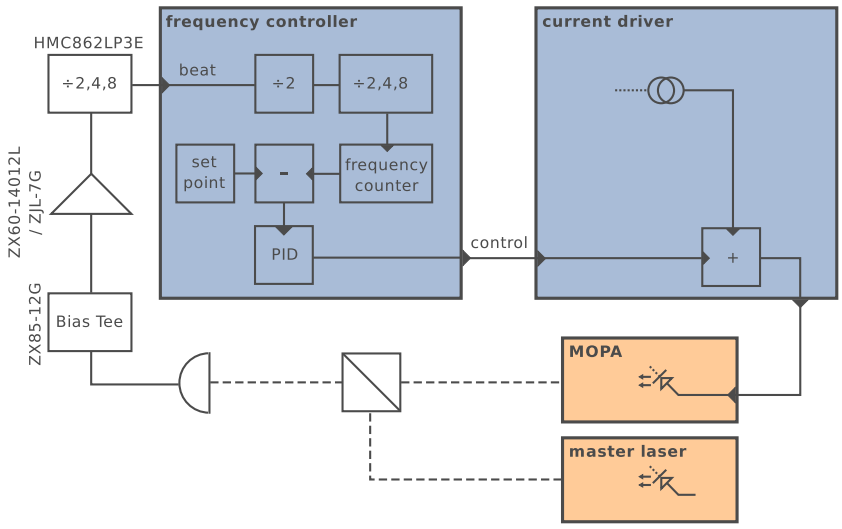

Figure 4.11: MOPA frequency offset locking scheme: The beat note between the master laser and a MOPA is detected on a photodiode, filtered, amplified and prescaled. In the frequency controller the beat frequency is counted and compared to a reference. An error signal is derived from the difference between the counted frequency and a reference. A PID controller generates a control voltage from the error signal that is fed back to the MOPA's current driver.

is outside the available tuning range of the current drivers of 2.3 GHz, the output currents are adjusted by means of the triggerable current drain circuit, mentioned before. Unfortunately, the frequency controller is not able to dynamically change from locking to falling or rising slopes of the error signal. Therefor, the sign of the beat note frequency is not allowed to invert. Due to this limitation, the two-photon blue-detuning for Bragg has to be larger than 1.5 GHz, whereas the red-detuning for Raman has to be larger than 3.6 GHz.

Features and limitations of the digital frequency controller

It is worth noting that a locking scheme based on a simple frequency counter algorithm has two limitations: (i) The bandwidth of the lock is limited by the gate-time of the frequency counter. (ii) The frequency resolution is also Fourier-limited by the gate-time $\Delta f = 1/t_{\mathrm{gate}} = 1/10\,\mu\mathrm{s} = 100\,\mathrm{kHz}$. Since in our case the frequency controller's counter detects rising and falling slopes, the frequency resolution is doubled to $\Delta f = 50\,\mathrm{kHz}$. Also it has to be mentioned that the use of prescalers decreases the resolution by the factor of which the initial frequency is divided.

Nevertheless compared to the spectroscopy lock, the offset lock is far more robust due to the fact that once the beat is in locking range, the algorithm will pull the laser towards the desired frequency as long as the control range is large enough and

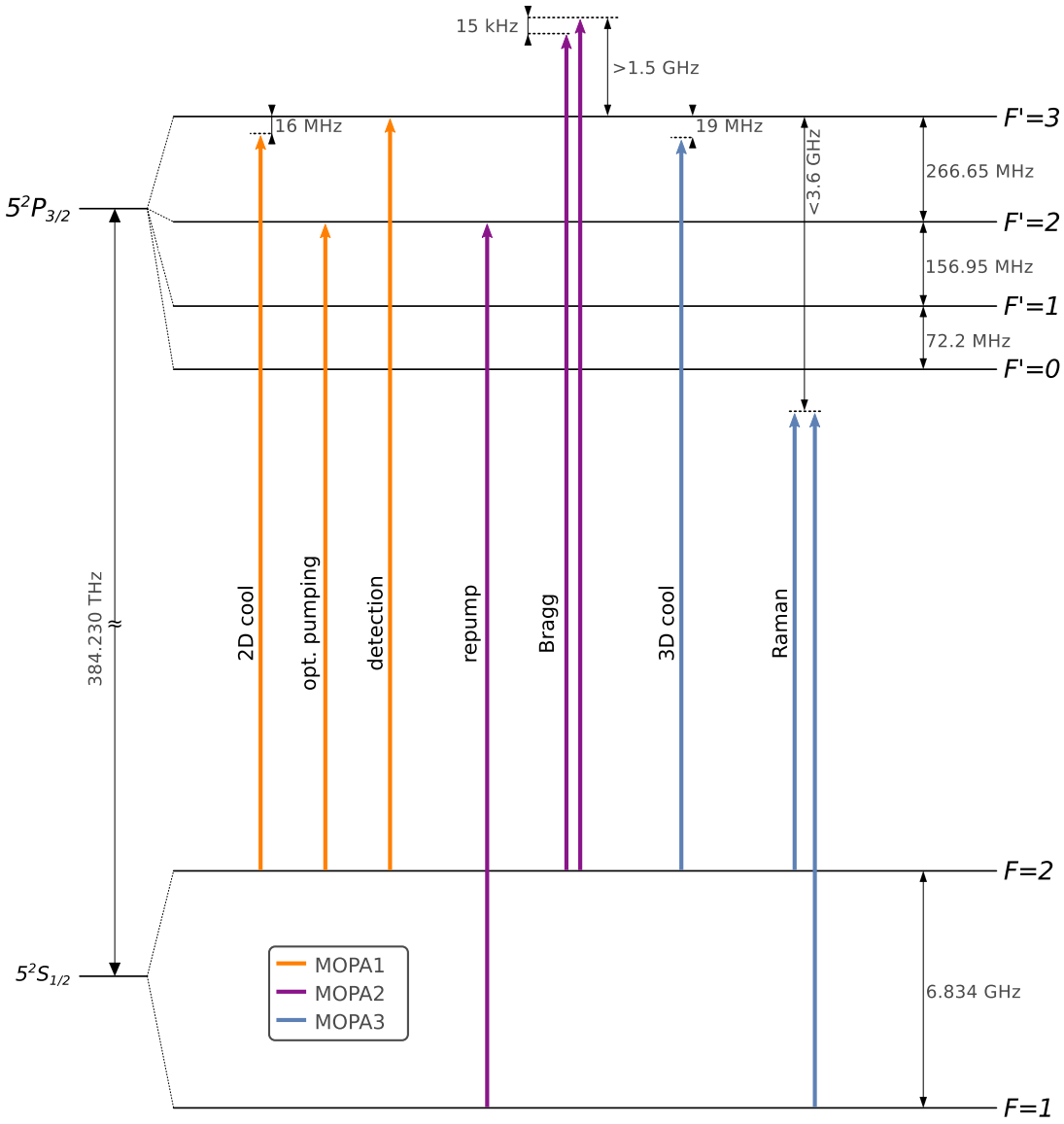

Figure 4.12: Level scheme of the ^{87}Rb D_2 line and laser frequencies including their detuning from resonance. Not shown is the master laser, which is stabilized to a rubidium-85 transition. (level scheme adapted from [117])

the power of the RF beat at the input of the frequency controller is sufficient. In the future, a software update will allow not only for locking the offset frequency to a reference but also to phase-lock the lasers.

The results of the three frequency counters as well as the generated control signals are valuable information for debugging of the experiment sequence. Therefor, the frequency controller can write all 16 channels for the frequency counter, demodulation, error and control signals into a monitoring file for later examination. Due to the limited buffer size of the frequency controller as well as the limited bandwidth on the digital bus, the frequency controller cannot write the full output of all the channels at the rate at which the frequency counters are clocking. A dedicated 16-channel mode is reducing the data load by averaging over a selectable factor of 200. The read-out gate-time is thus prolonged to 2 ms. The data is then written at this rate to a file on the PXI control computer. Anyhow, the frequency counter for each channel would suffer from a buffer overflow given this long gate-time. To solve this problem, the five least significant bytes are not transmitted. In this way it is possible to monitor all frequency controller channels with a resulting sample rate of 500 Hz and a resolution of the frequency counters that is reduced by a factor of 2.56.

4.5 Laser system qualification

Because of the application of novel key concepts, it was expected that the catapult-capable laser system would require a substantial amount of development and testing. To this end, the physics package was set up in Hannover while the laser system was assembled at the Humboldt-Universität zu Berlin. During the development of the catapult-capable laser system, a second ground laser system was used to work with the physics package in Hannover. This laser system provided all the necessary functions to characterize the physics package. However, it lacked in mechanical stability because of the employed external cavity diode lasers.

Before the integration of the catapult-capable laser system into the physics package, a series of thorough tests were made to qualify the functionality as well as the mechanical stability of the laser system and to ensure a smooth integration into the experiment, later on. The qualification included drop tests from a custom-built miniaturized drop tower at the Humboldt-Universität zu Berlin as well as the integration of the laser system in a dedicated laser system test capsule to demonstrate the operability of the laser system in subsequent drop and catapult flights at the drop tower in Bremen. In addition, the catapult-capable laser system was the first system that was supposed to make extensive use of the compact electronics. All individual cards had been electronically tested before delivery, but never as a complete stack and in conjunction with a laser system. Thus, the functionality of the electronics stack and its interplay with the laser system has been investigated within this thesis.

4.5.1 Test of individual components

Some of the custom-made key components such as the titanium mirror mounts and fiber couplers were tested and compared with commercial components in advance. The tests were conducted on a miniature drop platform at the Humboldt-Universität zu Berlin which features a drop height of about one meter and selectable peak accelerations at impact. The results showed that the mechanical stability was superior to commercial components or predecessor generations of in-house produced components [118].

An identically constructed MOPA was tested on a shaker at the Center of Applied Space Technology and Microgravity in Bremen [119]. Although the tested MOPA was not envisaged to fly on a sounding rocket, a test on a mechanical shaker can yield valuable information concerning the overall applicability of the laser module production technology. The MOPA was shaken in all three axes with an RMS acceleration between 8.1 g and 21.4 g, which represent the TEXUS sounding rocket qualification level and low earth orbit application level, respectively. The vibrations did not cause any deterioration of the output power and spectral characteristics of the MOPA [109].

Since the master laser can lock onto different Doppler-free transition slopes, it is crucial to make sure that the laser locks onto the right transition and does not jump to an undesired transition while being subjected to accelerations. To get an understanding of the locking behavior of the laser and to tune the PID controller of the master laser lock, the master laser was tested individually on the mini drop tower. A second DFB master laser, not mounted on the mini drop tower testbed, was used as a reference. The reference laser was locked to the ^{87}Rb D_2 $|F = 2\rangle \rightarrow |F' = 3\rangle$ transition and its light shifted in its frequency by an AOM by 113 MHz. The QUANTUS-2 master laser was locked onto the ^{85}Rb D_2 $|F = 3\rangle \rightarrow |F' = 3/4\rangle$ cross-over transition using the frequency controller card. Light from both lasers was overlapped on a fast photodiode. The beat note with a frequency of 953 MHz was observed on a spectrum analyzer [*Rohde&Schwarz FSL18*] as well as recorded with one of the frequency counters of the frequency controller card. Additionally, the error and control signals of the frequency controller were recorded while dropping the master laser from the mini tower. The gain of the PID controller for the master laser lock was increased to a level below the point at which the control circuit started to oscillate. This could be observed with the help of the beat note on the spectrum analyzer as well as the standard deviation of the error and control signal of the spectroscopy lock. Because the desired transition features the steepest slope in the demodulated spectroscopy signal, the noise amplitude of the error signal decreases in case the laser locks to an undesired transition. Furthermore, the control signal of the lock exhibits an abrupt jump to another value when the laser locks to a different transition.

The master laser was then dropped from the mini drop tower to check the stability of the lock. The beat note as well as the error and control signals of the frequency

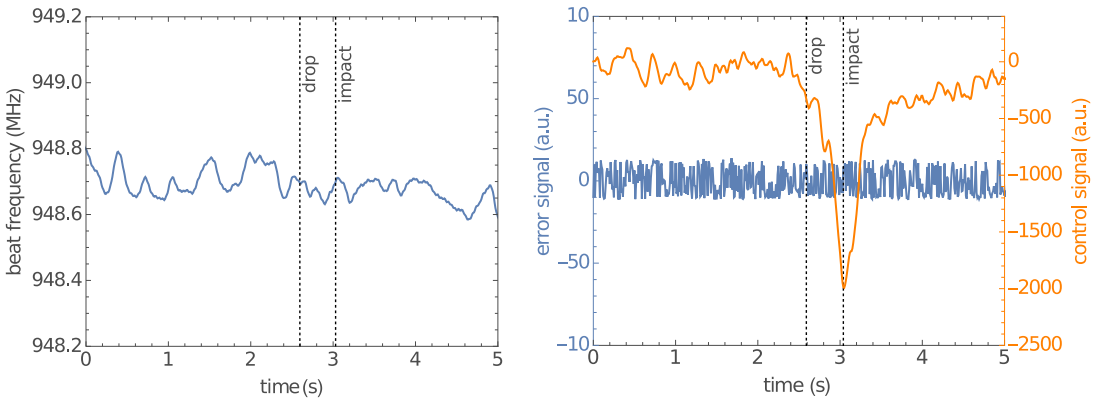

Figure 4.13: Behavior of the digital spectroscopy lock during a drop from the miniaturized drop tower: Beat frequency between master laser and reference laser (left). Error and control signal of the spectroscopy lock (right). The dashed vertical lines mark the time of release and impact.

controller are shown in Fig. 4.13. The master laser stayed locked to the right transition during release and impact. This can be deduced from the beat frequency that is constant at around 948.7 MHz with a slowly varying frequency drift between the two lasers within the range of 100 kHz. The controller is actuating on the laser current to keep the laser at its desired frequency. After impact the current returns to its initial value. Also, the mean noise level of the error signal does not change.

4.5.2 Laser system test capsule

The laser system was integrated into a dedicated catapult capsule and has been tested at the drop tower within two drops and seven catapult flights. The basic capsule structure was comparable with the QUANTUS-2 capsule structure described in Sec. 3.2. The capsule base housed rechargeable batteries with a nominal voltage of 24 V as well as the control computer of the capsule. On the level above, additional DC-DC voltage regulators were installed to provide ±15 and 5 V for conventional lab rack electronics. Also a complete set of LiFePo4 batteries was integrated on this platform for the supply of the laser system electronics stack. Furthermore, a dedicated PXI system for the control and monitoring of the laser system was installed. It housed the same controller and FPGA card like the QUANTUS-2 PXI. An additional data acquisition card [*NI PXI-6259*] served for monitoring. On the upper next level, break-out boxes and conventional rack electronics were housed. During the first tests, the digital frequency controller was not available and analog lab electronics were used to stabilize the laser frequencies. These were based on digital phase-frequency detectors [*Hittite EVAL-ADF4108EBZ1*] for offset locking, analog PID controllers as well as a frequency synthesizer and analog mixer for the frequency modulation spectroscopy of the master

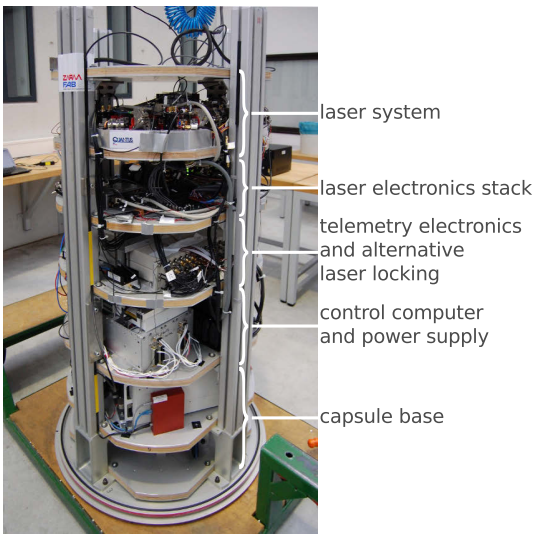

Figure 4.14: Picture of the laser system test catapult capsule: The capsule base houses batteries, a control computer and read-out electronics. Located on the level above are voltage converters as well as batteries and the control computer for the laser electronics. The two levels above house some alternative lab locking electronics and telemetry as well as the laser system electronics stack. The laser system itself sits on top of the capsule.

laser. On the next level, the electronics stack was installed, which was connected with the laser system sitting on the top level. A second backup DFB master laser was also installed next to the laser system, which had been already tested thoroughly in advance and provided a reference for the QUANTUS-2 master laser [120].

The rubidium laser system was qualified with the test capsule in a series of two drops and seven catapult launches at the drop tower and we will now discuss the results of the qualification tests.

Thermal behavior

The laser system test capsule did not feature water cooling and therefor, a temperature increase induced by the irradiated heat from electronic devices was expected. Temperatures started to rise immediately after the hull and lid had been mounted, thus closing the capsule airtight. To reduce this temperature increase, the lasers were turned off during the evacuation phase. Nevertheless, the temperature increased almost at a constant gain of about 3.5 °C per hour, starting at 22 °C while being located in the lab. Shortly before the catapult launch, the temperature inside the capsule reached values of 30 °C. The increase in temperature did not cause any problems with the electronics and lasers. However, the fiber couplings within the distribution module were affected by the temperature increase because of the thermal expansion of the laser system breadboards. While the MOPA fiber couplings did not show a reduction in power, thanks to the short distance between the lasers and the fiber couplers, the optical power in the output ports of the distribution module decreased by about 43 %. The most critical element regarding the temperature stability of the laser

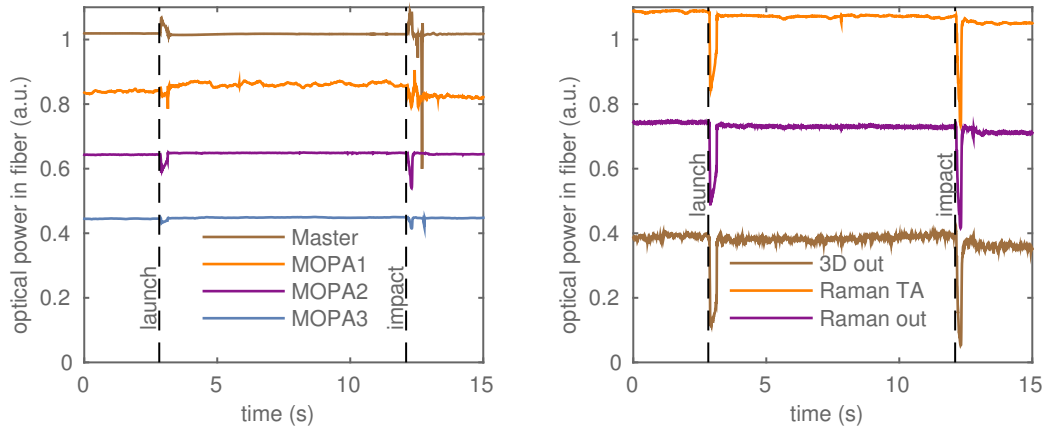

Figure 4.15: Optical power in the fibers during a catapult flight with the laser system test capsule: (left) Fiber couplings in the MOPA module show just a minor reduction at the launch and impact of up to 16 %. (right) The power in the 3D cooling fiber reduces by 80 % during the impact, whereas the power of the Raman TA and the output of the Raman module reduces by about 40 %. Most importantly, all powers return to their initial values after the deceleration, showing just a minor reduction below 10 %.

system are thus the long free beam paths inside the distribution module. Compared to the predecessor QUANTUS-1 laser system, this result presents a major improvement since a temperature increase of just few degrees Celsius renders a BEC creation with the QUANTUS-1 apparatus impossible [121]. In contrast, supplementary tests with QUANTUS-2 have shown that an overall reduction of the laser power of about 50 % does not affect the final atom number in the BEC. Since the QUANTUS-2 capsule features water cooling, which is especially attached to the distribution module breadboard, a reduction of the laser power resulting from a temperature increase is be negligible.

Optical power during catapult operation

Photodiodes [*Thorlabs FDS100*] at the end of the output fibers of the laser system as well as behind the fiber outcouplers were used to record the optical power within the laser system. The photocurrents were transformed into a voltage by a home-made transimpedance amplifier circuit. The output was recorded with the PXI data acquisition card using a sample rate of 20 kHz. The recorded data is plotted in Fig. 4.15. During the catapult launch and recapture, the optical power in the MOPA fibers and the master laser fiber reduced by not more than 16 %. The optical power behind the tapered amplifier of the Raman module and the Raman module output fiber dropped by about 40 % whereas the output of the 3D cooling fiber was reduced by 80 %. The

most important result, however, is that the optical power at every point within the laser system settles at its initial level after the catapult launch. After the impact in the deceleration container, the overall power level at the output of the laser system reduces by not more than 10 %.

Stability of the laser frequency locks

The stability of the spectroscopy lock of the master laser and the frequency offset locks of the MOPAs were investigated using conventional analog lab rack electronics as well as the digital frequency controller card. The analog control and error signals have been recorded using the PXI data acquisition card with a sampling rate of 20 kHz, while the digital lock signals were recorded with a sampling rate of 100 Hz. Initial tests using the conventional electronics showed some issues caused by mechanical instabilities of the potentiometers of the temperature controllers, which were used to dial the temperature setpoint. After fixing these, the conventional lab electronics as well as the digital frequency controller performed well, holding the offset locks during the catapult launch as well as the deceleration. As already diagnosed within the mini tower drop tests, the error and control signals of the master laser locks did not show any indications for a failing lock. As a cross-check, the older second master laser was used as a reference for the new master laser. It was locked to the ^{87}Rb $|F = 2\rangle \rightarrow |F' = 2/3\rangle$ transition using the conventional analog electronics, while the new master laser was locked to the ^{85}Rb $|F = 3\rangle \rightarrow |F' = 3/4\rangle$ transition using the digital frequency controller card. The resulting beat frequency of 1.2 GHz was recorded using one of the frequency counters of the digital frequency controller card. During the catapult launch and the impact, no evidence of a failing lock was indicated by the control and error signals of both master laser locks. Furthermore, the beat between the two master lasers did not show any deviation of the beat frequency within the frequency resolution of 51 kHz at a sampling rate of 100 Hz.

The MOPAs were locked to the master laser with a frequency offset of 300 MHz. The beat frequency was recorded using the frequency controller card with a digital resolution of 12.8 kHz. During the whole catapult sequence, only sporadic deviations of the beat frequency of ± 1 bit could be observed within a temporal resolution of 100 Hz.

The overall performance of the laser system and electronics proved to be excellent within the test campaigns and the laser system test capsule was finally transferred to Hannover for the integration of the laser system into QUANTUS-2.

4.5.3 Integration into QUANTUS-2 experiment

Before the replacement of the old QUANTUS-2 ground laser system and joining the control software of both capsules, the functionality of the catapult-capable laser system

in conjunction with the QUANTUS-2 capsule was tested. Both, the laser system test capsule and the QUANTUS-2 capsule were placed next to each other and fibers from the new laser system were connected with the QUANTUS-2 physics package (see Fig. 4.16). Each capsule had a dedicated control software for the experiment sequence running on its control computer. The trigger starting the sequence in the QUANTUS-2 capsule was routed to the test capsule for synchronization of the laser system sequence. After successful operation of the experiment with the new laser system and electronics, the laser system was integrated into the QUANTUS-2 capsule.

After the integration, the laser system electronics stack needed some further treatment and debugging. Due to an impedance mismatch and the substantial amount of capacitive integrated circuits in the stack, the clock signal generated by the FPGA in the PXI control computer suffered from deterioration and reflection at the end of the stack bus. A communication with the frequency controller and the shutter driver was thus not possible. This problem could be solved by removing unnecessary cards from the stack and placing the frequency controller and shutter driver at the end of the stack where the clock signal has a maximum amplitude.

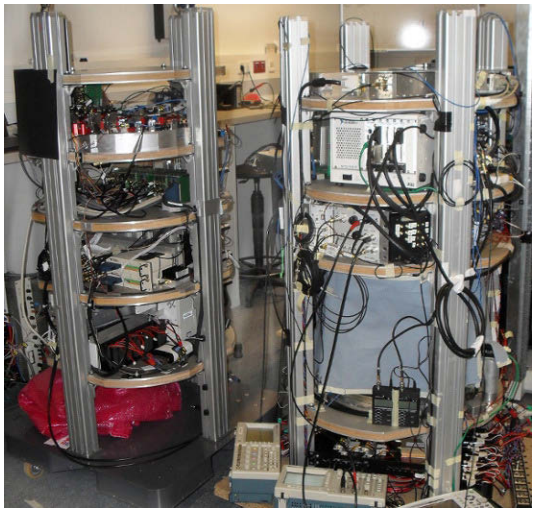

Figure 4.16: Operation of QUANTUS-2 experiment (right) with laser system in test capsule (left) in Hannover.

The temperature controllers were affected by the RF signal for the evaporation. Furthermore, the output stages of the temperature controller [*TDA2030*] are not designed for driving capacitive loads such as the D-sub cables used for the connection with the lasers. By replacing them for shorter cables and tuning a stabilizing circuit of the temperature controller, the problems with oscillating temperature controller output stages could be solved.

The common bus line is created by the cards stacked onto each other. The complete stack is thus prone to voltage drops occurring because of the increased ohmic resistance at the connectors. Care had to be taken to use power supply cables with a sufficient large cross section. Some voltage regulators on the DDS card had to be replaced by low drop out regulators to compensate for the lowered supply voltage. The connection of the power supply cables with the receptacle on the power interface was also replaced by high voltage D-sub connectors to reduce the voltage drop on the supply line.

Although the debugging of the electronics took some weeks, the gain in experience was very important for the future sounding rocket experiments MAIUS, which rely on

the compact electronics as well. The analog temperature controllers will be replaced by commercial controllers [*Meerstetter*]. Furthermore, the next generation electronics will feature a communication via an Ethernet protocol to avoid problems experienced with the FPGA-based communication.

4.6 Potassium laser system

Although the potassium laser system is most of all a mirror image of the rubidium system, there are minor differences. First of all, the used diode lasers and tapered amplifiers have been explicitly produced to run at at the potassium D_2 transition wavelength of 767 nm. The master laser is equipped with a vapor cell heating since the vapor pressure within the gas cell has to be increased by raising the temperature to about 60 °C to facilitate spectroscopy. The distribution module had to be redesigned to allow the integration of an additional tapered amplifier for the repumping light. This step was necessary due to the hyperfine levels of the excited state of the bosonic ^{41}K being separated by only few megahertz [122].[4] This leads to a high loss rate of atoms from the cooling cycle that has to be compensated for by a repumping laser with an optical power comparable to the cooling laser power [123]. On the other hand, the Raman module design becomes much more straightforward since the necessary frequency difference of 254 MHz for ^{41}K can be simply generated by using a double-pass through an acousto-optic modulator.

The technical aspects of the QUANTUS-2 apparatus and the catapult-capable laser system have been introduced in the previous two chapters. We will now focus on the performance of the experiment in microgravity.

[4] A short discussion on potential potassium isotopes is given in Sec. 7.2

5 Fast preparation of rubidium Bose-Einstein condensates in microgravity

In this chapter, we will analyze the performance of the QUANTUS-2 experiment in microgravity. Although the apparatus is designed as a dual-species experiment, it was operated exclusively with ^{87}Rb, while an upgrade with potassium is planned in the near future (see Sec. 7.2). The first drop and catapult campaigns were used to qualify the robustness of the complete system and demonstrate the performance of the compact laser system in conjunction with the fast atom-chip-based BEC source in microgravity. The experiment sequence for the rapid BEC production will be introduced, followed by an evaluation of in-trap oscillations as well as the rate of expansion of the BEC after release from the trap. The chapter finishes with a description of the transfer of the atoms into a magnetic insensitive state.

At the time of submission of this thesis, QUANTUS-2 is not only the fastest BEC experiment in the world, producing BECs within 850 ms, but also it can produce condensates within 1 s with an atom number of 1×10^5, which is larger by one order of magnitude than the second fastest experiment [124]. This chapter introduces the standard experiment sequence for a fast BEC production and will be the foundation for the next Chapter 6, in which we will show how the kinetic energy of the BEC can be reduced by means of a magnetic lens. This will allow for the lowest three-dimensional expansion rate of an atomic ensemble ever achieved.

5.1 Definition of the coordinate system

An overview of the coordinate system as well as the laser beam axes is shown in Fig. 5.1. The origin of the coordinate system is located at the center of the science chip and sits on top of its mirror coating. The z-axis is normal to the chip surface, which is mounted vertical. The y-axis is pointing downwards along the direction of gravity. The x-axis is lying on top of the science chip pointing in the horizontal and forms an orthonormal system with the y- and z-axis. Three Helmholtz coils allow for the creation of a homogeneous field along the x-, y- and z-axis, which in turn are called x- y- and z-coils. The precooled atom beam is directed in a 45° angle downwards in the x-y plane through the science chamber. One pair of counterpropagating beams along

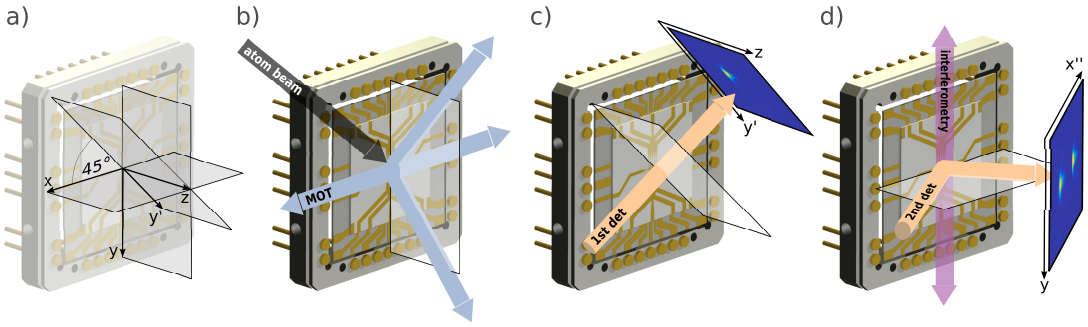

Figure 5.1: Overview of the coordinate system and the important laser beam axes: (a) The origin of the coordinate system is sitting on the surface of the atom chip, which is located in the x-y plane. The y-coordinate is pointing along the direction of gravity and the z-coordinate is normal to the chip surface. The y' axis is created by rotating the y-axis by 45° around the z-axis. (b) Location of the atom beam from the 2D$^+$MOT and the MOT beams. (c) Orientation of the first detection. (d) The second detection imaging beam is reflected over the chip in the horizontal plane. Due to the reflection, there are two shadows of the atom ensemble visible on the camera. The interferometry beam is pointing along the y-axis and is being retroreflected at the bottom.

the x-axis and one counterpropagating pair reflected over the chip in the vertical plane allow for laser cooling in all three dimensions. The first detection beam is directed in a 45° angle within the x- and y-plane pointing upward to the first detection camera. The images have coordinates y' and z whereas the y'-axis is created by rotating the y-axis by 45° around the z-axis . The second detection beam is reflected over the chip in the horizontal plane with an angle of incidence of 37.5°. Due to the reflection of the imaging beam at the chip surface, there are two shadows of the atom ensemble visible on the camera. The interferometry beam is pointing downwards along the y-axis and is retroreflected at the bottom.

5.2 Magnetic field simulation

The magnetic fields generated by the atom chip and Helmholtz coils can be simulated by a *Mathematica* script developed within the work of [78]. The simulation helped to identify trap geometries for a fast production of ultra-cold atoms. Due to the limited microgravity time and number of drops per day, there is no possibility to conduct trial and error experiments at the drop tower. Thus, the meticulous simulation of the experiment sequence becomes an absolute necessity and helps to understand the atom chip. This is especially valid for the upcoming MAIUS sounding rocket missions. These are using a comparable atom chip technology and are highly dependent from a simulation of the magnetic fields since there will be no possibility to test the experiment in microgravity beforehand. We will now shortly illustrate the concept of the magnetic

field simulation.

All current carrying structures like the Helmholtz coils, 2D$^+$MOT coils, mesoscopic chip structures as well as the chip wires including their feeds are modeled within the simulation. Static or dynamic currents can then be sent through individual structures. Using the Biot-Savart law, the complete magnetic field $\mathbf{B}(\mathbf{r})$ created by the current carrying wires can be calculated. From this, the atom-field interaction potential $V(\mathbf{r})$ can be deduced. A *Mathematica*-implemented routine for finding the minimum of a function is then searching for the trap center. At the potential minimum $\mathbf{r}_0$ the Hessian matrix $H(\mathbf{r}_0)$ is computed. By solving the eigenproblem for the Hessian matrix, it is then possible to get the orientation of the principal axes of the magnetic trap in reference to the chip coordinate system as well as the trapping frequencies ω_j along these axes (see Sec. 2.2.1). Furthermore, a polynomial function till fourth order is being fitted to the potential around its minimum to calculate the L_3 and L_4 values, characterizing the strength of the anharmonicities along the trap principal axes.

A second part of the program can calculate the center of mass motion of the condensate for the case of time-dependent currents in the structures. Just like in the experiment control sequence, the currents can be switched dynamically within the *Mathematica* simulation using different ramp forms. By solving Newton's equation of motion for all three directions, one can get the time-dependent position of the condensate. It is thus possible to make estimations of the in-trap oscillation amplitudes one can expect when changing the magnetic field dynamically.

The program can be run for adjustable values of the gravitational acceleration as well as its direction for taking into account a possible tilt of the experiment in reference to gravity. It also features the possibility to add homogeneous offset fields as well as correction factors to the programmed currents. All this allows for a gauging of the chip simulation to achieve maximum agreement between simulated and experimental results. This program will be used for the future MAIUS sounding rocket missions by adapting the layout of the current carrying structures and subsequent gauging by comparison with experimental results.

5.3 Sequence for ultra-fast BEC production

The sequence for the fast BEC production is discussed in greater detail in [80]. An overview of the sequence with absorption images and illustrations of the chip structures used throughout the sequence is shown in Fig. 5.2.

Magneto-optical trap

The 2D$^+$MOT generates a beam of precooled rubidium atoms from the background rubidium vapor pressure that is maintained by keeping the rubidium oven at a temperature of about 58 °C. Two pairs of racetrack coils create a transversal quadrupole

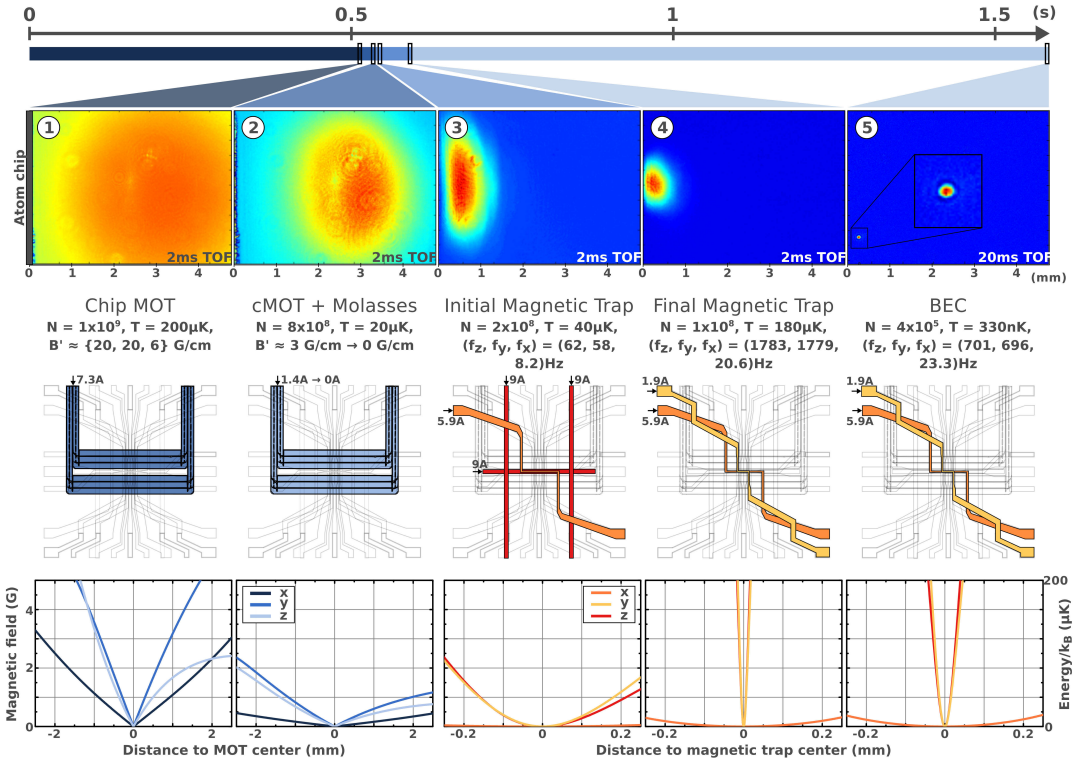

Figure 5.2: BEC production sequence: Five absorption images of the atoms illustrate the steps involved. The chip structures used as well as the magnetic field simulated with a model of the wire structures are shown below the images. The trap bottom has been subtracted for the magnetic traps. All chip configurations are used in conjunction with external bias fields. (1) After 500 ms, 1×10^9 atoms are loaded into the MOT generated by the mesoscopic U-structure in conjunction with the laser fields. (2) The atoms are compressed and cooled by an optical molasses to 20 μK. (3) 2×10^8 atoms can be captured in the initial magnetic trap, formed by the mesoscopic H and a base chip Z-structure. (4) To improve the evaporation efficiency, the trap is compressed by switching from the mesoscopic H-structure to a science chip Z-structure while keeping the base chip Z switched on. (5) During evaporation to the BEC, the trap is decompressed once to avoid three-body collisions. (picture taken from [80])

field along the desired atom beam direction. Two retroreflected transversal beams with a total power ratio of 45 % in each beam ensure cooling in the transversal direction for 2D-MOT operation. A pusher beam with 9 % of the total power out of the fiber pushes the atoms along the axial direction into the science chamber through the differential pumping stage, while a retarder beam with a power of 1 % out of the fiber is reflected at the differential pumping stage and directed in opposite direction to provide additional cooling in the longitudinal axis for $2D^+$MOT operation. The intensity of the pusher beam can be reduced by a neutral density filter installed in the collimation optic of the pusher. The power ratio between pusher and retarder allows for tuning the velocity profile of the atomic beam to match the capture velocity of the 3D-MOT. Two coils next to each other are wired in series and the current through the opposite coils can be adjusted to shift the magnetic field minimum and align the atomic beam for best insertion into the science chamber. The cooling light of the $2D^+$MOT is detuned by -16.2 MHz from the transition $|F = 2\rangle \rightarrow |F' = 3\rangle$. A laser power of 90 mW is available in the $2D^+$MOT. The atomic flux is not saturated and a higher laser power would lead to a further increase.

The magnetic fields for the 3D-MOT are generated by using the mesoscopic U-structure and the y- and z-coil [90]. The magnetic field gradients of $\{B'_x, B'_y, B'_z\} \approx \{20, 20, 6\}$G/cm together with a detuning of the cooling laser of about -19 MHz from the resonance provide a loading rate of about 1×10^9 atoms/s. The 3D-MOT saturates at an atom number of about 2.5×10^9 atoms after 4 s. The total optical power in the 3D-MOT cooling beams is about 60 mW at which the performance of the 3D-MOT reaches its optimum. The MOT loading takes 150 ms. As we will see, an increase of the MOT loading time will not lead to a higher atom number in the magnetic trap because of the inefficient transfer of the atoms into the first magnetic trap.

Compressed MOT, molasses and optical pumping

The MOT center is located at a position of about 3 mm away from the chip. The position of the first magnetic trap has its central position just 500 µm away from the chip and therefor, the atom ensemble has to be pulled towards the chip and compressed to enhance the mode matching. To this end, the magnetic field gradient is reduced to about 3 G/cm and the detuning of the cooling beams is increased to -50.6 MHz [125]. By adjusting the y-field simultaneously, the compressed MOT gets pulled towards the chip with a distance of about 1 mm. This process takes about 63 ms. In a next step, the atoms are subjected to an optical molasses for 2.5 ms by turning off the chip and compensating a residual homogeneous magnetic field to zero with the Helmholtz coils. The detuning of the cooling beams is further increased to -122 MHz. This allows for polarization gradient cooling the ensemble to a temperature of about 20 µK [126].

Since only weak-field seeking atoms can be captured in the magnetic trap, all the atoms are optically pumped into the magnetic sublevel $|F = 2, m_\mathrm{F} = +2\rangle$ within

0.73 s by shining in circular polarized light through the detection telescope onto the atoms. The detuning of the pumping light from the transition $|F = 2\rangle \rightarrow |F' = 3\rangle$ is swept from -265 to -244 MHz to transfer all the atoms to the $|m_F = +2\rangle$ state. This increases the atom number in the first magnetic trap by about a factor of three.

Magnetic trap

About 2×10^8 atoms are captured in the initial magnetic trap, which is created by using the mesoscopic H- and the base chip Z-structure. Only about 25 % of the atoms of the molasses can be transferred into the first magnetic trap because of an insufficient trap depth, trap position mismatch and inapt trapping frequencies, which are limited by the gravitational sag. After 25 ms of holding the atoms in the initial trap, the mesoscopic H-structure is ramped off while the science chip Z-structure is being ramped up within 25 ms. The trap is then compressed and pulled towards the chip by increasing the y-field. This simultaneously increases the trapping frequencies to $\{\omega_x, \omega_y, \omega_z\} = 2\pi \cdot \{20.6, 1779, 1783\}$Hz and facilitates a quick evaporation thanks to a high elastic collision rate and a resulting fast rethermalization.

Evaporative cooling

The phase space density of the ensemble is reduced below the BEC transition temperature by selectively removing the hottest atoms in the ensemble using evaporative cooling. Microwave transitions to a non-trappable internal state are selectively induced for the hottest atoms by applying a radio frequency via one of the U-structures of the base chip. On the one hand, the evaporation should be slow enough to ensure rethermalization of the ensemble. On the other hand the magnetic trap should be steep enough to keep up the elastic collision rate [43]. The density of the atomic ensemble is increasing during evaporation and three-body collisions lead to increasing trap losses. Therefor, at a certain point, the trap frequencies are lowered to values of $\{\omega_x, \omega_y, \omega_z\} = 2\pi \cdot \{23.3, 696, 701\}$Hz to decompress the trap. The evaporation sequence includes seven linear RF frequency ramps with decreasing power and frequency as well as one decompression of the trap after the fourth ramp. After a total sequence time of about 1.6 s, we end up with 4×10^5 atoms in the BEC. The lifetime of the BEC has been measured to about 2.84 s and could be probably increased by further lowering of the residual vacuum pressure in the science chamber.

Decompression of the trap

After evaporation is finished, the atoms are held in a magnetic trap with trapping frequencies of $\{\omega_x, \omega_y, \omega_z\} = 2\pi \cdot \{24.4, 456.5, 462.3\}$Hz and at a distance from the atom chip of $z = 209\,\mu$m. The high density in the final evaporation trap results in a large mean-field interaction energy, which would convert into kinetic energy after

the release of the BEC from the trap. To reduce the expansion rate of the released condensate, the trap can be decompressed by ramping down the bias field. This process has to be slow enough to be adiabatic, which means that the system stays in its instantaneous eigenstate during the change of the trapping frequencies. No higher eigenvalues of the eigenspectrum of the Hamiltonian should be excited, which would lead to a manifold of dynamics of the condensate such as dipole or density oscillations. Furthermore, because of the reduction of the bias field, the magnetic field minimum gets shifted away from the chip. In this way it is ensured that the condensate has enough room for spatial expansion after the release. Finally, it should be noted that the interferometry beam pointing vertically downward along the chip is affected by wavefront distortions because of diffraction of the beam at the chip edge. This would contribute to systematic effects to the measured phase shift in an atom interferometer [127]. This effect can be reduced by transporting the condensate away from the chip surface. The decompression and transport away from the chip is done by reducing the current in the bias field coil from $-1.5\,\mathrm{A}$ to $-0.6\,\mathrm{A}$ within $250\,\mathrm{ms}$ using a sigmoid-shaped function in time. The trapping frequencies are thus reduced to $\{\omega_x, \omega_y, \omega_z\} = 2\pi \cdot \{17.5, 61.1, 59.8\}\mathrm{Hz}$ and the condensate is transported from a position of $z = 200\,\mu\mathrm{m}$ to $z = 800\,\mu\mathrm{m}$.

Release from the trap and time of flight

After turning off the trap, the BEC undergoes an expansion that is fundamentally connected with the Heisenberg's uncertainty principle $\Delta x \Delta p \geq \hbar/2$. Thus higher trapping frequencies lead to stronger localization of the condensate and therefor a higher expansion rate after release. Additionally, the condensate expansion is strongly driven by the conversion of the mean-field interaction energy into kinetic energy after release. This effect depends on the trapping frequency as well as the atom number and is dominating for the used trap geometries in this thesis by about two orders of magnitude compared to the expansion rate connected to the uncertainty principle. Furthermore, the condensate is undergoing a residual center of mass oscillation in the final trap. It is excited by a non-perfect adiabatic decompression of the trap. This leads to a center of mass motion after the release, and is defined by the instantaneous in-trap oscillation phase at the time of switch-off. Over the time of flight (TOF) after the trap has been turned off, a homogeneous quantization field is generated by the x-coil. The initially used quantization field of $0.96\,\mathrm{G}$ has been reduced to values down to $0.19\,\mathrm{G}$ to reduce dynamics of the magnetic lensing potential, as will be described later. During the free evolution of the condensate, the atoms are being subjected to residual magnetic field gradients. Since the atoms are still in a magnetic sensitive state $|F = 2, m_\mathrm{F} = +2\rangle$, they experience a magnetic force accelerating them. To reduce this effect to first order, the atoms can be transferred into a magnetic insensitive state $|F = 2, m_\mathrm{F} = 0\rangle$ by driving an adiabatic rapid passage, discussed in Sec. 5.6.

Detection

After a variable time of free evolution, the atoms are detected by means of absorption imaging. On ground, the time of flight observable with the first and second absorption imaging detection is limited to 22 ms and 13 ms, respectively. A beam of collimated circularly polarized light in resonance with the transition $|F = 2\rangle \rightarrow |F' = 3\rangle$ is subjected to the atoms for 40 µs. The intensity profile I_a showing the cast shadow of the condensate is recorded on a camera sensor. 180 ms after the camera sensor has been read out, this so called atom image is followed by a second picture to record an image I_b of just the beam illuminating the sensor. A third dark image I_d, which was recorded with all light being blocked from entering the chamber, is used to subtract an overall electronic noise level of the camera from the atom and beam image. From the recorded densities of the corrected beam and atom image, one can calculate the projected two-dimensional atom density distribution [78, 128]:

$$n(x,y) = \frac{1}{\sigma_0}\left(1 + 4\left(\frac{\Delta}{\Gamma}\right)^2\right)\ln\frac{I_b(x,y) - I_d(x,y)}{I_a(x,y) - I_d(x,y)} + \frac{I_b(x,y) - I_a(x,y)}{\sigma_0 I_{\mathrm{sat}}} \tag{5.1}$$

Here, Γ denotes the natural linewidth of the D_2 transition, Δ the detuning from resonance, I_{sat} the saturation intensity and $\sigma_0 = (\hbar\omega\Gamma)/(2I_{\mathrm{sat}})$. From the measured density distribution, we can calculate the atom number in the thermal and condensed ensemble as well as its spatial extent and the position of the ensemble by fitting a bimodal function to represent the Gaussian and Thomas-Fermi fraction.

At the impact of the experiment in the deceleration unit, the physics package including the absorption imaging optics are getting subjected to accelerations of up to 50 g. After a dislocation of the imaging optics at impact had been observed, a position correction routine has been implemented. It is moving and rotating the CCD picture within the coordinate system to correct for these changes. Circular interference fringes created by impurities on the vacuum windows serve as a reference. In this way it is possible to extract the exact position of the atoms in respect to a defined fixed reference frame over many subsequent drops with a dislocating imaging system.

During detection, a homogeneous quantization field pointing along the direction of the circular polarized detection beam is generated by the x- and y-coil. It has a strength of 8.1 G and has been minimized to reduce switching effects of the coils as well as to reduce deviations of the calculated atom number when detecting atoms in different Zeeman levels. When shining detection light on the ensemble, the atoms in a magnetic sublevel $m_{\mathrm{F}} < +2$ are rapidly pumped into the state $|F = 2, m_{\mathrm{F}} = +2\rangle$, thanks to the short excited state lifetime of about 26 ns. Thus, the atoms become rapidly resonant with the transition $|F = 2, m_{\mathrm{F}} = +2\rangle \rightarrow |F' = 3, m_{\mathrm{F}} = +3\rangle$ driven by the detection light.

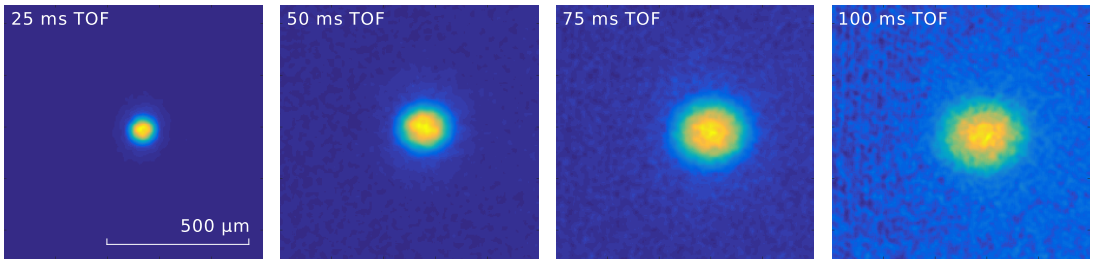

Figure 5.3: Four subsequent produced BECs during a 9 s lasting catapult flight. The TOF has been gradually increased to show the expansion of the ensemble over time.

5.4 Performance of the apparatus in microgravity

Within the first drops and catapult flights, the capabilities and robustness of the experiment have been tested. In a series of four subsequent BEC sequences during one single catapult flight, the expansion of the condensate wave function for increasing time of free evolution (TOF) has been investigated. An overview of the four produced BECs with increasing TOF is shown in Fig. 5.3. This demonstrates the robustness and capability of the high-flux BEC source in microgravity. In the following, we will discuss the performance of the experiment in microgravity in detail.

Vacuum pressure

While the experiment is located in the lab, the vacuum pressure is read-out with a UHV sensor [*Pfeiffer IKR270*], located above the science chamber outside the mu-metal. The pressure is usually at a level of 4×10^{-11} mbar. Furthermore, the ion getter pump controller unit [*Digitel SPC2-2*] offers the possibility to read out the vacuum pressure, which is calculated from the current running through the ion getter pump. It is located close to the UHV sensor. The read-out of the controller usually displays a value of 1×10^{-12} mbar, which represents the lower floor level. In drop tower operation, only the ion getter pump controller is used for monitoring the vacuum pressure. The evolution of the vacuum quality during a catapult flight or drop is depicted in Fig. 5.4. Intermittent peaks of the vacuum pressure can be observed in steady-state operation. These cannot be attributed to an actual fluctuation of the vacuum pressure since the dedicated vacuum sensor does not reproduce these peaks in lab operation and are therefor considered to be read-out errors. The only clear signature is produced at the impact of the capsule in the deceleration unit that leads to an increase of the vacuum pressure to a level of about 1×10^{-9} mbar for less than two seconds. Anyhow, this increase does not reduce the performance of the experiment. Over the course of many weeks and drops, the vacuum pressure keeps a level below 1×10^{-10} mbar. After a while, however, the vacuum pressure can increase to levels above 10^{-10} mbar. The

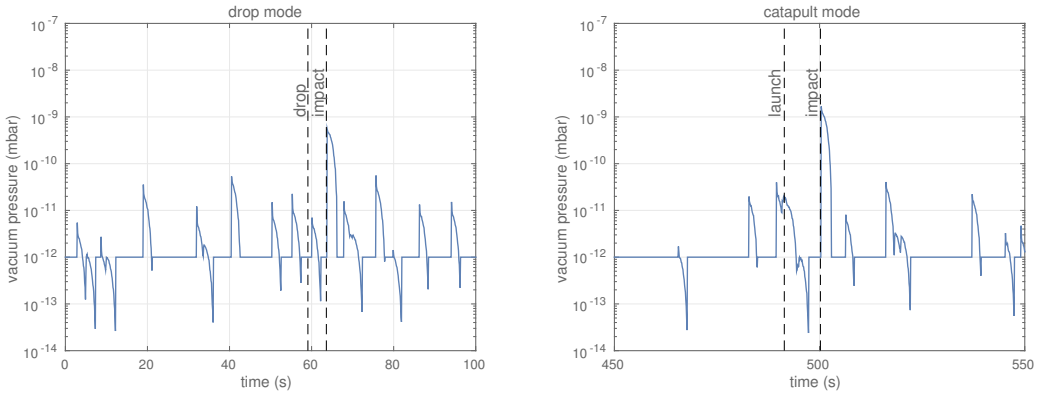

Figure 5.4: Vacuum pressure during a drop (left) and a catapult flight (right): The recorded pressure is most of the time on the 1×10^{-12} mbar floor level of the ion-getter pump read-out and shows some intermittent peaks. At impact the vacuum pressure rises shortly to 1×10^{-9} mbar and comes back to its standard level within two seconds.

installed titanium sublimation pump is used to bring back the vacuum pressure to a desired level.

Unfortunately, after some catapult launches, the performance of the experiment deteriorated. The creation of a BEC was no longer possible and some of the absorption pictures were showing shadows of macroscopic particles within the detection area during the microgravity phase. A video sequence with the detection beam illuminating the CCD of the first absorption imaging camera during a catapult flight sequence revealed a substantial amount of particles shaken up during the catapult launch. These particles can potentially fly through the cooling laser beams or might even interact with the atoms. This rendered a further use of the catapult mode impossible. The particles presumably originate from the integration of the chip into the science chamber, where pieces of the Macor™ chip mount might have been torn off. Unless otherwise noted, all of the measured data was taken using the drop mode, which is not affected by the impurities. In the future, it is intended to open and clean the vacuum chamber in conjunction with maintenance work to be done for the potassium upgrade.

Laser frequency locks

The important monitor signals of the laser locks, such as the control signals of all lasers, the MOPA offset frequencies and the spectroscopy error signal, have been recorded during a drop (see Fig. 5.5). The frequency controller is keeping the detuning of the MOPAs at the desired setpoint throughout the whole sequence in flight as well as during the impact in the deceleration unit. A slight jump in the control signal is produced by the 42.2 g deceleration in this specific drop, which is within the control

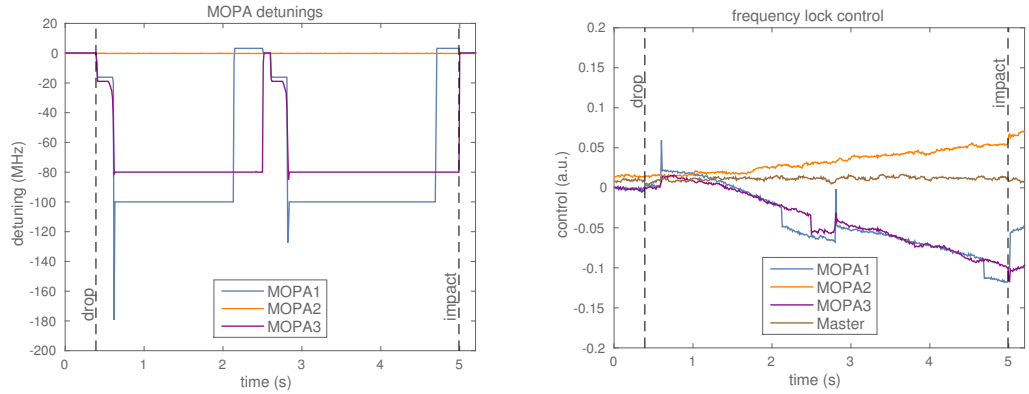

Figure 5.5: Monitor signals for the laser frequency offset locks for all three MOPAs during a drop: (left) The detuning from resonance. (right) The control signal of the frequency controller. All lasers stay in lock during the whole flight as well as after the impact and the control voltages stay within the available control range that stretches between ± 0.24 a.u. equaling 2.3 GHz. The slow drift of the control signal visible after the release of the capsule is most probably related to drifting laser temperature controllers.

range of the frequency lock of 2.3 GHz. The control signals of the MOPA offset locks start to drift slowly after the transition to microgravity. This is can be most probably related to drifting laser temperature controller electronics. Also, it is evident that the master laser stays locked to the right atomic transition since it is possible to run a BEC sequence in the deceleration container after recapture without the need to relock the lasers.

Battery power

The experiment has a battery-limited operation time of about four hours with the laser system running. This ensures enough time for experiments during a usually three hours lasting lab-to-lab drop routine. Nevertheless, the most used +2S and +6S batteries are buffered via the umbilical while the tower is being evacuated. During the capsule preparation, transfer between the lab and the tower as well as the evacuation and venting of the tower, the lasers are turned off. This allows for a prolonged uptime of the experiment and extends the battery lifetime.

Reproducibility

The system has proven to create reproducible experimental sequences throughout every drop. This ensures, for example, the phase stability of in-trap oscillations of the BEC and makes it possible to sample the dynamics of the condensate over many consecutive drops. Thanks to the position correction of the absorption imaging system,

all the taken absorption images are showing the same region within the chip coordinate system. However, the system shows a fluctuation of the atom number that can be attributed to a fluctuation of the atom number in the magnetic trap. The origin of these fluctuations has not yet been fully understood. The fluctuating atom number is non-Gaussian distributed, with the system sporadically producing ensembles with a reduced atom number by a factor of about 20 %. This makes the rescaling of the Thomas-Fermi radii of the BECs to a normalized atom number a necessity to ensure comparability within a data set.

Catapult operation

The experiment proved to be also functional in the catapult mode. This is not self-evident since the accelerations during the launch could possibly deteriorate the vacuum quality and disturb the laser frequencies or optical power, thus rendering a BEC sequence impossible. In fact, during the first catapult flights the system did show that it can be operated in the catapult mode. The most striking difference, compared to the drop mode, are the induced rotation rates of the capsule during the flight. Rotation rates of up to $0.9\,^\circ\,\mathrm{s}^{-1}$ could be observed using an inertial measurement unit. For future catapult campaigns, this data has to be monitored for every flight for post-correction of the position data of the cloud. The increased rotation rate will also contribute a phase shift that has to be considered when executing an atom interferometer sequence. In drop mode, however, the rotation rates are relaxed by about one order of magnitude because of the better controlled release of the capsule from the top of the tower. As already mentioned earlier, vacuum impurities are prohibiting the use of the catapult mode until the science chamber has been opened and cleaned.

Performance comparison with other experiments

The QUANTUS-2 apparatus presented here is outnumbering the current fastest BEC experiments concerning its cycle rate as well as the produced atom number. At its fastest rate, it is possible to create a BEC within 850 ms with an atom number of 4×10^4. When producing BECs at a 1 Hz rate, atom numbers of 1×10^5 are achievable which is one order of magnitude larger than the fastest BEC machine so far [124]. Furthermore, with a relaxed evaporation sequence, it is possible to create a BEC with a maximum atom number of about 4×10^5 within 1.6 s. This is by a factor of two faster than the fastest optical dipole trap BEC machine generating a comparable atom number. [129]. Therefor, QUANTUS-2 is keeping pace with the atomic flux rates created by the fastest lab experiments to date while being an ultra-compact and robust mobile experiment.

5.5 Dynamics of the condensate

The first drop and catapult campaigns were used to show the capability of the experiment in microgravity. In one of the first series of experiments, the in-trap oscillation of the BEC after decompression of the trap was investigated to get an understanding of the fundamental dynamics of the condensate. Furthermore, by timing the trap switch-off it is possible to control the center of mass motion of the ensemble.

5.5.1 In-trap oscillations of the condensate

After the transition to the BEC has been accomplished, the trap is decompressed a last time by reducing the bias field current from $-1.5\,\mathrm{A}$ to $-0.6\,\mathrm{A}$. The trapping frequencies are lowered from $\{\omega_x, \omega_y, \omega_z\} = 2\pi \cdot \{24.4, 456.5, 462.3\}\mathrm{Hz}$ down to $2\pi \cdot \{17.5, 61.1, 59.8\}\mathrm{Hz}$. Due to the reduction of the density of the condensate, the mean-field interaction is lowered, which leads to a lower kinetic energy and thus a reduced rate of expansion after the release from the trap. Furthermore, the minimum position of the trap is moved from $z = 200\,\mu\mathrm{m}$ to a position of about $z = 800\,\mu\mathrm{m}$. A sigmoid-shaped ramp function has been used in a first step for the reduction of the bias field in order to translate the BEC in space with a smooth start and end. Furthermore, the ramp takes 250 ms to achieve an almost adiabatic transfer. Although this seems to be a rather intuitive way to transport the condensate without exciting dynamic behavior, we will show in Sec. 6.4.2 that there are faster ways to transport the condensate from one place to another.

Since the transport is not completely adiabatic, the condensate ends up in the decompressed trap with a dipole oscillation excited mostly along the z-direction. It is beneficial to turn off the trap in the moment at which the condensate is at a turning point. In this way, the center of mass motion during the TOF can be reduced. Due to the finite resolution of the absorption imaging system, the small amplitude oscillation in the trap could not be investigated directly. To this end, the oscillation was sampled by recording a series of positions of the cloud with a varying holding time in the decompressed trap with subsequent 100 ms of TOF. The position of the cloud after the TOF T is a function of the in-trap oscillation amplitude A_z, the holding time t_{hold}, the oscillation phase ϕ_z and the trapping frequency ω_z:

$$z_{\mathrm{TOF}}(t_{\mathrm{hold}}) = z_0 + A_z \cdot \sin(\omega_z \cdot t_{\mathrm{hold}} + \varphi_z) + A_z\omega_z \cdot T \cdot \cos(\omega_z \cdot t_{\mathrm{hold}} + \varphi_z) \qquad (5.2)$$

The last term is the derivative of the first terms multiplied with the time of flight T. This function has been fitted to the recorded data (see Fig. 5.6). From the results of the fit, the in-trap oscillation has been deduced and compared with a simulation of the oscillation in the trap after 250 ms decompression. The simulation of the decompression was done using the *Mathematica* magnetic field simulation program.

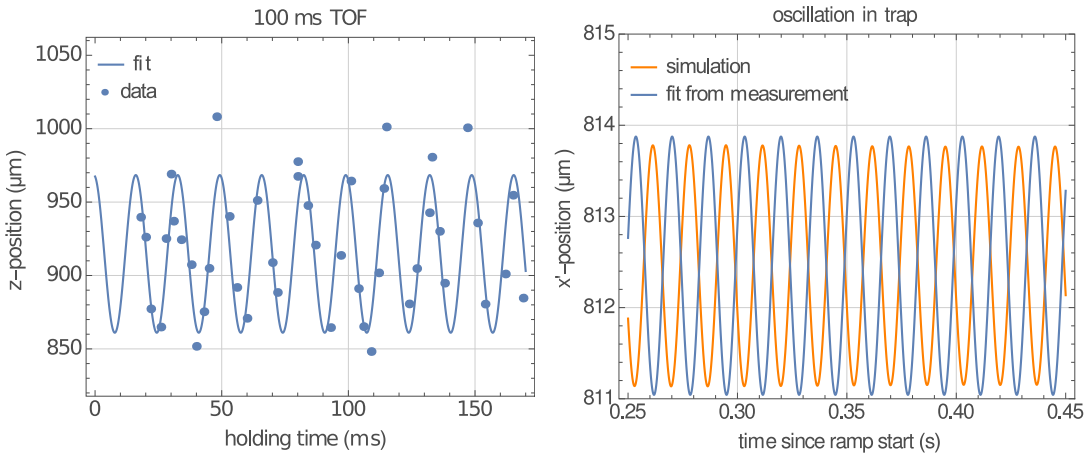

Figure 5.6: Oscillations of the BEC inside the trap: (left) Observed position after variable holding time and subsequent 100 ms TOF. (right) Comparison of simulated and measured in-trap oscillation, whereas the measured data has been corrected for a position offset. A phase offset of π between the simulation and the measured data is apparent, whereas the oscillation amplitude and frequency is well reproduced.

	simulation	measurement
z_0	812 µm	914.7(4) µm
A_z	1.3 µm	1.4(2) µm
ω_z	$2\pi \cdot 59.8$ Hz	$2\pi \cdot 60.3(3)$ Hz

Table 5.1: Comparison of measured and simulated in-trap oscillation: The frequency and amplitude agree well. The offset between the oscillation center position points to possible residual magnetic field gradients during the TOF and/or a kick on the atoms induced by the switch-off of the trap.

The position of the atoms in the trap has been measured to $z = 844(20)$ µm (simulated: $z = 812$ µm). The center of the oscillation after 100 ms of TOF lies around $z = 914.7(4)$ µm. A kick induced by dynamics during the switch-off of the chips and y-coil as well as residual magnetic field gradients can lead to this discrepancy (see. Sec. 6.4.8). When removing the position difference between the measured oscillation after TOF and the simulation, one can observe that both fit well regarding the oscillation amplitude and frequency (see Tab. 5.1). Anyhow, the measured data is shifted by an offset of about π. Although there is a shift in the phase of the measured oscillation, the simulation yields proper results concerning the amplitude and frequency of the oscillation. The overall phase stability of the experimental sequence is demonstrated by the fact that sampling an oscillation over 22 consecutive drops over several days is possible.

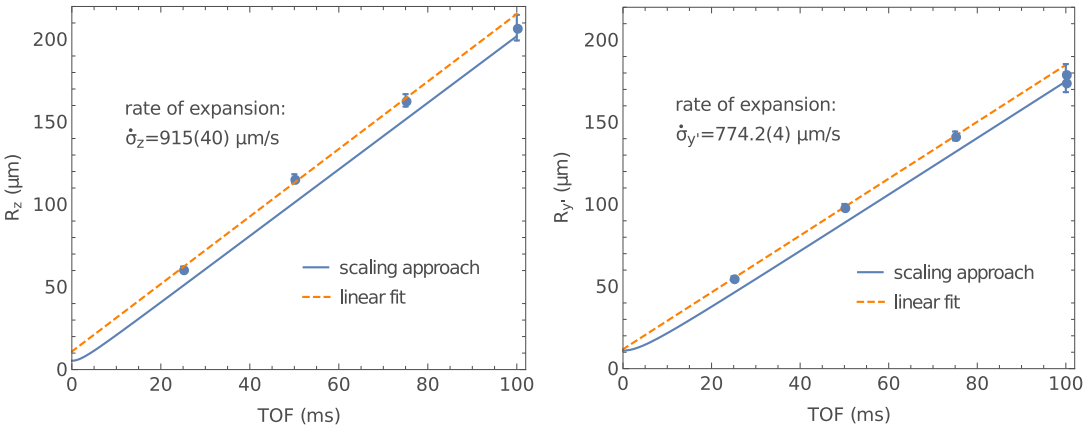

Figure 5.7: Evolution of the Thomas-Fermi radius of the ensemble after the release in z- (left) and y'-direction (right). The expansion rate of the ensemble has been inferred from a linear fit (orange). A theoretical prediction of the expansion coming from a scaling approach is shown in blue. The listed value for the rate of expansion $\dot{\sigma}$ from the linear fit is given in terms of the standard deviation of the Thomas-Fermi distribution σ.

5.5.2 Release and expansion rate

We now want to calculate the rate of expansion of the BEC after release from the magnetic trap. A TOF series ranging from 25 ms up to 100 ms is provided by the data from the catapult flight with four consecutively produced BECs. The evolution of the Thomas-Fermi radii R in the z- and y'-direction is shown in Fig. 5.7. The observed cloud radius in the y'-direction is a projection of the radii in x- and y-direction with $\alpha = 45°$ being the angle of the detection beam which is propagating diagonally in the x-y plane:

$$R_{y'} = \sqrt{(R_x \sin(\alpha))^2 + (R_y \cos(\alpha))^2} \tag{5.3}$$

The release trap is rotated around the z-axis by an angle of 11.8°. The projection angle thus becomes virtually reduced to $\alpha = 33.2°$. Since the Thomas-Fermi radius is a function of the atom number, the measured radii have been rescaled to an atom number of 50 000 using Eqn. (2.22) to compensate for shot-to-shot atom number fluctuations. The theoretical prediction of the expansion has been calculated from a scaling approach (see Sec. 2.1.4).

The expansion rates in the two observed directions agree with the scaling approach, while there exists a general size offset. An error in the calculated atom number would not lead to an offset in the size but rather change the rate of expansion. Furthermore, an error in the atom number would lead to a change of the Thomas-Fermi radius that scales $\propto (1/N)^{1/5}$ and thus would lead only to small deviations. A misestimation of the magnification factor of the imaging system would also not lead to an offset. On

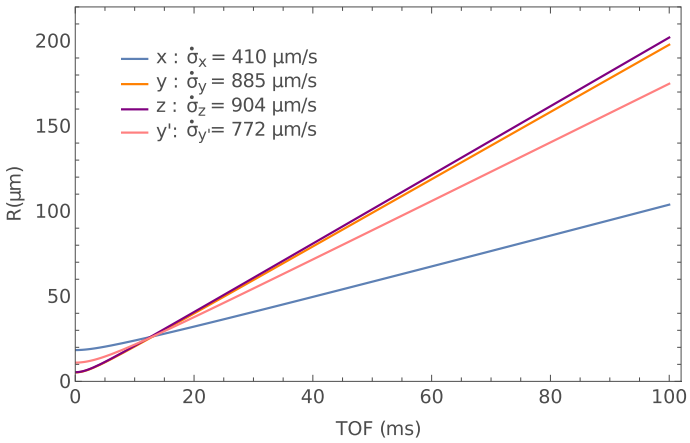

Figure 5.8: Theoretical prediction of the expansion of the BEC in terms of the standard deviation σ of the Thomas-Fermi distribution. The cigar-shaped trap with two fast radial trapping frequencies in y-and z-direction and one slow frequency in x-direction leads to an aspect ratio change from a prolate to an oblate shape of the condensate at $t = 12\,\mathrm{ms}$, which is typical for a BEC.

the other hand, an increase of the size of the condensate caused by the interaction of the condensate with the residual thermal fraction is plausible.

The TOF of the recorded data is large enough so that we can assume that the expansion of the condensate is in the linear regime. We can thus calculate the expansion rate by applying a linear fit to the measured data, whereas the data points at $t = 100\,\mathrm{ms}$ have been dropped because of the increased dilution of the cloud which leads to a underestimation of the atom number and radii. Expansion rates of $\dot{\sigma}_z = 915(40)\,\mu\mathrm{m\,s^{-1}}$ along the z-direction and $\dot{\sigma}_{y'} = 774.2(4)\,\mu\mathrm{m\,s^{-1}}$ along the y'-direction have been inferred from a linear fit. They are given in terms of the standard deviation σ of the Thomas-Fermi distribution (see Sec. 2.2.2). Since the scaling approach is in good agreement with the measured data for the expansion rate, we can use it to calculate the respective rate of expansion along the x-, and y- direction. The results are shown in Fig. 5.8. Based on the good agreement between the measured and simulated expansion, we attribute expansion rates of $\{\dot{\sigma}_x, \dot{\sigma}_y, \dot{\sigma}_z\} = \{410, 885, 904\}\mu\mathrm{m\,s^{-1}}$ to the BEC after the release from the trap.

5.6 Adiabatic rapid passage

During the magnetic trap and evaporation, the atoms are in the low-field seeking state $|F = 2, m_\mathrm{F} = +2\rangle$. The ensemble is thus sensitive to residual magnetic field gradients after the trap has been turned off. These can lead to an additional contribution to the center of mass motion as well as a modified BEC expansion [75]. It is therefor desired to transfer the atoms into a magnetic insensitive state $|F = 2, m_\mathrm{F} = 0\rangle$. A reliable technique to transfer all the atoms into a to first order magnetic insensitive state, is the adiabatic rapid passage (ARP) [130]. By subjecting the atoms to a quantization field in x-direction of about 10 G and applying a radio frequency sweep across the resonance coupling the sublevels, the atoms can be selectively transferred into a

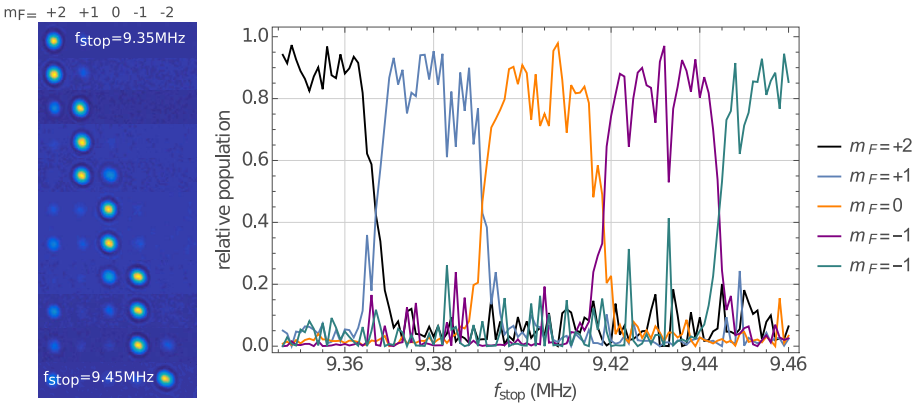

Figure 5.9: Sequence of absorption images taken after an adiabatic rapid passage (ARP) with increasing stop frequency (left). After the ARP, the atoms in different magnetic sublevels are spatially separated by a Stern-Gerlach field pulse. The atoms can be transferred selectively into a desired m_F level with an efficiency of about 90 % (right).

desired Zeeman sublevel by tuning the stop frequency f_{stop} of the sweep. In Fig. 5.9, the selective transfer of the atoms into different Zeeman sublevels depending on the stop frequency of the sweep is shown. A transfer efficiency of about 90 % could be reached. An in-depth discussion of the ARP used in this experiment can be found in [82].

In this chapter, the performance of the experiment in microgravity was demonstrated and an insight on the standard BEC creation routine in microgravity was given. The chip simulation as well as the scaling approach were used to describe the dynamics of the center of mass of the condensate as well as the expansion rate of the cloud. In the following chapter, we will show how the expansion rate of the condensate can be reduced by applying a magnetic lens. This will be crucial for future atom interferometry experiments on ultra-long time scales.

6 Magnetic lensing of the condensate

In the present chapter, we will deal with the reduction of the expansion rate of the condensate. After a short motivation, in which we discuss why a low momentum width is beneficial, we will discuss the concept of delta-kick cooling and how it can be used to form a magnetic lens for collimating the expansion of an atomic ensemble. Using a description in phase space, the principle of delta-kick cooling is illustrated. Looking at first magnetic lens results, we will identify important details that have to be taken care of when trying to increase the collimation quality of the lens. We will then introduce an improved lensing scheme and analyze its effect on the atoms in detail. This will allow for a reduction of the expansion rate of the released ensemble calculated in the previous chapter by one order of magnitude. This corresponds to an effective temperature below 120 pK, which has not been reached before in three dimensions.

6.1 Motivation for the reduction of the kinetic energy

In Sec. 5.5.2, it has been shown that the kinetic energy of the Bose-Einstein condensate after being released from the decompressed science chip base chip (SCBC) trap leads to expansion rates of $\{\dot{\sigma}_x, \dot{\sigma}_y, \dot{\sigma}_z\} = \{410, 885, 904\}\mu\mathrm{m\,s}^{-1}$ in each direction. Within the present chapter, we will show how the kinetic energy can be further reduced in a very fast and efficient way by applying a magnetic lens. The magnetic lens relies on the concept of delta-kick cooling, already introduced theoretically in Sec. 2.2.2. A descriptive explanation of the principle will be given in the following section.

From many points of view, the reduction of the expansion rate of the atomic ensemble is of fundamental interest for high-precision atom interferometry. The beam splitters and mirrors are realized by two counter-propagating laser beams driving a two-photon Raman transition between two hyperfine ground states $|1\rangle$ and $|2\rangle$ via an intermediate excited level $|i\rangle$. While subjected to the interferometry beams, the transition probability of both hyperfine ground states is oscillating with the effective Rabi frequency $\Omega_{\mathrm{eff}} = -\Omega_{1\mathrm{i}}\Omega_{\mathrm{i}2}/2\Delta$, where Δ is the single-photon detuning from the intermediate level $|i\rangle$ [131]. The single-photon Rabi frequency for the transition $m \to n$ is given by $\Omega_{\mathrm{mn}} = \mathbf{d}_{\mathrm{mn}}\mathbf{E}/\hbar$, with the transition dipole moment $\mathbf{d}_{\mathrm{mn}}$. The beam splitter pulses are realized by choosing the pulse area $\Omega_{\mathrm{eff}}\tau = \pi$ for a mirror pulse or $\Omega_{\mathrm{eff}}\tau = \pi/2$ for a beam splitter pulse. Usually, this is done by tuning the pulse length τ. Till now we have assumed, that the intensity of the driving laser field

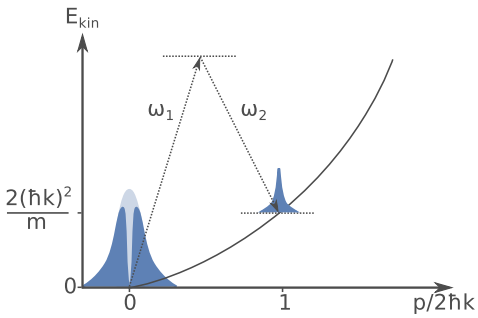

Figure 6.1: Two-photon Bragg transition and momentum selectivity: Due to the finite momentum width of the input state, the Bragg condition is fulfilled only for a certain velocity class. Transfer efficiencies can be thus increased by narrowing the momentum width of the input state. This becomes especially important for high-order Bragg transitions.

is homogeneous. In a typical experiment, however, we have to deal with Gaussian intensity profiles. The effective Rabi frequency is thus becoming position dependent. As a consequence, only a certain fraction of the atoms undergoes a Rabi oscillation with the desired pulse area depending on the spatial extent of the atomic sample. This in turn reduces the interferometer contrast due to inefficient beam splitter and mirror pulses. This effect can be diminished by reducing the size and expansion rate of the atomic ensemble.

Furthermore, because of the finite momentum width of the atomic ensemble, the resonance condition for the two-photon transition is only valid for a fraction of the ensemble. With increasing expansion rate and spatial extent, the beam splitter efficiency is thus dropping (see Fig. 6.1). This is especially true for high-order multiphoton Bragg transitions. When increasing the interferometer pulse separation times T_{sep}, this effect is becoming even more pronounced. A common way to increase the beam splitter efficiency is the application of a velocity-selective Raman transition before the first beam splitter pulse [132]. Unfortunately, this process suffers inherently from atom loss and is therefor not suitable.

Another effect reducing the contrast in the interferometer is caused by wavefront aberrations. In a retroreflection interferometry setup the wavefront of the reflected interferometry beam is distorted by the retroreflection mirror, quarter-wave plate and bottom window. For a parabolic wavefront with curvature R, the phase shift contribution arising from wavefront distortions $\Delta\Phi_{\mathrm{wf}}$ depends linearly from the effective temperature T of the ensemble and quadratically from the interferometry pulse separation time T_{sep} [133]

$$\Delta\Phi_{\mathrm{wf}} = \frac{k_{\mathrm{eff}}}{R}\frac{k_B T}{m}{T_{\mathrm{sep}}}^2. \tag{6.1}$$

When using absorption imaging for the detection of the atomic ensemble, the signal to noise ratio is dropping for longer times of free evolution as a consequence of the sample becoming increasingly dilute. Fitting the density profile of the absorption image is thus leading to an underestimation of the atom number because of the reduced signal to noise ratio. Likewise, when using an asymmetric Bragg Mach-Zehnder

interferometer, the contrast of spatial interference fringes is also dropping [76]. For fluorescence detection, anyhow, the atom number is independent to first order from the size of the ensemble, given the ensemble is covered properly by the detection beam.

All these effects are reducing the contrast or introduce systematic contributions to the phase shift and can be overcome by lowering the size and expansion rate of the atomic ensemble. Thus, a BEC is an excellent choice for high precision atom interferometry in microgravity with pulse separation times of multiple seconds. In the following we will introduce the experimental aspects of the delta-kick cooling technique, and how to use it for magnetic lensing and collimating the atomic ensemble in an extremely fast and atom number conserving way.

6.2 Delta-kick cooling approach using magnetic potentials

6.2.1 Introduction

The idea of delta-kick cooling was first described by Chu et al. in 1986 [61]. Around this time it was introduced as a cooling technique using an optical dipole trap. Nevertheless, it can be extended to any trapping potential, no matter if it is a simple dipole trap, optical lattice or for example a magnetic trap. This technique is relying on using the same infrastructure that is already used for trapping the atoms. It not only can be applied to atoms, but has been already used for example with ions and molecular beams [134, 135]. The first application using a Ioffe-Pritchard type magnetic trap was described by Aoki et al. in 2004 [136]. The first delta-kick cooling using an atom chip was shown in the predecessor generation experiment QUANTUS-1 [76]. Coldest effective temperatures down to 50 pK in two dimensions were achieved so far by optically delta-kick cooling atoms in a 10 m-fountain setup using the dipole force generated by the transversal beam profile of a single red-detuned laser beam [137]. Especially future space missions, like the Cold Atom Laboratory CAL [70] or the proposed QTEST [56] and STE-QUEST mission [57] rely on delta-kick cooling techniques for increasing the sensitivity of interferometric measurements.

The benefits of delta-kick cooling are becoming apparent when looking at alternative techniques of reducing the kinetic energy of an atomic ensemble. A standard approach is the adiabatic decompression of the trap. Although in general, no atoms are lost during this process, it can take up to several seconds to ensure that the process is truly adiabatic. This is especially valid when decompressing to trap frequencies of few Hertz. Temperatures down to 450 pK have been reached by decompressing a gravito-magnetic trap down to a mean trap frequency of one Hertz and reducing the particle number down to 2500 atoms [60]. Adiabatic decompression is limited by the gravitational sag, which deforms the trapping potential and limits the depth of the trap. This could be theoretically overcome in a microgravity environment, if it were not for the limited lifetime of the condensate. Interactions with background gas

atoms and the surrounding as well as electrical noise in the magnetic field generating structures lead to decoherence and atom loss from the trap.

Another widely used technique to cool atoms is the evaporation of the hottest atoms from a trap, as described in Sec. 5.3. Evaporative cooling suffers from atom loss by definition. Furthermore, the speed of evaporative cooling is connected to the elastic two-body collision rate, which scales with the trapping frequency. Hence, large trapping frequencies are advantageous. At certain points, however, the trapping frequency has to be lowered to reduce three-body collisions, which are leading to unwanted heating and atom loss. Thus, evaporative cooling cannot be driven arbitrarily fast.

Summarized, the adiabatic decompression and evaporative cooling suffer from low cooling rates and atom loss, respectively. Delta-kick cooling, in contrast, is an extremely fast and atom number conserving process. It is important to note, however, that a reduction of the phase space density of an atomic ensemble is not possible using conservative potentials, as shown in [93]. Delta-kick cooling has to be therefor seen as a phase space conserving process that is trading off momentum width at the expense of spatial extent. Hence, it is impossible to reach degeneracy and create a Bose-Einstein condensate solely with delta-kick cooling techniques.

6.2.2 A description in phase space

To get a descriptive picture of the lensing sequence, we now have a look at the process in phase space, which is spanned by position and momentum vectors $\mathbf{r}$ and $\mathbf{p}$. We can then express the density matrix of our quantum mechanical system in terms of a Wigner function as a quasiprobability distribution in phase space [138]

$$W(\mathbf{r},\mathbf{p},t) = \frac{1}{(2\pi\hbar)^3}\int_{-\infty}^{+\infty} d^3\xi e^{-i\mathbf{p}\xi/\hbar}\langle \mathbf{r}+\frac{1}{2}|\hat{\rho}(t)|\mathbf{r}-\frac{1}{2}\xi\rangle. \tag{6.2}$$

Given an initial density distribution trapped within a harmonic potential $V(\mathbf{r})$ for times $t \leq 0$, we set $W_0 = W(\mathbf{r},\mathbf{p},t=0)$. When switching off the trap at $t=0$ the free evolution of the density can be written as

$$W_f(\mathbf{r},\mathbf{p},t) = W_0\left(\mathbf{r}-\frac{\mathbf{p}}{m}t,\mathbf{p},0\right). \tag{6.3}$$

The distribution is thus getting sheared along the position direction. After a time of free evolution t_0, called "preTOF", the initial trapping potential is turned on for a short time t_k. For short kicking times t_k we can write the lensing process as a shearing along the momentum direction

$$W_l(\mathbf{r},\mathbf{p},t_0,t_k) = W_f(\mathbf{r},\mathbf{p}+\nabla V(\mathbf{r})t_k,t_0). \tag{6.4}$$

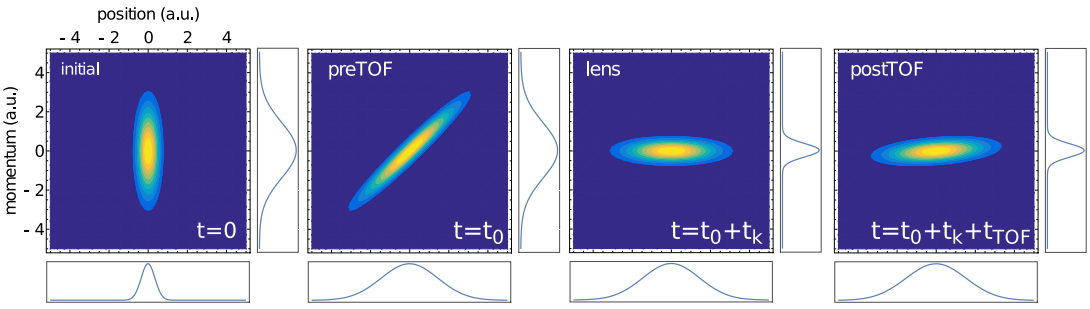

Figure 6.2: Delta-kick cooling in phase space: The initial Gaussian phase space distribution trapped in a harmonic potential is getting sheared over time t_0 after the release. When switching on the initial trapping potential for a short time t_k, the phase space distribution can be rotated around its center. By timing the pulse length t_k properly, one can rotate the distribution in the horizontal, thus minimizing the kinetic energy by narrowing the momentum distribution.

In Fig. 6.2 the process of delta-kick cooling is depicted in a two-dimensional phase space for one dimension. Lets assume a Bose-Einstein condensate being held within a magnetic trap with all atoms accommodating the ground state of the quadratic potential. When neglecting interactions between the atoms, the spatial density of the ensemble is simply given by a Gaussian. The momentum distribution is given by the Fourier transform, which in turn is a Gaussian. The resulting phase space density distribution is shown in the first picture. When turning off the trap at $t = 0$, the atoms move freely with their attributed momentum. According to Eqn. (6.3), this leads to a shearing of the phase space distribution within the time of the preTOF t_0, which is depicted in the second picture. After time t_0, the initial trapping potential is being pulsed on for a short time t_k. As stated in Eqn. (6.4), this leads to a position dependent change of momentum, which for short pulse times acts as a shearing in the momentum direction of the distribution. By selecting the right pulse time, we can now shear the distribution into the horizontal, thus reducing the momentum distribution to a minimum. After the lensing, the ensemble is again evolving freely and the ensemble is shearing again over the time t_{TOF}. But due do the narrow momentum distribution, the expansion rate is much slower. Therefor, it becomes clear that delta-kick cooling is trading off momentum width for spatial width.

6.2.3 Magnetic lens in microgravity and its limits

If we expand the delta-kick cooling technique beyond one spatial dimension, similarities to the collimation of an optical beam by means of a lens are becoming apparent. Terms like beam quality, astigmatism, coma and aberration find their equivalent in the field of cold atoms interacting with trapping potentials. In general, one can speak of the collimation of an atomic ensemble after release from a trap by means of a magnetic

lens. Just like in optics, the fidelity of the input beam as well as the properties of the lens govern the achievable collimation quality, which in atom optics would correlate with the achievable minimum expansion rate of the atomic ensemble.

If we apply the concept of a one-dimensional effective temperature to describe the expansion rate of the ensemble (see Eqn. (2.64)), the achievable temperature T_f is depending on the ratio of the initial and final width σ_0/σ_f of the atomic ensemble, given an initial temperature T_0 [139, 136]:

$$T_f = (\sigma_0/\sigma_f)^2 T_0. \tag{6.5}$$

It is thus desired to start with a cold as possible initial ensemble. Furthermore we would like to maximize the size difference between the initial and final ensemble by stretching the time t_0 between the release and lens as long as possible.

A limit for the maximum time t_0 is set by the anharmonicities of the lensing potential. The lensing potential can be approximated as a harmonic potential only within a finite region. For increasing times t_0 between release and magnetic lens, the atoms will experience a stronger deviation from the harmonic curvature of the potential. This will lead to an under- or overcompensation of the kinetic energy, thus leading to a deviation from perfect collimation. It is therefor indicated to keep the time t_0 between release and lens in an acceptable range in which the anharmonicities are not deteriorating the collimation quality.

A last but nevertheless very important limit is set by gravity. Once the ensemble is released from the trap, it will accelerate downwards. Since the magnetic trap is fixed in its position in reference to the apparatus, it is usually not possible to translate the trap along the trajectory of the falling atoms while keeping its trap frequencies and orientation constant. In contrast, microgravity setups offer the possibility to reach far lower temperatures than in a lab-based experiments because of the atoms not moving away from the trap during the time of flight. Thus, an optimized synchronous lensing in all three dimensions is achievable.

Measuring the expansion rate of an atomic ensemble is becoming increasingly different for ever lower temperatures since in a typical lab experiment the time of free evolution is limited to some tens of milliseconds before the atomic ensemble is falling out of the camera view. A fit of the increasing cloud diameter in the far field is thus not possible. Using a fountain setup or a long vertical baseline, it is possible to stretch this time. Anyhow, even for a 10 m fountain setup, like reported in [137], a measurement technique deriving the temperature indirectly from the minimum spot size of a refocused ensemble had to be applied. In this thesis, a direct observation of the expansion rate over 2 s was possible due to the experiment falling along with the atomic ensemble.

Since the expanding atomic cloud is not in thermodynamic equilibrium, it is not possible to attribute a proper temperature as defined in thermodynamics to the en-

semble. Hence, we will avoid a further use of the term delta-kick cooling since it implies a reduction of the temperature. In fact, we will use the term "magnetic lens" with which we reduce the expansion rate of the atomic ensemble.

6.3 First lens using base and science chip

Two different lensing schemes have been investigated within this work – the "SCBC lens" and the pure "BC lens". The first attempts with the SCBC lens have been done releasing the atoms from a trap at a distance of about $z = 850\,\mu\text{m}$ away from the chip, and using a Gaussian pulse of the Helmholtz y-coil as well as the science and base chip. This first lens configuration was chosen since it utilizes the standard release trap, which had been already analyzed thoroughly. First results will be presented in this section. We will see that many notable effects occur when using this first attempt lens. In the following section we will analyze, from where these peculiarities are arising, and work out an improved lensing scheme that is reducing these effects.

The starting point for the SCBC lens sequence is the decompressed release trap discussed in Sec. 5.5 at a distance of $z = 844\,\mu\text{m}$ away from the chip surface. By turning of all chips and coils, except for the quantization field coil left at a current of 0.5 A equaling a field of 0.96 G, the BEC is released from the trap and undergoes free expansion for a preTOF of $t_0 = 30\,\text{ms}$. The lensing potential is then created by pulsing the release trap potential created by the SC, BC and y-coil with a Gaussian function in time for the field creating currents. The Gaussian pulse was first used with the idea in mind that the magnetic field generated by the inductive coils can be better controlled as when switching them with a box pulse. A pulse length of 6 ms was chosen to be the fastest speed at which the measured current in the y-coil is a good reproduction of the control signal of its current driver. Since such a long lens pulse would have been too strong, leading to a refocusing of the ensemble, the BC-, SC- and y-coil current have been scaled down by a factor of 0.244 to reduce the lens strength, thus arriving at maximum currents during the lens of BC=1.464 A, SC=0.488 A and y-coil=−0.1353 A.

After the lensing, the atoms are transferred into the non-magnetic state $|F = 2, m_F = 0\rangle$ by an adiabatic rapid passage. Residual atoms in the other magnetic sub-states are pushed away by applying a Stern-Gerlach field created by a current of 1 A for 3 ms through the base chip. Throughout the preTOF, lens and subsequent TOF after the lensing, a quantization field was provided by a current of 0.5 A in the z-coil. A TOF series of the SCBC lens is shown in Fig. 6.3. From looking at these pictures a list of problems and peculiarities can be identified:

- **Pronounced tail:** A tail pointing away from the chip surface along the z-direction is visible on the first detection camera. This tail is transforming the cloud shape and diminishes the collimation quality.

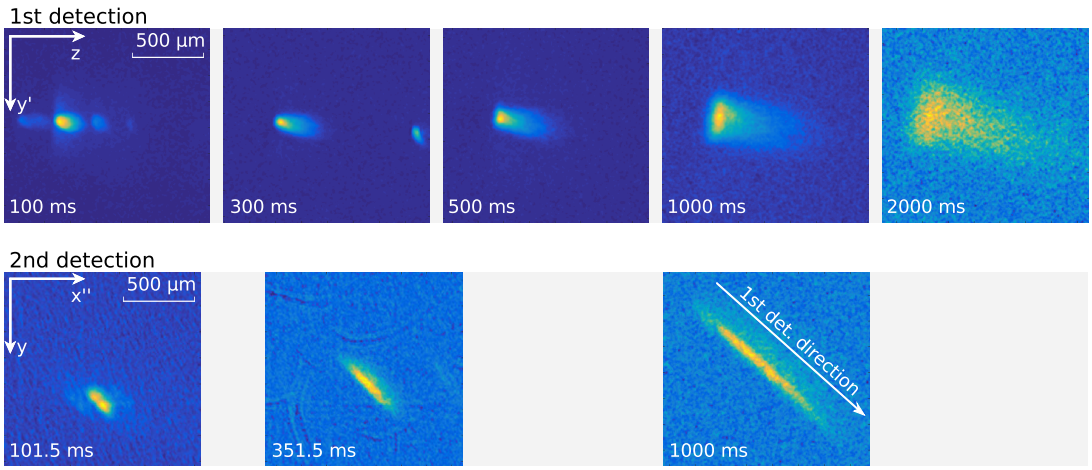

Figure 6.3: TOF series of atomic ensembles after being exposed to the SCBC lens. Images have been taken with the 1st and 2nd detection. The following peculiarities can be noticed: (i) Pronounced tail pointing away from the chip, located at the left image border. (ii) Cloud is sheared against the z-axis, which was expected to be an axis of symmetry. (iii) Existence of a focus somewhere around 300 ms. All pictures feature the same region of interest (ROI) size. (please refer to Fig. 5.1 on p82 for the orientation of the image coordinates)

- **Focus in y'-direction:** The y'-direction is a projection of the x- and y-direction. The lensing force in the x-direction is weak because of the slow axial trap frequency and the expansion along the x-direction should dominate. Anyhow we see a focus in y'-direction at about 300 ms.
- **Rotated cloud:** The cloud is not aligned along the z-axis on the first detection camera, but slightly rotated against it by some degrees. An even stronger rotation of the cloud is visible on the second detection camera.

The discovered peculiarities with the SCBC lens will be analyzed in the following sections. From these considerations we evolve a recipe for an improved lensing scheme, which we call in the further the "BC lens".

6.3.1 Trap dynamics during the lens

Because of the limited agility of the magnetic field creating structures, it is not possible to pulse the trap with a true delta function in time. Thus, we have to take a look at the dynamics of the position and orientation of the principal axes of the trapping potential during the scaling of the currents during the lens pulse. Simulated results for the rotation of the eigenvectors of the trap against the chip coordinate system as well as the translation of the trap minimum for different scaling values of the trap are shown in Fig. 6.4. A quantization field of $B_x = 0.964\,\mathrm{G}$ in x-direction was present

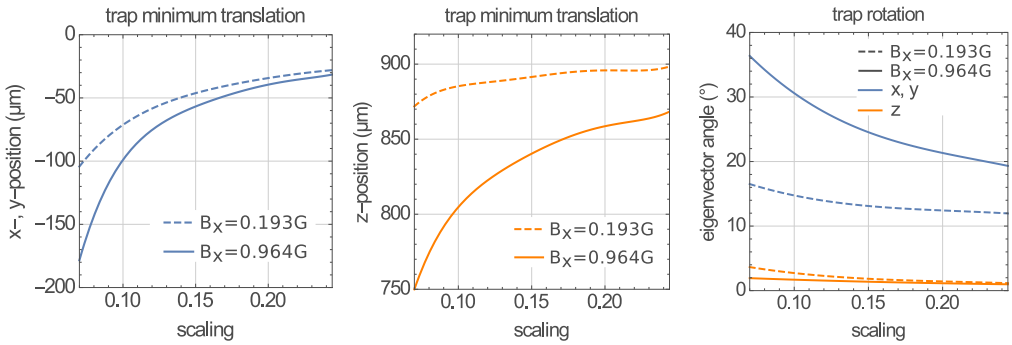

Figure 6.4: Simulation of the trap position and orientation during the lens for a homogeneous magnetic quantization field B_x in x-direction of 0.964 G (solid) and 0.193 G (dashed). During lensing with the SCBC, the trap generating currents are scaled from zero up to a factor of 0.244 of the currents used for the release trap with a Gaussian function in time. During this process, the eigensystem of the trap is rotating mostly around the z-axis and its minimum is being translated. A weaker quantization field leads too reduced lens dynamics. While the simulation indicates that the trap rotation and translation get more dramatic close to zero scaling, it is important to understand that also the trap curvature goes to zero and thus the dynamics at low scalings become alleviated.

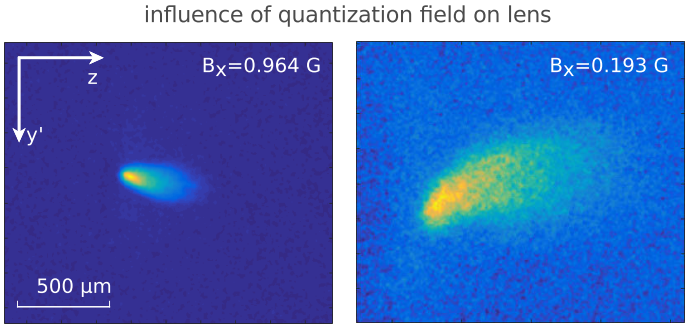

Figure 6.5: Comparison of two equal sequences using a SCBC lens but with different quantization fields B_x during the lens. Both pictures were taken after 300 ms of TOF using the same ROI. The trap dynamics depend on the quantization field strength, resulting in a different orientation and lens strength.

during the lens. A reduction of the quantization field to a value of $B_x = 0.193\,\mathrm{G}$ reduces the rotation of the lens during the pulse by about a factor of two. In this way, also the translation especially in z-direction is reduced by a factor of about three. A further reduction of the quantization field would lead to loss of atoms from the state $|m_F = +2\rangle$ into other Zeeman levels.

An experimental demonstration of the effect is shown in Fig. 6.5, where two equal lensing sequences have been performed in microgravity with a different quantization field. The reduction of the quantization field is leading to a different orientation of the lensed cloud in reference to the chip coordinate system as well as a different cloud size and thus lens force. With the reduced quantization field, the cloud is rotated in the opposite direction, which means that the lensing potential is still exerting a dynamic behavior during the Gaussian current scaling.

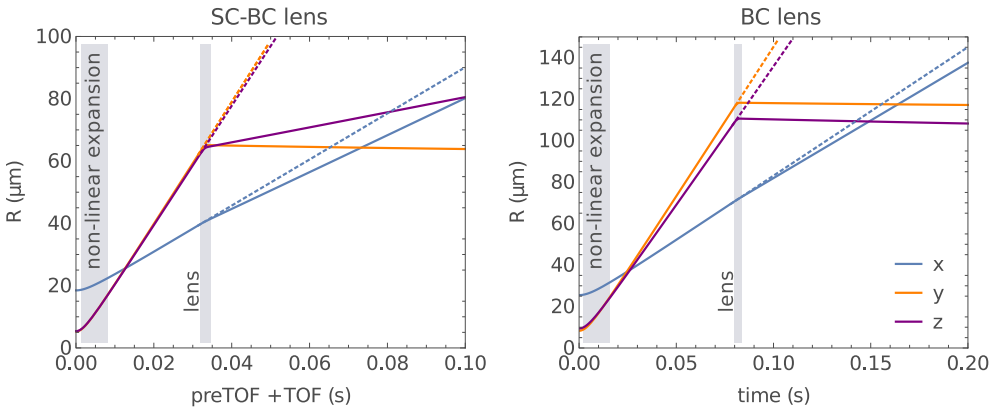

Figure 6.6: Simulation of the SCBC lens following a scaling approach: The lens is reducing the expansion rate for each direction. However, because of the anisotropic trapping frequencies of the SCBC lens it is only possible to collimate, for example, the y-direction (left). An improved lens using just the BC allows for a collimation of the y- and z-direction (right). In the axial x-direction, both lens configurations show the weakest lensing force.

A further manifestation of the trap rotation can be observed when looking at a TOF series of the SCBC lens from the 2nd absorption imaging detection direction (Fig. 6.3). The cloud is rotated by about 42° against the horizontal in the 2nd detection coordinate system. As a consequence, the weak lensed axial direction of the condensate is rotated into the direction of the first detection laser beam. Therefor, the expansion in the axial direction is not visible on the 1st detection and a focus in the radial direction can be thus observed without having the expansion of the weak lensed condensate axis masking the focus in the y'-direction.

The improved BC lens will make use of a different pulsing scheme. For the SCBC lens the y-coil and the SC and BC were pulsed on with a Gaussian function in time. The BC lens will be implemented by ramping on the y-coil to the desired value before the lens and pulsing just the BC with a box pulse. Thus the lens duration is no longer limited by the inductance of the y-coil but exclusively by the speed of the comparatively fast base chip. By using a box-like pulse function, trap rotations and translations can be mitigated to a great extent. In addition, the quantization field will be reduced to a magnetic field strength of 0.19 G.

6.3.2 Astigmatic lens

A characteristic of the Ioffe-Pritchard type trapping potential is the axial symmetry of the trapping frequencies, which can be tuned by adjusting the bias field. Especially for atom chip traps, this characteristic has to be even generalized to three individual trapping frequencies for each direction, with one slow axial and two similar but

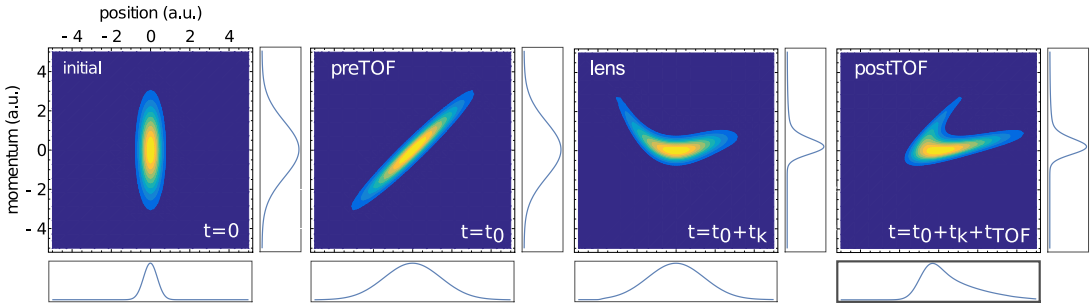

Figure 6.7: Simulation of the phase space density for lensing with an anharmonic potential. The anharmonicity leads to an overcompensation of the momentum on the left side, whereas the change in momentum on the right side is too small. This leads to a banana-shaped phase space distribution. After TOF the distribution in position space becomes asymmetric, showing a pronounced tail.

not compulsory equal fast radial trapping frequencies. As a consequence, the atomic ensemble shows for each direction a different expansion rate. When using the same anisotropic potential with three different trapping for the lens, it is impossible to collimate the ensemble in more than one direction. A scaling approach simulation of the cloud radii evolution after the release and a subsequent SCBC lens is shown in the left plot in Fig. 6.6. It depicts the asymmetric behavior that allows only for a collimation in a single direction. By using solely the BC and tuning the bias field properly, one can achieve a lens configuration that offers two equal radial trapping frequencies. It is then possible to collimate these two radial axes, which is shown in the right picture in Fig. 6.6. While the axial direction still features a substantial expansion rate of $\dot{\sigma}_x = 562\,\mu\mathrm{m\,s}^{-1}$, we will later show an approach that can allow for a reduction of the kinetic energy along this axis by utilizing in-trap density oscillations of the cloud before the release.

6.3.3 Anharmonicities of the magnetic potential

The most striking peculiarity when looking at the SCBC lens TOF series, shown in Fig. 6.3, is the pronounced tail of the atomic ensemble pointing away from the chip surface. To get an understanding from where this tail is arising, we can have a look at a simulation of the lensing potential, shown in Fig 6.8. The potential can be expressed as a polynomial series Eqn. (2.52) with a harmonic expression and higher order terms. It becomes evident that due to the third order term in the potential, the lensing force is asymmetric. This leads to a stronger kick away from the chip surface for the atoms closer to the chip. This translates into the formation of a tail pointing away from the chip after TOF.

In Fig. 6.7, the evolution of the phase space density for a lensing process with an anharmonic potential is shown. Due to the third order term in the potential, the

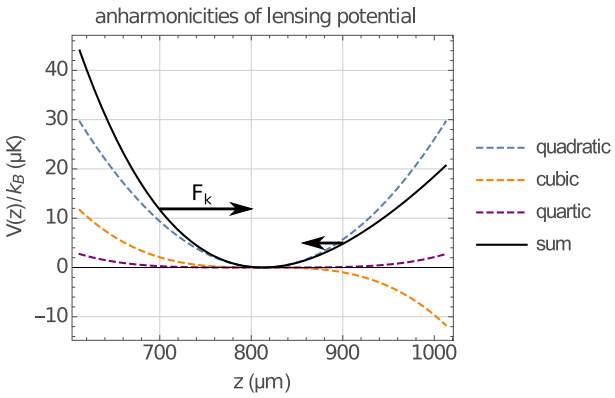

Figure 6.8: Simulated anharmonic magnetic lensing potential: The complete potential (black) is a sum of the harmonic (blue) and higher anharmonic terms (orange and purple). As a consequence, the curvature is not equal everywhere within the trap. For example, at $z = 700\,\mu m$, the atoms experience a stronger kicking force $F_k = -\nabla V$ towards the center of the trap at $z = 800\,\mu m$ as compared to the kick on the opposite side at $z = 900\,\mu m$.

ensemble is not sheared symmetrically, which leads to a banana-shaped distribution. Furthermore, the fourth order anharmonicity is increasing the strength of the lens for atoms further away from the lens center. When looking at the spatial distribution after TOF, the formation of a tail can be explained by the overcompensated initial left part of the distribution which moves quickly to the right side during the time of free evolution. The strength of the anharmonicities is quantified by the L_n coefficients (see Eqn. (2.52). These describe at which distance from the minimum the curvature and thus force exerted on an atom of the anharmonic term of n-th order is equal to the curvature of the harmonic term. L_n values for the magnetic potential of the SCBC lens as well as the improved BC lens are listed in Tab. 6.1. For the SCBC lens, the z-direction shows a strong cubic contribution that creates the tail along the z-direction after TOF. Aside from the cubic term in the y-direction, the cubic and quartic anharmonicities can be reduced largely by using a pure BC lens.

Overall, the anharmonicities are distorting the shape of the phase space distribution and deteriorate the collimation of the atomic ensemble, thus limiting the achievable minimum mean kinetic energy. It is therefor of interest to reduce the anharmonicities of the lensing potential. Furthermore the evaluation of the position, size and atom number of the ensemble is no longer straightforward since the distorted shape of the cloud can be no longer described by a simple set of parameters like the Thomas-Fermi radius. We will later on use a decomposition of the density profile into Hermite-Gaussians modes (see Sec. 6.4.4).

6.4 Improved base chip lens

Thanks to the analysis of the SCBC lens given in the previous three sections, we can now tailor a sequence for an improved lensing scheme. Extensive use was made of the *Mathematica* magnetic field simulation, due to the fact that the intended configurations involve very shallow traps. The gravitational sag would distort the potentials to a

direction	coefficient	SCBC (µm)	BC lens (µm)
x	$L_3 =$	$-20\,130$	$390\,928$
	$L_4 =$	1524	3376
y	$L_3 =$	$-25\,527$	-1764
	$L_4 =$	698	1180
z	$L_3 =$	-339	-909
	$L_4 =$	467	7862

Table 6.1: L_n coefficients describing the strength of the anharmonic term of n-th order: Values for the SCBC lens as well as for the improved pure BC lens are listed. The value L_n describes at which distance from the trap minimum the force on an atom created by the n-th order anharmonic term is equal to the force exerted by the harmonic term. The cubic term is most pronounced for the z-direction. For a pure BC lens configuration, anharmonicities are reduced except for the cubic term in y-direction.

degree at which the atoms are no longer trappable in a lab environment. The BC lens will offer the following improvements:

- reduced anharmonicities of the lensing potential
- collimation in two directions
- reduced dynamics during lens pulse
- tuning of the center of mass motion of the condensate with the lens position

6.4.1 Lens sequence

To reduce the rotation and translation of the trap when pulsing it on and off, a reduced quantization field of 0.193 G will be used. Furthermore the chip simulation was used to calculate the trap frequencies of a pure BC trap depending on the current sent through the y-coil. For a BC current of 6 A and a y-coil current of -0.251 A, the two radial trapping frequencies ω_y and ω_z are equal, with $\{\omega_x, \omega_y, \omega_z\} = 2\pi\{5.46, 22.5, 22.5\}$Hz. An additional benefit of the pure BC trap is the reduced anharmonicity of the trapping potential.

The trap center of the BC lens is located at a position of $z = 1462\,\mu$m. The transition to the BEC is achieved in the final evaporation trap generated by the science and base chip at a position of $z = 209\,\mu$m. Because of the limited microgravity time, we need to transport the atoms over a distance of about 1.2 mm away from the chip to the position of the BC lens within a preferably short time. This can be done by ramping the bias field from a value of -1.5 A down to -0.374 A. As a consequence, the trapping frequencies are reducing from $\{\omega_x, \omega_y, \omega_z\} = 2\pi\{24.4, 457, 462\}$Hz to $\{\omega_x, \omega_y, \omega_z\} = 2\pi\{9.1, 27.9, 24.6\}$Hz. To keep the transfer adiabatic and prevent the excitation of dipole as well as density oscillations in the final trap, this transfer has to be slow

compared to the trapping frequencies. Due to the microgravity time being limited, we take explicit care of the decompression by implementing a transport trajectory that relies on a shortcut to adiabaticity approach (see Sec. 6.4.2). This will allow for a fast quasi-adiabatic decompression with reduced excitations of the condensate in the final trap.

After decompression and transport of the BEC to the BC lens position, all field generating structures, excluding the x-coil, are turned of and the condensate is released from the trap. The ensemble is expanding during a preTOF of $t_0 = 80\,\mathrm{ms}$. After the release, the mean-field energy converts into kinetic energy and drives the expansion in the first 20 ms. A further prolongation of the preTOF would increase distortions because of anharmonicities of the lensing potential becoming more pronounced, thus lowering the collimation quality.

We have seen that the lens is showing a dynamic behavior in respect to its position and orientation when turning it on and off. To reduce these dynamics we will use a box pulse for the BC lens. Therefor, 10 ms before the lens we ramp the y-coil to the desired lens current and then pulse on solely the BC with a box function in time for $t_k = 2.64\,\mathrm{ms}$. Since the BC has a reaction time of less than 200 µs we can assume a box-like pulse behavior of the lens. The y-coil and BC current of the initially proposed lens have been scaled by a factor of 0.3 to reduce the strength of the lens, thus increasing the necessary lens time t_k for a box-like pulse behavior. After the lens, an adiabatic rapid passage transfers about 90 % of the atoms to the non-magnetic state $|m_F = 0\rangle$, followed by a 3 ms long inhomogeneous Stern-Gerlach field to push away residual atoms left in magnetic sensitive states.

Now that we have tailored an improved lensing sequence which takes into account the results of the first SCBC lens, we will focus in the next section on the fast transport of the condensate to the BC lens position.

6.4.2 Fast transport of a Bose-Einstein condensate

For several reasons, the decompression and transport of the condensate further away from the chip is desired in our experiment:

- **Reduced mean-field interaction energy:** After the evaporation, the condensate is compressed in a potential featuring steep trapping frequencies. Due to the high density, the mean-field interaction energy would lead to a fast rate of expansion after release. By ramping down the bias field, the trapping frequencies can be reduced resulting in a decompression of the BEC. This also reduces three-body losses occurring in the dense ensemble, which limit the lifetime of the BEC [140].

- **Transport away from chip surface:** By ramping down the bias field, the condensate is transported further away from the chip. This has the beneficial effect that it leads to an increased time before the expanding condensate would interact with the vacuum chamber or the chip surface. Furthermore, the interferometry beams pointing in the vertical direction are diffracted on the chip edge. Systematic effects from the diffracted interferometry beams close to the chip can be thus reduced by moving the BEC further away from the chip.
- **Symmetric lens configuration in two dimensions:** A magnetic field configuration with two symmetric trapping frequencies can be created further away from the chip.

For two reasons we want to execute the transport of the condensate as fast as possible:

- **Increased experiment cycle time:** We want to reduce the experiment sequence cycle time to enhance the number of measurements during the limited microgravity time.
- **Limited lifetime of the condensate:** The BEC should spend as little time as possible in the compressed trap to reduce the three-body loss induced heating rate. Interaction of the condensate with atoms from the residual background vacuum pressure as well as the chip and vacuum chamber lead to an additional decoherence.

Unfortunately, the decompression cannot be driven arbitrarily fast. Rapid changes of the trapping frequency will excite higher eigenvalues of the eigenspectrum of the Hamiltonian during the decompression. This will result in dipole as well as density oscillations of the BEC in the final decompressed trap. To prevent this, one has to satisfy the quantum adiabaticity criterion, which states that the change in trapping frequency has to be well below the instantaneous trapping frequency [141] during the decompression:

$$\left| \frac{\sqrt{2}}{8} \frac{\dot{\omega}(t)}{\omega^2(t)} \right| \ll 1. \tag{6.6}$$

For a linear decompression over a time t_f, this criterion can be expressed as

$$t_f \gg \frac{1}{8\sqrt{2}\omega(t_f)} \left(\frac{\omega^2(0)}{\omega^2(t_f)} - 1 \right). \tag{6.7}$$

In our case, we want to reduce the trapping frequency along z-direction from $\omega(0) = 2\pi \cdot 264\,\mathrm{Hz}$ to $\omega(t_f) = 2\pi \cdot 24.6\,\mathrm{Hz}$. Eqn. 6.7 then tells us that this process should take significantly longer than 200 ms. Adiabaticity would be thus reached for transport times in the range of multiple seconds. Since we are limited by the microgravity time

of 9 s during a catapult flight we have to find a reasonable trade-off between speed of the decompression and the tolerable amount of excitations.

Over the course of the last few years, the controlled rapid transport of ultra-cold atoms has gained an increased amount of attention not only within the precision metrology community. For example, it is also of interest in quantum simulation and computing. Today, many experiments and theory discussions are dealing with the problem of how to transport or load atoms into a different trap geometry within a limited time (for a comprehensive list see [142]). One way of approaching this problem is by making use of optimal control theory. In a recent work of Mennemann et al. [143] the problem has been treated by taking into account the full three-dimensional Gross-Pitaevskii equation and minimizing a cost function depending on a set of control parameters with a variational approach. The cost function is represented as a measure of the overlap between the calculated and the desired final state. Another well established approach to tackle this problem is the so-called "shortcut to adiabaticity". This term was first introduced by Chen et al. [144] in 2010 and describes a technique that is modeling a fast transition of the Hamiltonian. Just like in optimal control theory, this rapid change of the Hamiltonian is in itself allowed to violate the quantum adiabaticity criterion (6.6), but it should end up with a set of final eigenstates one would achieve after an adiabatic process. The shortcut approach is based on the use of Lewis-Riesenfeld invariants to inverse engineer the evolution of the harmonic oscillator frequency with given initial and final frequency values without inducing excitations in the final state.

Calculation of the trap trajectory

In the following, the calculation of an optimized ramp with a shortcut to adiabaticity approach will be described. The calculations of the ramp were kindly provided by Robin Corgier. The approach is based on inverse engineering to find a trajectory for an adiabatic transport that is respecting a set of boundary conditions for the initial and final state. The general problem is depicted in Fig. 6.9.
The following variables will be used in the next steps to characterize the transport:

$$\begin{aligned} z(t) &\quad \dots \quad \text{position of the atoms} \\ z_0(t) &\quad \dots \quad \text{position of the trap} \\ \omega_0(t) &\quad \dots \quad \text{trapping frequency} \end{aligned}$$

We are searching now for a solution to the classical equation of motion for the harmonic oscillator:

$$\ddot{z} + \omega_0^2[z_0](z - z_0) = 0 \tag{6.8}$$

The following boundary conditions are imposed for the initial and final states at times

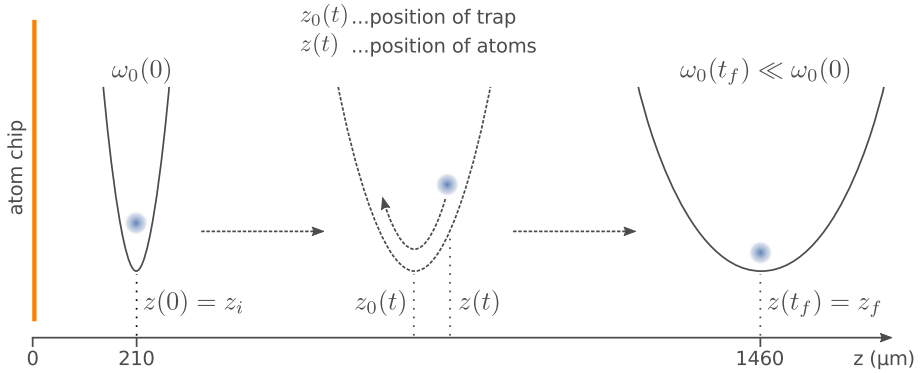

Figure 6.9: Transport of the condensate from the position of the evaporation trap $z_i = 210\,\mu m$ over a distance of 1.2 mm to the base-chip lens position at $z_f = 1460\,\mu m$. An elaborated trap trajectory $z_0(t)$ transports the atoms from their initial position z_i to the final position z_f. During translation of the trap, its trapping frequency is lowered. While the condensate is allowed to be excited during the transport, it should end up in a state that resembles the eigenstates of an adiabatic transport.

$t_i = 0$ and t_f:

$$\begin{array}{rcrcl} & \text{initial} & & \text{final} & \\ z(0) = & z_i & & z(t_f) = & z_f \\ \dot{z}(0) = & 0 & & \dot{z}(t_f) = & 0 \\ \ddot{z}(0) = & 0 & & \ddot{z}(t_f) = & 0 \\ z_0(0) = & z_i & & z_0(t_f) = & z_f \\ \dot{z}_0(0) = & 0 & & \dot{z}_0(t_f) = & 0 \\ \ddot{z}_0(0) = & 0 & & \ddot{z}_0(t_f) = & 0 \end{array} \tag{6.9}$$

The boundary conditions for the motion of the trap center are necessary, because the translation of the trap has to be smooth at the beginning and the end. This is necessary due to the finite reaction time of the field generating structures. Furthermore they prohibit an excess of the total classical energy at the beginning and the end of the decompression:

$$E_{tot}(t) = \frac{1}{2}m\dot{z}^2(t) + \frac{1}{2}m\omega_0^2[z_0(t)](z(t) - z_0(t))^2 \tag{6.10}$$

$$E_{tot}(0) = 0 \tag{6.11}$$

$$E_{tot}(t_f) = 0 \tag{6.12}$$

The following time-dependent function for the position of the atoms was calculated,

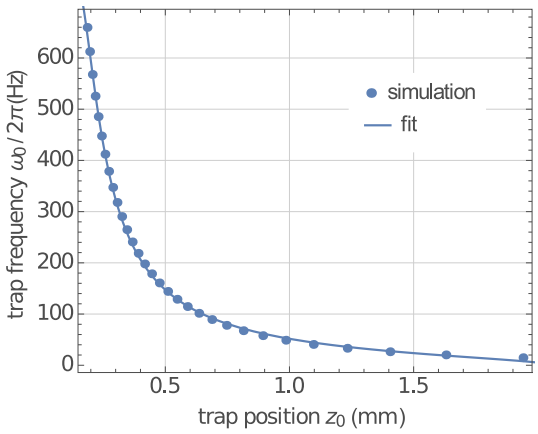

Figure 6.10: Simulated trapping frequencies $\omega_0/2\pi$ in z-direction for different trap positions z_0 and the fitted analytical expression. The fit shows a slight deviation from the calculated data for positions far away from the chip. When ramping the trap away from the chip by reducing the bias current in the y-coil, the trapping frequency reduces and thus the trap is decompressed. Furthermore, the condensate becomes more prone to the excitation of oscillations due to low trapping frequencies at the end of the trajectory.

using an inverse engineering approach by obeying the boundary conditions (6.9):

$$z(t) = z_i + \frac{z_f - z_i}{48\pi}[48\pi t - 27\sin(2\pi t) + \sin(6\pi t)] \tag{6.13}$$

Since we want to use this atom trajectory to solve the equation of motion (6.8) to find a trajectory of the trap center, we still need the instantaneous trap frequency $\omega_0(z_0)$ at its position z_0. To get an analytical expression for $\omega_0(z_0)$, we calculate the trap frequencies at given points using the chip simulation and apply a fit based on a Padé approximation:

$$\omega_0(z_0) = \frac{\alpha + \beta z_0}{1 + \gamma z_0 + \zeta z_0^2} \tag{6.14}$$

The results of the chip simulation and the fitted analytical expression is shown in Fig. 6.10. Given this analytical expression, we can now solve the equation of motion resulting in the following trajectory:

$$z_0^{\pm}(t) = \frac{-(\gamma\ddot{z}(t) - \alpha + \beta z(t)) \pm \sqrt{\Delta(t)}}{2(\zeta\ddot{z}(t) - \beta)}, \tag{6.15}$$

with

$$\Delta(t) = (\gamma\ddot{z}(t) - \alpha + \beta z(t))^2 - 4(\zeta\ddot{z}(t) - \beta)(\ddot{z}(t) + \alpha z(t)). \tag{6.16}$$

Only the solution (6.15) with a negative sign yields a physical trajectory.

Application in microgravity

The calculated function for decompression and translation of the BEC from the evaporation trap to the position at which the BC lens shall be used has been tested in the drop tower. The decompression and translation is achieved by simply ramping down

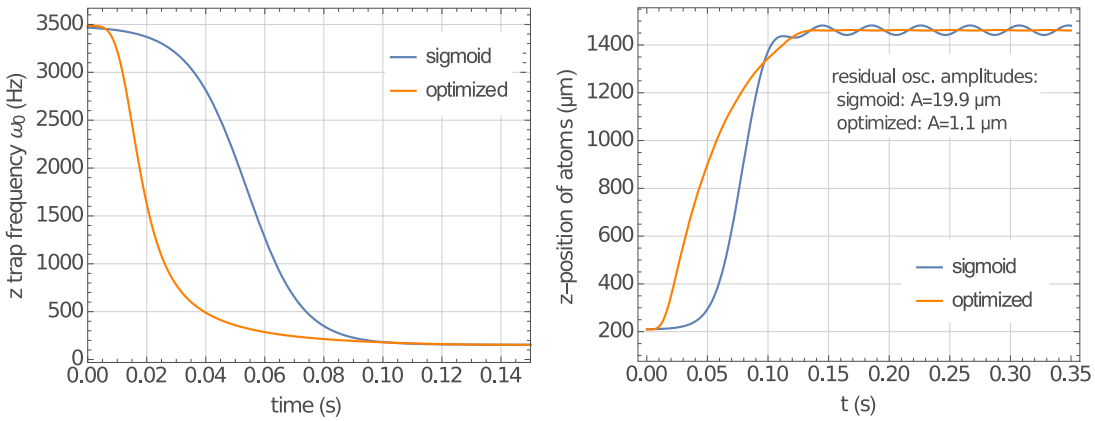

Figure 6.11: Comparison of a 150 ms long ramp-out of the atomic ensemble utilizing a sigmoid or an optimized ramp: Evolution of the trapping frequency (left). Simulation of the position of the atomic ensemble (right). At low trap frequencies, the atomic ensemble is more sensitive to changes in the trap frequency. Hence, the optimized ramp is changing the trapping frequency at a slower speed at the end of the ramp-out. This leads to a reduction of the residual oscillation amplitude after the ramp-out by a factor of about 20. Furthermore the atoms spend less time in the compressed trap with high trapping frequencies, which reduces three-body losses.

the current in the y-coil with the optimized decompression function. In Fig. 6.11, the difference between a sigmoid-shape ramp and the optimized ramp is depicted. The optimized ramp executes the bulk of the trap frequency changes in the beginning of the ramp while the instantaneous trap frequency is still high. Later on, when the trap frequency is lower, the optimized ramp changes the trap frequency more slowly. As a consequence, the oscillation amplitude in the holding trap after the ramp-out is reduced by a factor of 20 compared to the standard sigmoid ramp.

In a series of four drops, the oscillation in the holding trap has been investigated after ramping the atomic ensemble away from the chip by about 1.2 mm using the optimized ramp. The position of the atoms after 100 ms has been measured and a function describing the oscillation fitted. From this fit the oscillation inside the trap can be calculated (see Eqn. (5.2)). In Fig. 6.12, the measured data and the fit are depicted together with a comparison of the deduced in-trap oscillation with a simulated oscillation (see also Tab. 6.2). The frequency and position show a good agreement but the oscillation amplitude is by a factor of 4.5 larger than the simulation predicts. A phase difference of about π can be observed, which has been already encountered in the analysis of the decompression of the trap in Sec. 5.5.1. Nevertheless, the simulation delivers a good approximation of the ramp-out dynamics concerning the final oscillation amplitude, frequency and offset.

Although the excitation of dipole oscillations is handled well with the used decompression ramp, the condensate is showing some density oscillations. We will investigate

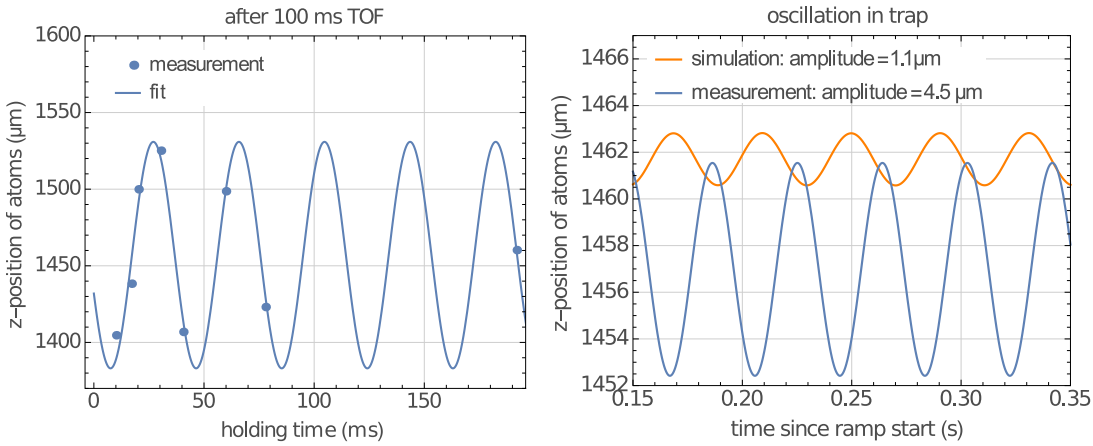

Figure 6.12: Measured position of the atoms in microgravity after using an optimized ramp-out and subsequent 100 ms of TOF (left). The position uncertainty is below 1 µm and error bars have been omitted. An oscillating function has been fitted to the data (Eqn. (5.2)). This function yields the parameters for the in-trap oscillation which is compared with a simulation (right).

	simulation	**measurement**
amplitude	1.1 µm	4.5(5) µm
center	1461.7 µm	1457.0(55) µm
frequency	24.6 Hz	25.7(2) Hz

Table 6.2: Comparison of the measured and simulated in-trap oscillations in z-direction after ramping the condensate over a distance of 1.2 mm away from the chip within 150 ms.

them later in Sec. 6.4.7 and argue that these oscillations can be used to reduce the expansion rate of the condensate in the x-direction in which the magnetic lens is exerting only a weak force.

6.4.3 Base chip lens in microgravity

A TOF series of the BC lensed ensemble has been recorded in a series of drops. An overview picture of the lensed ensemble after different TOF is shown in Fig. 6.13. From looking at the pictures it becomes evident that the cloud rotation against the z-axis of the first detection images, as observed with the SCBC lens, is now absent. Furthermore, the rotation of the cloud, as seen from the 2nd detection, is also reduced. Therefor, the axial direction of the cloud becomes visible on the first detection direction. In the following section, we will focus on the detailed analysis of the rate of expansion of the condensate.

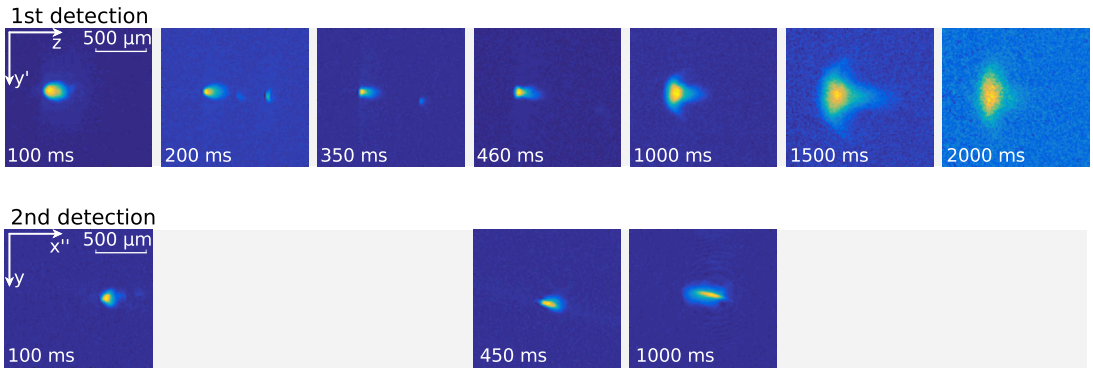

Figure 6.13: TOF Series of an atomic ensemble lensed with the improved BC lens. In comparison to the first SCBC lens, the ensemble is no longer rotated against the z-axis on the first detection and the tail of the anharmonicities is less pronounced. Also, the rotation of the cloud on the second detection is reduced. For reasons of comparability, the same ROI like in Fig. 6.3 has been used.

6.4.4 Hermite-Gaussian decomposition

The application of an anharmonic lensing potential to the initial released distribution results in a distortion of the wave packet. It is therefor no longer possible to describe the spatial evolution of the ensemble in the individual directions by a single parameter like the Thomas-Fermi radius. Just like in Gaussian optics, we will decompose the measured two-dimensional density $N(I, J) \in \mathbb{N}_0$ with coordinates I, J into a set of subcomponents that are linked together by a set of Hermite polynomials. We can then focus on the fundamental Gaussian (0,0) mode and reconstruct its temporal evolution in three dimensions from a set of given 2D projections as seen from the two viewing angles of the first and second detection direction.

One-dimensional description

The decomposition of a given function $f(x)$ into series represented by Hermite polynomials is a mathematic formalism used in Gaussian optics or in the description of the eigenstates of the quantum harmonic oscillator. In the following we will explain this formalism and show how it can be applied to the measured density distributions of the lensed ensembles.

Every function that is asymptotically Gaussian can be approximated by a series of Hermite polynomials

$$H_n(x) = (-1)^n e^{-x^2} \frac{d^n}{dx^n} e^{-x^2}. \tag{6.17}$$

The Hermite polynomials are orthogonal, fulfilling the relation

$$\int_{\infty}^{\infty} H_m(x)H_n(x)e^{-x^2}dx = \sqrt{\pi}2^n n!\delta_{nm}. \tag{6.18}$$

Using Hilbert space notation we can use the Hermite polynomials to form a set of normalized basis functions

$$\langle x|n\rangle = \frac{H_n(x)}{\sqrt{\sqrt{\pi}2^n n!}}e^{-\frac{x^2}{2}}, \tag{6.19}$$

which form a complete set:

$$\mathbb{1} = \sum_{n=0}^{\infty} |n\rangle\langle n|. \tag{6.20}$$

Thus, every function $f(x)$ can be expressed in terms of Hermite polynomials using the relation

$$f(x) = \sum_{n=0}^{\infty}\langle x|n\rangle f_n = \sum_{n=0}^{\infty}\frac{1}{\sqrt{\sqrt{\pi}2^n n!}}H_n(x)e^{-\frac{1}{2}x^2}f_n, \tag{6.21}$$

with the general underlying function e^{-x^2} and the amplitudes f_n given by

$$f_n = \int_{-\infty}^{\infty} f(x)\frac{H_n(x)}{\sqrt{\sqrt{\pi}2^n n!}}e^{-\frac{1}{2}x^2}dx. \tag{6.22}$$

Two-dimensional description

An expansion of the upper description to two dimensions is straightforward. The basis is extended to two dimensions I, J

$$\langle x|n_I\rangle\langle y|n_J\rangle = \frac{H_{n_I}(x)}{\sqrt{\sqrt{\pi}2^{n_I}n_I!}}\frac{H_{n_J}(y)}{\sqrt{\sqrt{\pi}2^{n_J}n_J!}}e^{-\frac{1}{2}(x^2+y^2)}. \tag{6.23}$$

Thus, the function $f(x, y)$ can be written as

$$f(x,y) = \sum_{n_i,n_j=0}^{\infty}\langle x|n_I\rangle\langle y|n_J\rangle f_{n_I,n_J}, \tag{6.24}$$

with the amplitudes given by

$$f_{n_I,n_J} = \int_{-\infty}^{\infty} f(x,y)\langle x|n_I\rangle\langle y|n_J\rangle d^2xy. \tag{6.25}$$

To improve the quality of the Hermite-Gaussian representation of a given distribution $N(I,J)$, we can rotate the distribution around its center of mass coordinates $(\bar{I},\bar{J})$ by an angle θ and stretch it in I- and J-direction by a factor s_I and s_J. The rotated coordinates I',J' thus can be expressed as

$$I' = \frac{\cos\theta(I-\bar{I})+\sin\theta(J-\bar{J})}{s_I} \tag{6.26}$$

$$J' = \frac{-\sin\theta(I-\bar{I})+\cos\theta(J-\bar{J})}{s_J}. \tag{6.27}$$

Analysis of the lensed ensembles

The Hermite-Gaussian (HG) decomposition is implemented as a *MATLAB* routine, which was kindly provided by Prof. Dr. Reinhold Walser from the Technische Universität Darmstadt. It is using the processed absorption images with coordinates I and J, showing the optical density of the cloud $N(I,J)$. One of the main functions of the program is a Gaussian fitting routine that rotates the data by an angle of θ and stretches the image by factors s_I and s_J in the two directions until a fit of a symmetric 2D Gaussian to the rotated and scaled data is optimal. This function is in a first step used to calculate the approximate center of the data as well as the widths s_I, s_J and the rotation angle θ. The image is then cropped to a selectable range to reduce the amount of data to be processed. After cropping, the Gaussian fitting routine is again evaluated on the cropped region to get values for the center, s_I, s_J as well as the rotation angle θ of the fundamental (0,0) Hermite-Gaussian mode. In a final step, the non-Gaussian wings are interpolated by higher order Hermite-Gaussian modes by minimizing the error functional

$$E(f,\mu)=\sum_{I,J}\left(N(I,J)-\sum_{n_I,n_J}\langle I,J|n_I,n_J\rangle f_{n_I,n_J}-\mu\right)^2, \tag{6.28}$$

where μ is a constant offset and f_{n_I,n_J} are the amplitudes of the (n_I,n_J) Hermite-Gaussian mode. Minimality is reached if the gradient $(\partial_\mu E,\partial_{f_{r,s}}E)=0,\forall(r,s)$ vanishes and the Hessian matrix is positive.

An example for a Hermite-Gaussian decomposition is shown in Fig. 6.14. A decomposition into Hermite-Gaussian modes up to order of $n=12$ has been used for a BC lensed ensemble after 500 ms of TOF. The reconstruction shows that the fundamental amplitude $f_{0,0}$ is mostly dominating the distribution, leading to a relative population of 88 % in the $(0,0)$ mode. Few higher modes are necessary to describe the distribution, leaving only minimal residuals. The recorded and decomposed density profiles of the BC lensed ensembles feature about $84-92\%$ of the atoms in the (0,0) mode. This represents an improvement when compared to the SCBC lensed ensembles which had

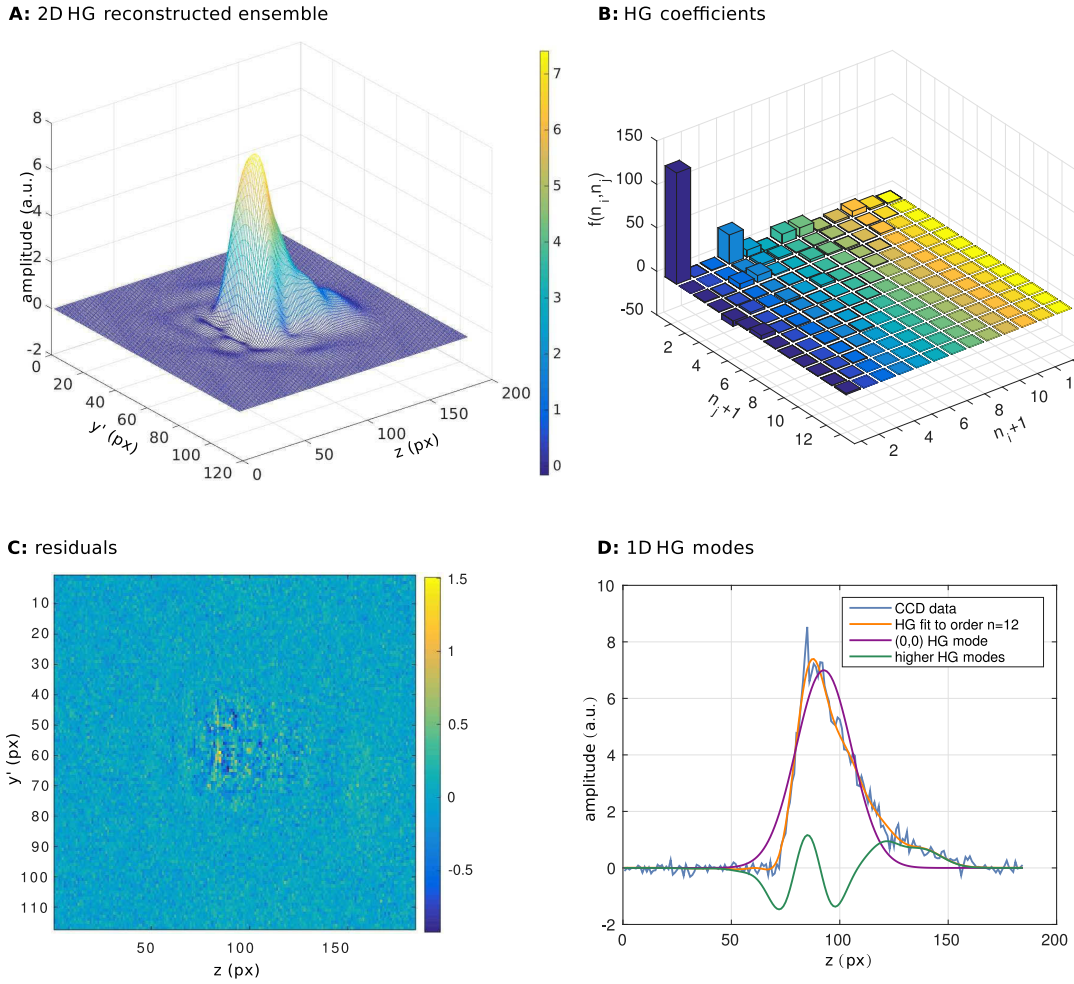

Figure 6.14: Hermite-Gaussian reconstruction of the density of a BC-lensed distribution after 500 ms of TOF: (A) Two-dimensional HG-reconstruction of the measured distribution. (B) HG-coefficients $f(i,j)$. 88 % of the atoms are accommodated in the (0,0) mode. (C) Residuals showing that the reconstruction is an adequate representation of the measured density. (D) Plot of the measured data, the (0,0) mode, the higher modes and the complete reconstruction.

a lower fraction of about $70 - 80\%$ in the fundamental mode.

6.4.5 Calculation of the condensate width in three dimensions

We now apply the Hermite-Gaussian decomposition to the BC lens TOF series to get a measure of the rate of expansion of the atomic ensemble. We will focus on the fundamental Hermite-Gaussian (0,0) mode to attribute a single number for the rate of expansion to every direction. The amplitude of the higher modes can be used to characterize the strength of the anharmonicities. For a full 3D analysis, we deduce the evolution of the condensate's fundamental mode size by calculating its size from the measured projections. We assume to know the orientation of the detection coordinate systems with respect to the chip coordinate system. Furthermore, we assume to know the orientation of the cloud within the chip coordinate system. Therefor, we can calculate the widths of the condensate along its principal axis by retracing them from the measured projections. We will simplify the spatial 3D Gaussian distribution of the fundamental mode to a system of three orthonormal vectors describing its orientation. The length of these vectors are describing the width of the fundamental mode.

In the following, we will use a notation that describes the principal axes of the cloud by vectors $\mathbf{b_{i,0}}$ (with $i = \{x, y, z\}$) that are parallel to the chip coordinate vectors $\mathbf{e_i}$ for the case that the cloud is not rotated. The lengths of the vectors $\mathbf{b}$ correspond to the width σ of the condensate in the respective direction. On the 2nd detection system we observe a rotation of the cloud of about $\alpha = -6.7°$ against the x"-axis. Since we know that the 2nd detection system is rotated by $\beta = 37.5°$ around the y-axis, we can calculate the rotation angle of the cloud around the z-axis:

$$\gamma = \tan^{-1}(\tan(\alpha)\sin(\pi/2 - \beta)) = -5.3°. \tag{6.29}$$

This is valid if we assume that the cloud is only rotated around the z-direction. This assumption stems from the observation that the cloud is not rotated in the 1st detection images. We can now rotate the initial cloud vectors $\mathbf{b}_0$ around the z-base vector using a rotation matrix to get the proper orientation of the cloud observed on the absorption images:

$$\mathbf{b_i} = R_z(\gamma) \cdot \mathbf{b_{i,0}} = \begin{pmatrix} \cos(\gamma) & -\sin(\gamma) & 0 \\ \sin(\gamma) & \cos(\gamma) & 0 \\ 0 & 0 & 1 \end{pmatrix} \cdot \mathbf{b_{i,0}}. \tag{6.30}$$

We are now interested in the projections of the vectors $\mathbf{b}$ when looking at them from the 2nd detection angle view. Therefor, we need to calculate the vectors of the 2nd detection coordinate system $\mathbf{e''}$. This can be done by turning the chip coordinate

vectors $\mathbf{e}$ around the y-direction by the 2nd detection angle $\beta = 37.5°$:

$$\mathbf{e_i}'' = R_y(\beta) \cdot \mathbf{e_i} = \begin{pmatrix} \cos(\beta) & 0 & \sin(\beta) \\ 0 & 1 & 0 \\ -\sin(\beta) & 0 & \cos(\beta) \end{pmatrix} \cdot \mathbf{e_i}. \tag{6.31}$$

Since we do not want to get the projections of the cloud vectors $\mathbf{b}$ on the 2nd detection coordinate system, but rather on the principal axes of the cloud visible on the 2nd detection image, we rotate the vectors $\mathbf{e}''$ by the angle α observed on the 2nd detection around the normal direction $\mathbf{e_z}''$, thus arriving at corrected 2nd detection coordinates

$$\mathbf{e}''_{\mathbf{i,c}} = R_{z''} \cdot \mathbf{e}''_{\mathbf{i}} = \begin{pmatrix} e''^2_{z,1}(1-\cos\alpha) + \cos\alpha & -e''_{z,3}\sin\alpha & e''_{z,1}e''_{z,3}(1-\cos\alpha) \\ e''_{z,3}\sin\alpha & \cos\alpha & -e''_{z,1}\sin\alpha \\ e''_{z,3}e''_{z,1}(1-\cos\alpha) & e''_{z,1}\sin\alpha & e''^2_{z,3}(1-\cos\alpha) + \cos\alpha \end{pmatrix} \cdot \mathbf{e}''_{\mathbf{i}}, \tag{6.32}$$

where $e''_{z,i}$ is the i-th component of the 2nd detection unit z-vector. The observable widths b''_1 and b''_2 in the 2nd detection system are then given by the projections

$$b''_1 = \sqrt{(\mathbf{b_{x,c}} \cdot \mathbf{e''_x})^2 + (\mathbf{b_y} \cdot \mathbf{e''_{x,c}})^2 + (\mathbf{b_z} \cdot \mathbf{e''_{x,c}})^2} \tag{6.33}$$

$$b''_2 = \sqrt{(\mathbf{b_{x,c}} \cdot \mathbf{e''_y})^2 + (\mathbf{b_y} \cdot \mathbf{e''_{y,c}})^2 + (\mathbf{b_z} \cdot \mathbf{e''_{y,c}})^2}. \tag{6.34}$$

The widths b''_1, b''_2, and b_z are observable from the 1st and 2nd detection system respectively, and we calculated the orientation of the cloud principal axis $\mathbf{b}$ as well as the 2nd detection coordinate system $\mathbf{e''_c}$. We can then solve the equation system to get the widths b_x and b_y.

6.4.6 Evolution of the condensate width after the lens

The evolution of the widths of the condensate after the BC lens is shown in Fig. 6.15. The data points in z- and y'-direction are recorded from direct observation with the 1st detection. Four data points for the x- and y-direction, two at 450 ms and two at 1000 ms, are calculated from the projected observed widths from the 1st and 2nd detection. The error bars for the z- and y'-direction arise from an assumed error in the atom number estimation of 10 %, which results in an error of the rescaled width of about 2 % (see Eqn. (2.22)). The error bars for the x- and y-direction are calculated via uncertainty propagation from the retracing of the cloud size projections, described above. Since we do not have the possibility to extract the atom number from the 2nd detection pictures, we assume a mean atom number of about 100 000 and use a rather large uncertainty of the actual atom number of 50 % leading to a uncertainty of the rescaled widths of about 14 %.

The data points show clearly that the applied BC lens leads to a focus in the z- and

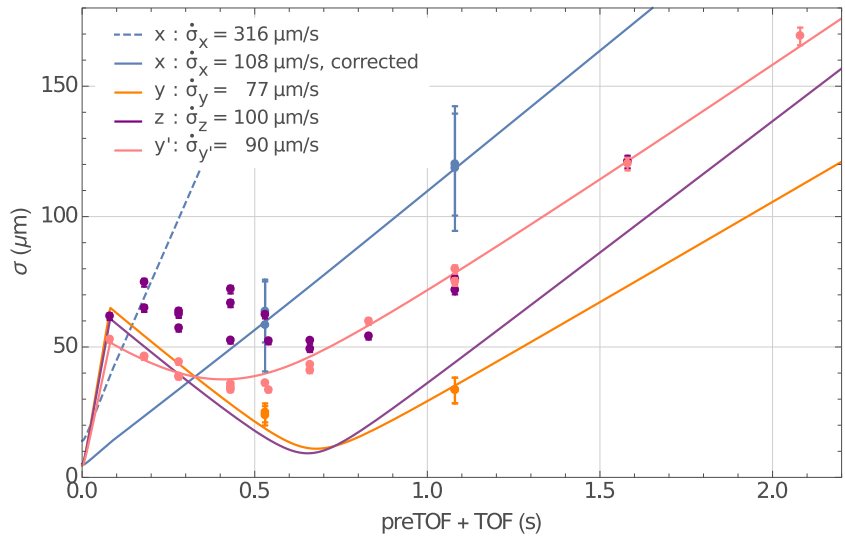

Figure 6.15: Evolution of the width of the condensate for a BC lens sequence: The width of the condensate is given in terms of the width σ of the fundamental Hermite-Gaussian (0,0) mode. A scaling approach has been used to simulate the evolution of the widths. The expansion in x-direction (dashed) has to be corrected by a factor of 0.34 to achieve correspondence with the measurement. In the following it will be shown that the input state of the lens has to be taken into account to fully understand the lensing process. The listed expansion rates refer to the evolution of σ in the far field.

y'-direction. Since the y'-direction is a projection of the x- and y-direction and the used lens is too weak to even just collimate the x-direction, we can deduce that the focus in the y'-direction stems from a focus in the y-direction. Also shown in the plot is a scaling approach solution of the complete lensing sequence starting at the release.

The first data points at $t = 80\,\mathrm{ms}$ were taken from a picture of the released cloud after the preTOF at exactly the time of the lens and thus resembles the input state of the lens. The conversion factor between the Thomas-Fermi radius and the standard deviation of the TF distribution $\sigma/R = \sqrt{1/5} \approx 0.447$ has been enlarged to a factor of 0.55 for the calculated curves so that the first data points at $t = 80\,\mathrm{ms}$ correspond to the scaling approach. The simulated lens strength was increased slightly by 8.5 %, so that the foci occur at the right times t. This correction could be justified by the quartic anharmonicities of the BC-lens, which would increase the lens strength. Furthermore, it becomes evident that the Hermite-Gaussian decomposition does not perfectly describe the evolution of the condensate width in z-direction around the focus of the lens. A strong focus in the z-direction cannot be observed on the experimental data. In the far field however, the simulation results a comparable expansion rate, while there still exists an offset in the width. One of the most striking results is that

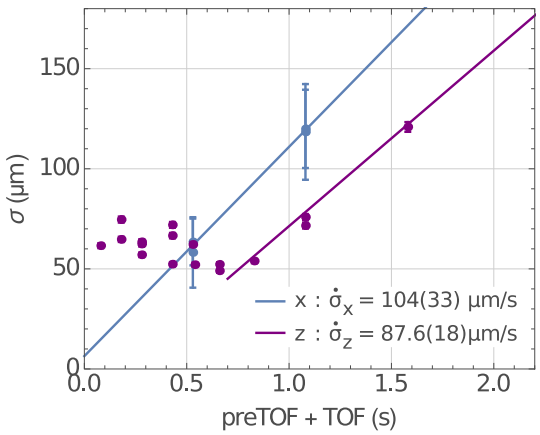

Figure 6.16: Evolution of the width of the lensed condensate in x- and z-direction. The width σ is given in terms of the width of the fundamental Hermite-Gaussian mode. The width in z-direction could be extracted directly from the 1st detection, while the evolution in x-direction has been reconstructed from the widths recorded with the 1st and 2nd detection. For the z-direction, only data points in the linear far-field regime of expansion have been fitted.

direction	**rate of expansion** $\dot{\sigma}(\mu\mathrm{m\,s^{-1}})$	**effective temperature** $\mathbf{T_{1d}}$ (pK)
x	104 ± 33	114^{+83}_{-61}
y	77.1 ± 6.9	62.1^{+12}_{-10}
z	87.6 ± 1.8	80^{+4}_{-3}

Table 6.3: Calculated expansion rates of the BC lensed ensemble. The respective one-dimensional effective temperature is given as a figure of merit. The achieved results represent the lowest values ever achieved for three dimensions (see Sec. 7.5).

the predicted expansion in the x-direction (dotted blue) is reduced by a factor of 0.34 (solid blue). We will see in the next section that the initial condition of the condensate in the release trap has to be taken into account to get a more profound understanding of the lens behavior.

To get proper values of the expansion rate of the cloud, we now look at the evolution of the sizes in all three directions. The z-direction is directly observable and we can use a linear fit on the data points for times greater than 700 ms, for which the expansion enters a linear regime. The expansion in x-direction is coming from a fit of the 3D reconstructed widths. The lens is very weak in the x-direction and we can therefor assume that we are surely in a linear expansion regime. It is thus possible to apply a linear fit to all four data points. Both fits are shown in Fig. 6.16. The expansion rate for the y-direction is coming from the scaling approach shown in Fig. 6.15. The expansion rates $\dot{\sigma}$ are listed in Tab. 6.3 together with the corresponding effective one-dimensional temperatures $T_{1\mathrm{D}}$, which were calculated from Eqn. (2.64).

Data points with a TOF larger than 1.5 s have been neglected in the evaluation since the ensemble is becoming increasingly dilute for a longer TOF due to the detection noise as well as the decoherence of the condensate wave function stemming from the vacuum pressure limited lifetime. This not only leads to a reduction of the measured

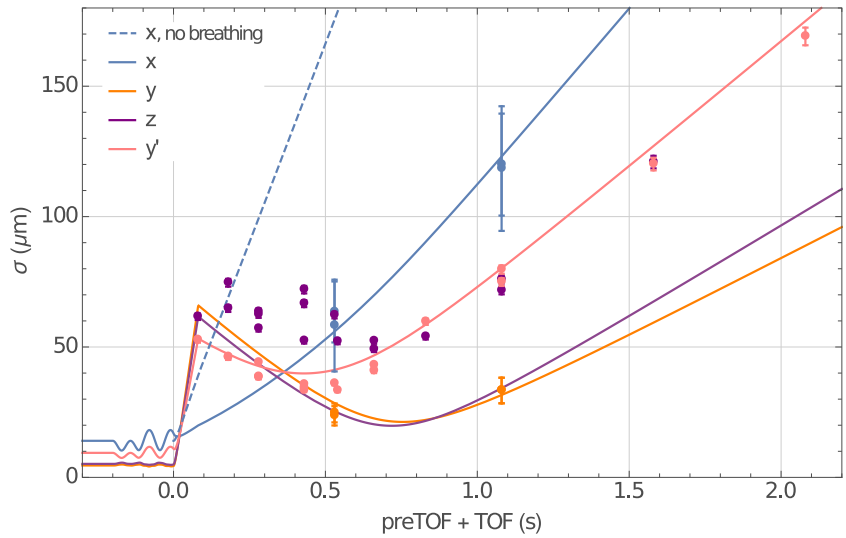

Figure 6.17: Influence of the input state on the lensed ensemble: A pronounced density oscillation in x-direction is induced by a rapid change of the trapping frequency between $t = -0.2\,\mathrm{s}$ and $t = -0.1\,\mathrm{s}$. The kinetic energy in x-direction can be then minimized by turning off the trap at a point of time at which the condensate radius is retracting. The expansion of the static ensemble in the release trap is depicted as a dashed line.

atom number in the condensate but also a broadening of the width of the ensemble for prolonged TOF.

6.4.7 Influence of the lens input state

As we have seen from Fig. 6.15, the scaling approach is not predicting a substantial reduction of the expansion rate along the x-direction. A correction factor had been thus introduced to reach agreement with the experimental data. In the following, however, we will show that a density oscillation in the holding trap before the release of the condensate can lead to the observed lowered expansion rate in x-direction. To this end, the trapping frequencies before the release have been modified in the simulation. At $t = -0.3\,\mathrm{s}$ The atoms are held within the trap with the original trapping frequencies, followed by a rapid change of the frequencies at $t = -0.2\,\mathrm{s}$ to introduce density oscillations of the cloud size. After a variable holding time the trapping frequencies jump back to the original holding trap before finally being reduced to zero for the release. The scaling approach solution for the evolution of the BEC is shown in Fig. 6.17. Density oscillations are excited by increasing the trapping frequency in x-direction by a factor of 1.2 and tuning the holding time so that the cloud is retracting in x-direction at the time of switch-off. In this way, the kinetic energy in x-direction can be reduced at the time of release. The expansion of the cloud in x-direction without a density

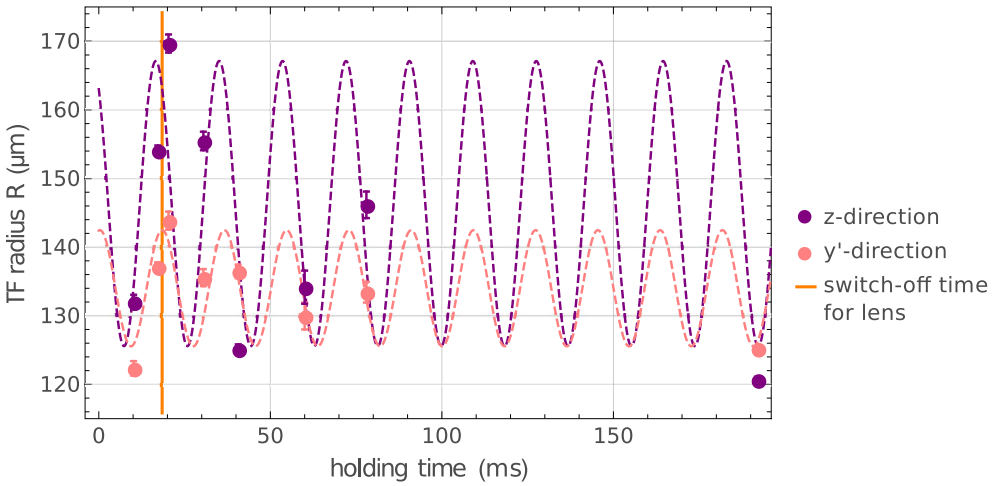

Figure 6.18: Density oscillations after the optimized ramp-out: Shown are the Thomas-Fermi radii of the cloud after 100 ms of TOF. An in-phase oscillation of the condensate radius in z- and y'-direction is visible. The trap is turned off after a holding time of $t = 18.46$ ms. At this point of time, the size in z-direction reaches a maximum after TOF, which means that the kinetic energy along this direction is maximal in the trap. This in turn means that for a quadrupole oscillation the kinetic energy in x-direction is minimal.

oscillation is plotted dashed for comparison.

The simulation of the ramp out of the condensate to the BC lens position does not predict a dipole oscillation in the x- and y-direction. Anyhow, an oscillation in y'-direction of $0.36(8)\,\mu$m has been measured. This is hinting to the fact that a residual magnetic field is disturbing the ramp-out trajectory. During measurements on ground, a magnetic field in z-direction could be measured and has been already actively compensated during the drops. Nevertheless, the compensation does not seem to be perfect. Furthermore, a certain degree of in-trap density oscillations is visible in the atomic ensemble after the decompression with the optimized ramp. A series of pictures with varying holding time in the decompressed trap followed by 100 ms of TOF have been recorded to examine these oscillations. The data is depicted in Fig. 6.18. The cloud shows clear size oscillations of the Thomas-Fermi radius in the z- and y'-direction.

To get an insight of the expected excitation spectrum of the density oscillations, we calculate the frequencies by applying the formalism introduced in Sec. 2.1.5. This formalism can be used to calculate the low-lying frequencies of the quadrupole, radial quadrupole as well as the breathing mode. Our trap configuration, however, does not show a single radial trapping frequency ω_r but rather two distinct radial trapping frequencies $\omega_y = 2\pi \cdot 27.9\,\text{Hz}$ and $\omega_z = 2\pi \cdot 24.6\,\text{Hz}$. Therefor, we use a mean radial trapping frequency $\omega_r = (\omega_y + \omega_z)/2 = 2\pi \cdot 26.25\,\text{Hz}$ to calculate the excitation fre-

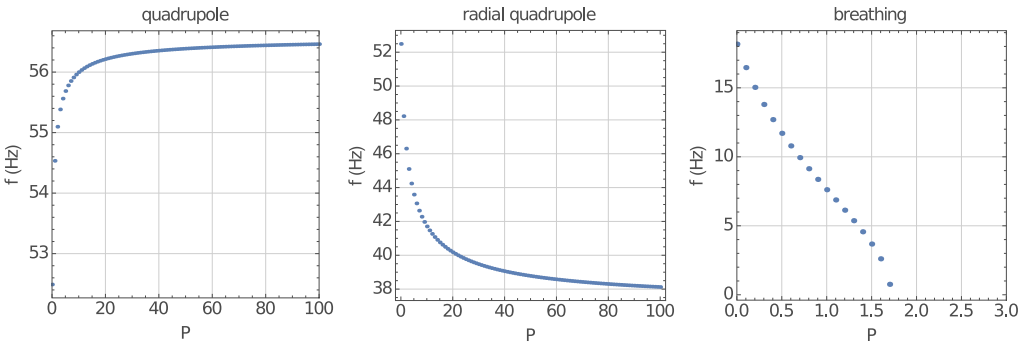

Figure 6.19: Theoretical prediction of the excitation frequency spectrum for a cigar-shaped trap with axial trapping frequency $\omega_x = 2\pi \cdot 9.1\,\mathrm{Hz}$ and radial trapping frequency $\omega_r = 2\pi \cdot 26.25\,\mathrm{Hz}$ depending on the interaction parameter P, which is in our case $P \approx 100$. The chosen trap frequencies resemble approximately the used trap configuration. The breathing mode is suppressed for increasing interactions.

quencies. The interaction parameter for our trap configuration and expected atom numbers calculates to $P \approx 100$. The expected excitation frequencies in dependence of the interaction parameter P are shown in Fig. 6.19. For the level of interactions expected in our experiment, the breathing mode is highly suppressed. The frequencies of the quadrupole and radial quadrupole mode equal $2\omega_r$ for a non-interacting Bose gas. At the onset of interactions, the quadrupole mode frequency increases slightly, while the radial quadrupole mode frequency drops to an asymptotic value of about $\omega_{rq} = 1.4 \cdot \omega_r$.

From these theoretical considerations, we can rule out the existence of a breathing mode for our used trap configuration. From the fit to the experimental data, we get oscillations frequencies of 54(3) Hz for the z-direction and 55(2) Hz for the y'-direction. Together with the fact that both oscillations are in phase we can conclude that the BEC is undergoing quadrupole oscillations in the holding trap. For the lensing sequence, the BEC has been held in the final trap after decompression for 18.46 ms. From looking at Fig. 6.18 we can see that at the time of switch-off, the cloud size in z- and y'-direction is maximal. Given a quadrupole oscillation this means that the size in x-direction is minimal after TOF. Thus, we can conclude that the kinetic energy in x-direction is minimal at the time of switch-off and consequently we observe a lower rate of expansion than predicted by the scaling approach.

6.4.8 Residual magnetic field gradients

The magnetic interaction potential is given by

$$V(\mathbf{r}) = m_F g_F \mu_B B(\mathbf{r}). \tag{6.35}$$

Therefor, a magnetic field gradient leads to a force accelerating the atoms depending on their internal properties like mass and m_F-state

$$\mathbf{F}(\mathbf{r}) = m \cdot \mathbf{a}(\mathbf{r}) = -\nabla V(\mathbf{r}) = -m_F g_F \mu_B \nabla B(\mathbf{r}). \tag{6.36}$$

Magnetic field gradients can thus lead to systematic effects in a dual-species atom interferometer measuring the differential acceleration. After release from the trap, the atoms are in a magnetic sensitive state and the two clouds experience a differential acceleration produced by the magnetic field gradient. Since we want to reduce the expansion rate of the ensemble by applying a magnetic lens, the atoms can only be transferred to magnetic in-sensitive state by an adiabatic rapid passage *after* the lens. Even after the atoms have been transferred into the $|m_F = 0\rangle$ state, they are still experiencing an acceleration generated by the quadratic Zeeman effect, which will contribute to a systematic error to the measured differential acceleration in a dual-species atom interferometer [33]. Hence, we are interested in the strength of residual magnetic field gradients in our experiment.

The influence of the magnetic gradients on the position of the atoms for a maximum TOF of 22 ms on ground is below the effective pixel size of our imaging system. Therefor, we rely on data taken during drop campaigns with increased TOF up to 1 s. We can extract the magnetic field gradient by measuring the position of clouds in different $|m_F\rangle$ states after varying TOF using Eqn. (6.36) to calculate the gradient from the observed acceleration. Data of the magnetic field gradient in z- and y'-direction for different drop campaigns are shown in Fig. 6.20. Several weeks span between each campaign. During the free evolution of the condensate, all chip structures had been disconnected by the programmable chip fuse and no technical changes were made to the apparatus to ensure consistency of the data throughout one campaign.

The data points 2 to 6 represent measurement series with exactly the same experimental setup. On measurement point 2, though, the usual magnetic quantization field in x-direction had been increased from a value of $B_x = 0.193\,\mathrm{G}$ to a strength of $B_x = 0.963\,\mathrm{G}$. This leads to a flipping of the gradient in y'-direction as well as a reduction of the gradient in z-direction. Since one can only expect an increase of the gradient when increasing the current in a single Helmholtz coil, we can conclude that the x-coil is compensating another second residual gradient. Anyhow, data points 3 to 6 show that the gradient stays relatively constant over several campaigns, given that no technical changes are done in the physics package. Within the last four campaigns the measured magnetic field gradients have a value of

$$\begin{aligned} \nabla B_z &= (-0.69 \pm 0.03)\,\mathrm{G\,m^{-1}}, \\ \nabla B_{y'} &= (-0.23 \pm 0.05)\,\mathrm{G\,m^{-1}}. \end{aligned}$$

The data point 1 was recorded with a setup in which the second detection had not been

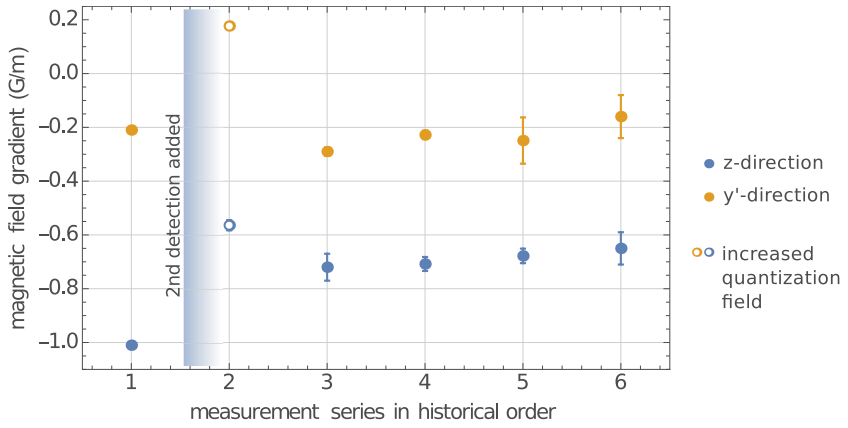

Figure 6.20: Measured magnetic field gradients over several drop campaigns in historical order: The biggest effect is caused by a change of the quantization field generated by the x-coil. The addition of the second imaging system contributed a small change to the gradient in z-direction. In general, the magnetic field gradients stay relatively constant as long as no changes are made to the standard experiment sequence or the technical setup inside the capsule.

installed yet. Furthermore, in contrast to all the other data points, the z-coil has not been disconnected during the TOF. Thus, it becomes evident that the disconnection of the z-coil and/or the installation of the second detection made a contribution to the present residual magnetic gradient in z-direction.

We can conclude that although care has been taken to reduce the strength of residual gradients by using an elaborated magnetic shielding concept as well as relying on non-magnetic materials inside the magnetic shield, a rather strong residual gradient is present within the vacuum chamber.

6.4.9 Center of mass motion

Apart from having an ultra-low mean expansion rate of the atomic ensemble, a well controlled center of mass motion of the ensemble is equally important for atom interferometric measurements with interrogation times of several seconds. Systematic effect contributions arise from atoms traveling along the transversal profile of the interferometry beams during the interrogation. Furthermore, the atoms should not leave the detection zone represented by the volume illuminated by the detection beam as well as the volume monitored by the absorption imaging or the fluorescence detection respectively.

In the experiment, the center of mass motion after the release is largely stipulated by the dipole oscillations of the condensate in the final trap. This contribution can be largely suppressed by switching off the trap at times, at which the atoms are at a turning point of the in-trap dipole oscillation. Furthermore, assuming a harmonic

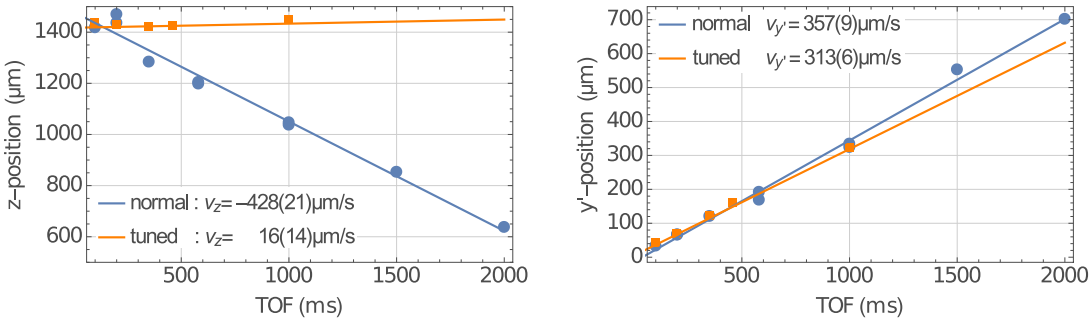

Figure 6.21: Center of mass motion (COMM) of the condensate after release from the trap: The COMM in z-direction could be minimized by tuning the BC current of the lens. In y'-direction a residual COMM remains, which can be partly attributed to a residual magnetic field gradient accelerating the atoms in the time between the release and the ARP.

lensing potential, the magnetic lens can contribute to the center of mass motion since a position mismatch between the atoms and the lens leads to a velocity contribution that is depending linearly from the atom-lens displacement.

The z-position of the lens can be adjusted by varying the base chip current. The position of a cloud lensed with base chip currents of $\{1.8, 1.82, 1.84\}$A has been evaluated and a linear interpolation was used to estimate the base chip current of 1.828 A that is optimal to reduce the COMM to a minimum. Due to this tuning, the trap frequencies of the lensing potential are reduced by about 2 % in the y- and z-direction equally. In Fig. 6.21 a comparison between the COMM of atoms lensed with a BC current of 1.8 A as well as a tuned lens with a BC current of 1.828 A is shown. The COMM in z-direction could be reduced to a level at which the scatter of the data points is becoming dominant. This scatter is mostly stemming from the anharmonicities in z-direction, which yield a larger uncertainty of about 10 µm for the evaluation of the position of the cloud. The following center of mass motion along z- and y'-direction has been achieved with the tuned lens position:

$$\begin{aligned} v_z &= (16 \pm 14)\,\mu\mathrm{m\,s^{-1}} \\ v_{y'} &= (313 \pm 6)\,\mu\mathrm{m\,s^{-1}} \end{aligned}$$

In the previous section, we calculated a magnetic field gradient of about $\nabla_{y'} B = -0.2\,\mathrm{G\,m^{-1}}$ in y'-direction. Between the release and the ARP the atoms thus would accumulate a velocity of $v_y = 138\,\mu\mathrm{m\,s^{-1}}$, which can partly describe the observed COMM in y'-direction. An observed residual oscillation in the y'-direction in the trap before the release with an amplitude of about 0.4 µm cannot contribute to a substantial COMM after the release. However, a kick induced by the switch-off of the magnetic trapping potential could be a plausible explanation.

7 Discussion and outlook

7.1 Laser system and electronics

The design, production and preparation of the laser system and in particular the laser system electronics posed to be one of the biggest work packages during the construction of the QUANTUS-2 experiment. Challenging requirements were defined by the drop tower environment regarding the mechanical stability, size, weight, power consumption as well as the optical output power and spectral fidelity of the laser system. In order to meet these requirements, novel technical key components were employed.

The second generation micro-integrated laser modules, produced by the FBH, were the first laser modules of this family ever used in a scientific setup. By proving their capabilities under harsh drop tower environment conditions, the way for future generation modules has been paved. Third generation modules relying on a similar integrated master oscillator power amplifier setup are already in use within the follow-up experiment MAIUS as well as the PRIMUS experiment [145]. As a most prominent new feature, the 3rd generation lasers come with on-board fiber coupling. Fourth generation laser modules, which are already in the production phase, will feature external cavity diode lasers instead of distributed feedback laser diodes as a master oscillator to reduce the linewidth of the emission spectrum. Additionally, they will be packaged in a hermetically sealed housing for better isolation from the environment and dust protection.

A critical subsystem that needed a great amount of treatment and optimization were the laser system electronics. QUANTUS-2 was the first experiment to make use of the novel compact electronics stack. Although, technically all cards performed as desired in a single test setup, the complete setup needed a substantial amount of debugging to make it work properly in conjunction with the physics package. One of the components that needed most attention, were the analog temperature controllers. In a next step they will be changed for commercial controllers [*Meerstetter*]. Also, the communication between the FPGA of the control computer and the electronics stack has proven to be a weak spot due to the deterioration of the clock signal on the bus when using stacks with many cards. A next generation interface offers communication between stack and control computer via an Ethernet protocol to solve this problem. Thanks to the close interaction and feedback from and to electronics designer Dr. Thijs Wendrich, the prototypes could mature to full operability. So far, there exist no commercial off-the-shelf replacements for most of the electronic components regarding the size of

the electronics.

The laser system was tested thoroughly before the integration into the physics package. A series of drop tests of single components from a miniaturized drop tower as well as drop and catapult campaigns of the complete rubidium laser system inside a test capsule at the drop tower in Bremen were performed. The optical power as well as the laser frequency locks proved to be extremely stable. The complete QUANTUS-2 laser system will feature a compact volume of 46 L, a low weight of 32 kg and a power consumption of about 300 W. All the executed performance tests qualified the laser system for the integration into the QUANTUS-2 experiment.

While future missions will rely heavily on the use of follow-up generation lasers and electronics based on technologies already qualified within QUANTUS-2, the used titanium free beam optomechanics are no longer envisaged to be a technical solution for follow-up laser systems. Although the mirror mounts and fiber couplers have proven to be sufficiently stable over many drops and weeks of operation, fiber- and Zerodur-based designs, which are used within the MAIUS sounding rocket missions, offer an increase in mechanical stability as well as a further reduction of the size and higher level of integration of the laser system [72].

7.2 Potassium upgrade

QUANTUS-2 was designed as a dual-species experiment. So far, experiments using exclusively rubidium have been conducted. The prospective potassium upgrade will include the installation of a dedicated second laser system for potassium. Furthermore, a potassium oven will be added.

Three stable potassium isotopes are available: the bosonic ^{39}K and ^{41}K and the fermionic ^{40}K. Bosonic ^{39}K features a negative scattering wavelength. The attractive interaction thus prohibits the formation of a stable ensemble. The scattering length could be tuned by a Feshbach resonance [146]. QUANTUS-2, however, does not feature the magnetic field creating Feshbach coils as well as an optical dipole trap which would be necessary to confine the atoms during the evaporation. Bosonic ^{41}K will be used most-likely since it can be prepared in a magnetic insensitive state. Direct RF evaporation from a magnetic trap with an efficiency comparable to ^{87}Rb has been observed [147]. Quantum degeneracy of ^{41}K and ^{87}Rb has been achieved in a common magnetic trap by microwave evaporation of rubidium and subsequent sympathetic cooling of potassium [148]. Fermionic ^{40}K is another candidate since it can be cooled to degeneracy by sympathetic cooling using ^{87}Rb as a coolant [149]. Experiments with Bose-Fermi mixtures in microgravity could be an interesting topic in the future.

In most instances, the potassium laser system is a mirror image of the rubidium system, sharing the comparable technological solutions with only minor modifications. The diode lasers have been produced to run on the potassium D_2 line at a wavelength of

767 nm. The spectroscopy cell of the master laser features a heating in order to increase the vapor pressure to facilitate frequency modulation spectroscopy. The ^{41}K D_2 level scheme features a hyperfine splitting of the excited state of just a few megahertz. Since the natural linewidth of the D_2 transition is about 6 MHz it is impossible to achieve a closed cooling transition cycle with low loss rates [150]. A repumper laser with a power comparable to the cooling laser is therefor necessary to transfer lost atoms back into the cooling cycle [123]. An additional tapered amplifier is installed in the distribution module to boost the repumper laser power. The Raman module for ^{41}K, in contrast, relies on a simplified scheme using just an acousto-optical modulator to create the phase-locked laser light. The laser system is already under construction and will again be tested in the drop tower in a dedicated laser system test capsule before integration into the experiment.

7.3 Simulation efforts

One of the key aspects when planning and conducting experiments on a microgravity platform, is the comprehensive simulation of the experiment sequence. This is especially valid for experiments conducted at the drop tower that offers only a low experiment repetition rate. Although, more than 200 drops have been performed, the data rate of the experiment is nevertheless extremely low. Thus, it has to be emphasized that the simulation of the magnetic interaction potential is essential for planning and evaluation of the drop campaigns. Achieved results include the gauging of the simulation to the experimental data taken in the lab before transfer of the apparatus to Bremen, over to cross-checking the results taken in microgravity as well as the simulation of the dynamics of the condensate when being transfered using tailored trajectories over a large distance. At its current state, the chip simulation delivers predictions that are in close agreement with the experimental results.

A big step forward in respect to the speed of the simulation will be made in the near future by translating the *Mathematica* code to *Python*. First routines are already working and the boost in speed will make it possible to achieve simulations in less then a tenth of the currently needed calculation time. The MAIUS sounding rocket missions are heavily depending on the chip simulation, due to the fact that there is no possibility to test the experiment in microgravity beforehand. For this reason, the results showing the applicability of the simulation as well as its optimization are extremely valuable.

7.4 Mobile high-flux source for ultra-cold atoms

The QUANTUS-2 experiment features a high-flux source for ultra-cold atoms in a mobile, compact and robust setup, which allows to conduct experiments in micrograv-

ity at the drop tower in Bremen. Unlike its predecessor experiment QUANTUS-1, it features the possibility to use the catapult mode of the drop tower, which doubles the microgravity time to 9 s. Initial accelerations during the catapult launch require a fast loading of the MOT directly after the catapult launch. One of the key technologies for achieving a high flux of ultra-cold atoms is the $2D^+$MOT, which provides a fast loading of the MOT in the science chamber. A three-layer atom chip in conjunction with Helmholtz coils allow for the production of the magnetic fields for the MOT as well as the Ioffe-Pritchard type magnetic traps with different geometries for a fast and efficient evaporation [79]. At its fastest cycle rate, the experiment can create a BEC within 850 ms with an atom number of 4×10^4. When producing BECs at a 1 Hz rate, atom numbers of 1×10^5 are achievable, which is one order of magnitude larger than the fastest BEC machine so far [124]. Furthermore, it is possible to create a BEC with a maximum atom number of about 4×10^5 within 1.6 s by using a slower evaporation sequence. This is by a factor of two faster than the fastest optical dipole trap BEC machine with comparable atom number.

After characterization of the atomic source and subsequent integration of the catapult-capable laser system into the physics package, the experiment was transferred to the drop tower in Bremen. In first drops and catapult flights, the mechanical robustness was tested. Accelerations of up to 43 g do not cause a degradation of the performance. The possibility to consecutively produce four BECs during one catapult flight has been demonstrated. The dynamics of the condensate were analyzed and compared with simulations. The reproducibility as well as the phase stability of the experimental sequence was shown by sampling an in-trap dipole oscillation of the condensate over 22 individual drops.

The fast transport of the condensate to ultra-shallow trapping potentials with harmonic oscillator frequencies of $\{\omega_x, \omega_y, \omega_z\} = 2\pi \cdot \{9.1, 27.9, 24.6\}$Hz was demonstrated by using a tailored shortcut decompression ramp. This allowed for a fast transport of the BEC over a distance of 1.2 cm within 150 ms, whereas a reduction of the excitation of in-trap dipole oscillations by a factor of 20 compared to a standard sigmoid-type decompression ramp was achieved. In the future, optimized transport ramps potentially will address not only the excitation of dipole oscillations but also density oscillations by introducing more control parameters to create even faster decompression ramps.

In total, over 210 drops and catapult flights have been conducted within the framework of this thesis.

7.5 Ultra-low expansion rates by using a magnetic lens

Atom interferometers measuring accelerations are limited in their sensitivity by the expansion rate of the interrogated atomic ensemble. Therefor, Bose-Einstein condensates are an excellent candidate for high-precision atom interferometry. Delta-kick

cooling has been introduced as a fast and atom number conserving technique to further lower the expansion rate of an atomic ensemble. A so-called magnetic lens, which is relying exactly on this technique, was used to further reduce the expansion rate of the BEC after the release from an adiabatically decompressed trap. In contrast to earthbound lab experiments, the microgravity environment permits a simultaneous magnetic lensing in all three dimensions because of the absence of gravity pulling the atoms away from the trap.

Two lensing schemes have been investigated within extensive drop campaigns. The first lens scheme relying on the science and base chip helped to understand many of the peculiarities emerging when using an atom chip for magnetic lensing. The eigensystem of the trap is rotating and translating when scaling the trap-generating currents, which leads to a rotated cloud after the lens. By pulsing the lens using a box function in time for the currents of the chips, the dynamics can be largely reduced. Furthermore, a reduction of the quantization field during the lens pulse leads to a minimization of the trap dynamics. Another important aspect when using atom chips for collimating atoms is the anisotropic trapping potential generated by the chip structures. The bias field has been carefully tuned to achieve a configuration with two equal trapping frequencies. It allows for a collimation of the ensemble in two directions. Finally, strong anharmonicities of the chip generated trapping potential deform the cloud shape and lead to a pronounced tail in the spatial density of the atomic ensemble. By using just the base chip and moving the atoms further away from the chip surface, the strongest cubic anharmonicities could be reduced by a factor of about three.

An improved lens was developed which takes all these findings into consideration. With the help of this so-called base chip lens, the expansion rate could be reduced to $\{\dot{\sigma}_x, \dot{\sigma}_y, \dot{\sigma}_z\} = \{104(33), 77.1(69), 87.6(18)\}\mu\mathrm{m\,s}^{-1}$. The corresponding one-dimensional temperatures are listed in Tab. 7.1. Values for achieved temperatures in a state-of-the-art 10 m atomic fountain setup in Stanford are listed for comparison. These have been achieved using a three-dimensional magnetic lens followed by an optical lens which works just in two directions [137, 151]. The magnetic lens presented within this thesis not only allows for effective temperatures that are on par with the ones achieved in [137], but also it features an effective temperature in the third direction that is lower by one order of magnitude.

The shape of the condensate, which is distorted by the anharmonicities, was analyzed using a Hermite-Gaussian decomposition to characterize the fundamental mode width of the condensate after the lens. The fraction of atoms in the fundamental (0,0) mode could be increased by about 12 % when compared to the initial science chip base chip lens.

In addition to the reduction of the expansion rate of the BEC, the center of mass motion of the condensate wave function in respect to the chip surface could be reduced below the position scatter of the data points. The magnitude of residual magnetic field gradients was calculated from the position of the lensed ensembles in different

T_{1D} in pK	10m fountain in Stanford	this work
x-direction	1600 ± 100	114^{+83}_{-61}
y-direction	40^{+40}_{-20}	62.1^{+12}_{-10}
z-direction	50^{+50}_{-30}	80^{+4}_{-3}

Table 7.1: Comparison of the achieved one-dimensional effective temperatures in this work and the state-of-the-art 10 m atomic fountain in Stanford [137, 151]. The achieved values are comparable in two directions. In the third direction, however, the effective temperature is lower by one order of magnitude in this work.

magnetic sensitive Zeeman states. These will be subject of further investigations since they are of fundamental interest regarding systematic effects in a subsequent atom interferometry sequence.

An interesting effect is arising from the self interference of the condensate after lensing with an anharmonic potential. The anharmonicities along the chip normal transform the phase space density to a banana-shaped form. Simulations show that for sufficient strong anharmonicities, fringes in the density profile of the cloud arise from the self interference of the BEC along the direction normal to the chip. While these fringes have not been observed so far, they could become visible with increasing time of evolution [152]. The implications on systematic effects in a subsequent atom interferometry sequence have yet to be discussed.

As of now, the magnetic lens applied within this thesis is not completely tuned for optimal collimation. The excitation of density oscillations in the final trap and their influence on the following magnetic lens was investigated. These oscillations can be used to reduce the kinetic energy of the weak lensed axial direction. The achievable minimum effective temperature depends on the ratio $(\sigma_0/\sigma_f)^2$ of the initial size of the ensemble at release and the size after the preTOF as well as the effective temperature of the released ensemble. For the used BC lens configuration, we have a ratio of $\sigma_0/\sigma_f = \{0.4, 0.077, 0.083\}$ for the three directions $\{x, y, z\}$ and an initial effective one-dimensional temperature of $T = \{0.13, 6.6, 5.6\}$nK of the released ensemble. This leads to a theoretical achievable minimum temperature of $T_{\min} = \{20, 39, 39\}$pK. The initial effective temperature of the released ensemble is fixed by the mean-field interaction energy in the chosen release trap configuration, whereas a prolongation of the preTOF would lead to an increased sampling of the anharmonicities. In a next step, a tuning of the lens strength will optimize the collimation and a deeper analysis of the in-trap density oscillations before the release could potentially allow for a reduction of the expansion rate below the aforementioned theoretical limit of delta-kick cooling.

7.6 Testing the equivalence principle

Once the apparatus has been upgraded with the second species and a simultaneous generation of two ultra-cold ensembles of each species is optimized, the differential acceleration can be read-out using a synchronous atom interferometer sequence. Therefor, the laser systems will provide the possibility to apply interferometry light pulses in a Raman as well as a Bragg scheme. The expansion rate of the cloud can be minimized to a large extent using the magnetic lens. Ultra-long times of free evolution between the interferometer pulses will result in a macroscopic separation of the interferometry arms. The time of free evolution is ultimately limited by the microgravity time lasting 9 s during a catapult flight. For a conservative estimation of the shot-noise limited acceleration sensitivity, we assume an atom number of $N = 100\,000$, an effective wave vector of $k_{\mathrm{eff}} = k_1 + k_2 \approx 4\pi/780\,\mathrm{nm}$ for rubidium, a pulse separation time of $T_{\mathrm{sep}} = 1\,\mathrm{s}$ and an interferometer contrast $C = 0.5$. The sensitivity then calculates to [56]

$$\Delta a = \frac{1}{\sqrt{N}} \frac{1}{C k_{\mathrm{eff}} {T_{\mathrm{sep}}}^2} = 3.9 \times 10^{-10}\,\mathrm{m\,s^{-2}}. \tag{7.1}$$

We have to assume that the atom number of the potassium interferometer will be lower than in the rubidium interferometer. Thus, the calculated uncertainty will be deteriorated by the potassium interferometer sensitivity, which has to be assumed to be lower. While systematics arising from wavefront aberrations or inefficient beam splitter pulses are to a large degree alleviated by the reduced expansion rate of the sample after magnetic lensing, expected systematic contributions are arising from BEC mean-field interactions [153]. These add to systematic effects caused by gravity gradients and residual magnetic field gradients [154].

7.7 Summary

The feasibility of a compact and robust source for ultra-cold atoms with a high atomic flux for high precision atom interferometry in microgravity was successfully demonstrated. As a key component, a laser system based on micro-integrated laser diode modules in conjunction with novel compact electronics was set up and qualified within nine drops and catapult flights with a dedicated laser system test capsule.

After the integration of the laser system into the physics package, the whole experiment was transferred to the drop tower in Bremen for extensive testing and subsequent studying and optimization of the cold-atom source in microgravity. The BEC source has been analyzed and optimized in its performance in over 210 drops and catapult flights. A fast transport of the BEC to an ultra-shallow magnetic trap using an optimized trajectory was used to reduce excitations of the condensate in the final trap.

The expansion rate of the released condensate was further reduced by means of a

magnetic lens, which is relying on a delta-kick cooling approach. A careful analysis and following optimization of the magnetic lens allowed for a substantial reduction of the expansion rate of the condensate. A Hermite-Gaussian decomposition was used to analyze the shape of the lensed ensemble and characterize the fundamental mode in three dimensions. Effective one-dimensional temperatures of less than 120 pK have been reached so far. This represents the lowest value ever achieved for three dimensions. To a great extent, the experiments conducted were benefiting from a magnetic field simulation program, which produced reproducible predictions of the physics.

Future experiments for testing fundamental physics in space will benefit from the technical and scientific results presented within this thesis.

Bibliography

[1] Claus Lämmerzahl. The search for quantum gravity effects I. *Appl. Phys. B*, 84:551, 2006.

[2] Vessot et al. Test of Relativistic Gravitation with a Space-Borne Hydrogen Maser. *Phys. Rev. Lett.*, 45:2081, 1980.

[3] M. E. Tobar, P. L. Stanwix, J. J. McFerran, and J. Gue. Testing local position and fundamental constant invariance due to periodic gravitational and boost using long-term comparison of the SYRTE atomic fountains and H-masers. *Phys. Rev. D*, 87:122004, 2013.

[4] Albert A. Michelson. The Relative Motion of the Earth and the Luminiferous Ether. *American Journal of Science*, 22:120, 1881.

[5] S. Herrmann, A. Senger, K. Möhle, M. Nagel, E. V. Kovalchuk, and A. Peters. Rotating optical cavity experiment testing Lorentz invariance at the 10ˆ-17 level. *Phys. Rev. D*, 80:105011, 2009.

[6] Loránd Eötvös. Über die Anziehung der Erde auf verschiedene Substanzen. *Mathematische und naturwissenschaftliche Berichte aus Ungarn*, 8:65, 1891.

[7] S. Schlamminger, K. Y. Choi, T. A. Wagner, J. H. Gundlach, and E. G. Adelberger. Test of the Equivalence Principle Using a Rotating Torsion Balance. *Phys. Rev. Lett.*, 100:041101, 2008.

[8] J. G. Williams, S. G. Turyshev, and D. H. Boggs. Progress in Lunar Laser Ranging Tests of Relativistic Gravity. *Phys. Rev. Lett.*, 93:261101, 2004.

[9] Abbott et al. Observation of gravitational waves from a binary black hole merger. *Phys. Rev. Lett.*, 116:061102, 2016.

[10] Louis de Broglie. *Recherches sur la théorie des quanta.* Thesis, University of Paris, 1924.

[11] R. Colella, A.W. Overhauser, and S.A. Werner. Observation of Gravitationally Induced Quantum Interference. *Phys. Rev. Lett.*, 34:1472, 1975.

[12] O. Carnal and J. Mlynek. Young's double-slit experiment with atoms: A simple atom interferometer. *Physical Review Letters*, 66(21):2689–2692, may 1991.

[13] L. Hackermüller, S. Uttenthaler, K. Hornberger, E. Reiger, A. Zeilinger, and M. Arndt. Wave Nature of Biomolecules and Fluorofullerenes. *Phys. Rev. Lett.*, 91:090408, 2003.

[14] M. A. Kasevich and S. Chu. Measurement of the Gravitational Acceleration of an Atom with a Light-Pulse Atom Interferometer. *Appl. Phys. B*, 54:321, 1992.

[15] E. L. Raab, M. Prentiss, A. Cable, S. Chu, and D. E. Pritchard. Trapping of Neutral Sodium Atoms with Radiation Pressure. *Phys. Rev. Lett.*, 59:2631, 1987.

[16] S. Chu, L. Hollberg, J. E. Bjorkholm, A. Cable, and A. Ashkin. Three-dimensional viscous confinement and cooling of atoms by resonance radiation pressure. *Phys. Rev. Lett.*, 55:48, 1985.

[17] Steven Chu. Nobel Lecture: The manipulation of neutral particles. *Rev. Mod. Phys.*, 70:685, 1998.

[18] L. Allen and J. H. Eberly. *Optical Resonance and Two-Level Atoms*. Dover Publications, 1987.

[19] Ch. J. Bordé. Atomic interferometry with internal state labelling. *Physics Letters A*, 140:10, 1989.

[20] M. Kozuma, L. Deng, E. W. Hagley, J. Wen, R. Lutwak, K. Helmerson, S. L. Rolston, and W. D. Phillips. Coherent Splitting of Bose-Einstein Condensed Atoms with Optically Induced Bragg Diffraction. *Phys. Rev. Lett.*, 82:871, 1999.

[21] A. Peters, K. Y. Chung, and S. Chu. High-precision gravity measurements using atom interferometry. *Metrologia*, 38:25, 2001.

[22] A. Peters, K. Y. Chung, and S. Chu. Measurement of gravitational acceleration by dropping atoms. *Nature*, 400:849, 1999.

[23] C. Freier, M. Hauth, V. Schkolnik, B. Leykauf, M. Schilling, H. Wziontek, H.-G. Scherneck, J. Müller, and A. Peters. Mobile quantum gravity sensor with unprecedented stability. *Journal of Physics: Conference Series*, 723:012050, 2016.

[24] http://www.muquans.com/index.php/products/aqg.

[25] http://aosense.com/solutions/gravimeter/.

[26] G. Tackmann, P. Berg, C. Schubert, S. Abend, M. Gilowski, W. Ertmer, and E. M. Rasel. Self-alignment of a compact large-area atomic Sagnac interferometer. *New J. Phys.*, 14:015002, 2012.

[27] Jeffrey Michael Mcguirk, G. T. Foster, J. Fixler, M. Snadden, and Mark Kasevich. Sensitive absolute-gravity gradiometry using atom interferometry. *Physical Review A*, 65(3), feb 2002.

[28] R. Bouchendira, P. Cladé, S. Guellati-Khélifa, F. Nez, and F. Biraben. State of the art in the determination of the fine structure constant: Test of Quantum Electrodynamics and determination of h/mu. *Annalen der Physik*, 525:484, 2013.

[29] G. Lamporesi, A. Bertoldi, L. Cacciapuoti, Marco Prevedelli, and Guglielmo M. Tino. Determination of the Newtonian Gravitational Constant Using Atom Interferometry. *Physical Review Letters*, 100(5), feb 2008.

[30] R. Geiger, L. Amand, A. Bertoldi, B. Canuel, W. Chaibi, C. Danquigny, I. Dutta, B. Fang, S. Gaffet, J. Gillot, D. Holleville, A. Landragin, M. Merzougui, I. Riou, D. Savoie, and P. Bouyer. Matter-wave laser Interferometric Gravitation Antenna (MIGA): New perspectives for fundamental physics and geosciences. In *E3S Web of Conferences*, page 01004, 2014.

[31] J. M. Hogan, D. M. S. Johnson, S. Dickerson, T. Kovachy, A. Sugarbaker, S. C. Peter, M. A. Kasevich, B. Saif, S. Rajendran, P. Bouyer, B. D. Seery, and L. Feinberg. An atomic gravitational wave interferometric sensor in low earth orbit (AGIS-LEO). *Gen. Relativ. Gravit.*, 43:1953, 2011.

[32] A. Bonnin, N. Zahzam, Y. Bidel, and A. Bresson. Simultaneous dual-species matter-wave accelerometer. *Phys. Rev. A*, 88:043615, 2013.

[33] C. Schubert, J. Hartwig, H. Ahlers, K. Posso-Trujillo, N. Gaaloul, U. Velte, A. Landragin, A. Bertoldi, B. Battelier, P. Bouyer, F. Sorrentino, G. M. Tino, M. Krutzik, A. Peters, S. Herrmann, C. Lämmerzahl, L. Cacciapouti, E. Rocco, K. Bongs, W. Ertmer, and E. M. Rasel. Differential atom interferometry with 87Rb and 85Rb for testing the UFF in STE-QUEST. *arXiv:1312.5963*, 2013.

[34] S. S. Szigeti, J. E. Debs, J. J. Hope, N. P. Robins, and J. D. Close. Why momentum width matters for atom interferometry with Bragg pulses. *New J. Phys.*, 14:023009, 2012.

[35] S. Chiow, T. Kovachy, H. Chien, and M. A. Kasevich. 102$\hbar$k Large Area Atom Interferometers. *Phys. Rev. Lett.*, 107:130403, 2011.

[36] Pierre Cladé. Bloch oscillations in atom interferometry. In *International School of Physics "Enrico Fermi"*, page 419, 2014.

[37] Albert Einstein. Quantentheorie des einatomigen idealen Gases. *Sitzungsber. phys.-math. Kl.*, page 261, 1924.

[38] Satyendranath Bose. Plancks Gesetz und Lichtquantenhypothese. *Z. Phys.*, 26:178, 1924.

[39] W. Ketterle, D. S. Durfee, and D. M. Stamper-Kurn. Making, probing and understanding Bose-Einstein condensates. In *Proceedings of the International School of Physics "Enrico Fermi"*, volume CXL, page 67, 1998.

[40] Fritz London. The λ-Phenomenon of Liquid Helium and the Bose-Einstein Degeneracy. *Nature*, 141:643, 1938.

[41] Charles E. Hecht. The Possible Superfluid Behaviour of Hydrogen Atom Gases and Liquids. *Physica*, 25:1159, 1959.

[42] H. J. Metcalf and P. van der Straten. *Laser Cooling and Trapping.* Springer, 2013.

[43] W. Ketterle and N. J. van Druten. Evaporative Cooling of Trapped Atoms. *Advances in Atomic, Molecular and Opticaal Physics*, 37:181, 1996.

[44] M. H. Anderson, J. R. Ensher, M. R. Matthews, C. E. Wieman, and E. A. Cornell. Observation of Bose-Einstein Condensation in a Dilute Atomic Vapor. *Science*, 269:198, 1995.

[45] K. B. Davis, M. O. Mewes, M. R. Andrews, N. J. Van Druten, D. S. Durfee, D. M. Kurn, and W. Ketterle. Bose-Einstein condensation in a gas of sodium atoms. *Phys. Rev. Lett.*, 75:3969, 1995.

[46] C. C. Bradley, C. A. Sackett, J. J. Tollett, and R. G. Hulet. Evidence of Bose-Einstein condensation in an atomic gas with attractive interactions. *Phys. Rev. Lett.*, 75:1687, 1995.

[47] Wolfgang Ketterle. Nobel lecture: When atoms behave as waves: Bose-Einstein condensation and the atom laser. *Rev. Mod. Phys.*, 74:1131, 2002.

[48] http://patapsco.nist.gov/imagegallery/details.cfm?imageid=193, NIST/JILA (public domain).

[49] J. G. Williams, S. G. Turyshev, and D. H. Boggs. Lunar laser ranging tests of the equivalence principle. *Class. Quantum Grav.*, 29:184004, 2012.

[50] B. Barrett, L. Antoni-Micollier, L. Chichet, L. Thomas, B. Battelier, T. Lévèque, A. Landragin, and P. Bouyer. Dual Matter-Wave Inertial Sensors in Weightlessness. *Nature Communications*, 7:13786, 2016.

[51] D. Schlippert, J. Hartwig, H. Albers, L. L. Richardson, C. Schubert, A. Roura, W. P. Schleich, W. Ertmer, and E. M. Rasel. Quantum test of the universality of free fall. *Phys. Rev. Lett.*, 112:203002, 2014.

[52] L. Zhou, S. Long, B. Tang, X. Chen, F. Gao, W. Peng, W. Duan, J. Zhong, Z. Xiong, J. Wang, Y. Zhang, and M. Zhan. Test of Equivalence Principle at 10-8 Level by a Dual-Species Double-Diffraction Raman Atom Interferometer. *Phys. Rev. Lett.*, 115:013004, 2015.

[53] P. Touboul, G. Métris, V. Lebat, and A. Robert. The MICROSCOPE experiment, ready for the in-orbit test of the equivalence principle. *Class. Quantum Grav.*, 29:184010, 2012.

[54] S. Dimopoulos, P. W. Graham, J. M. Hogan, and M. A. Kasevich. Testing General Relativity with Atom Interferometry. *Phys. Rev. Lett.*, 98:111102, 2007.

[55] J. Hartwig, S. Abend, C. Schubert, D. Schlippert, H. Ahlers, K. Posso-Trujillo, N. Gaaloul, W. Ertmer, and E. M. Rasel. Testing the universality of free fall with rubidium and ytterbium in a very large baseline atom interferometer. *New J. Phys.*, 17:035011, 2015.

[56] J. Williams, S. Chiow, N. Yu, and H. Müller. Quantum test of the equivalence principle and space-time aboard the International Space Station. *New J. Phys.*, 18:025018, 2016.

[57] Aguilera et al. STE-QUEST—test of the universality of free fall using cold atom interferometry. *Class. Quantum Grav.*, 31:159502, 2014.

[58] A. M. Nobili, M. Shao, R. Pegna, G. Zavattini, S. G. Turyshev, D. M. Lucchesi, A. De Michele, S. Doravari, G. L. Comandi, T. R. Saravanan, F. Palmonari, G. Catastini, and A. Anselmi. 'Galileo Galilei' (GG): space test of the weak equivalence principle to 10ˆ{-17} and laboratory demonstrations. *Class. Quantum Grav.*, 29:184011, 2012.

[59] X. Zhang, R. Pablo, T. Mazzoni, N. Poli, and G. M. Tino. Trapped-atom interferometer with ultracold Sr atoms. *Phys. Rev. A*, 94:043608, 2016.

[60] A. E. Leanhardt, T. A. Pasquini, M. Saba, A. Schirotzek, Y. Shin, D. Kielpinski, D. E. Pritchard, and W. Ketterle. Cooling Bose-Einstein Condensates Below 500 Picokelvin. *Science*, 301:1513, 2003.

[61] S. Chu, J. E. Bjorkholm, A. Ashkin, J. P. Gordon, and L. W. Hollberg. Proposal for optically cooling atoms to temperatures of the order. *Opt. Lett.*, 11:73, 1986.

[62] T. Lévèque, A. Gauguet, F. Michaud, F. Pereira Dos Santos, and A. Landragin. Enhancing the area of a Raman atom interferometer using a versatile double-diffraction technique. *Phys. Rev. Lett.*, 103:080405, 2009.

[63] E. Giese, A. Roura, G. Tackmann, E. M. Rasel, and W. P. Schleich. Double Bragg diffraction: A new tool for atom optics. *Phys. Rev. A*, 88:053608, 2013.

[64] H. Ahlers, H. Müntinga, A. Wenzlawski, M. Krutzik, G. Tackmann, S. Abend, N. Gaaloul, E. Giese, A. Roura, R. Kuhl, C. Lämmerzahl, A. Peters, P. Windpassinger, K. Sengstock, W. P. Schleich, W. Ertmer, and E. M. Rasel. Double Bragg Interferometry. *Phys. Rev. Lett.*, 116:173601, 2016.

[65] G. Stern, B. Battelier, R. Geiger, G. Varoquaux, A. Villing, F. Moron, O. Carraz, N. Zahzam, Y. Bidel, W. Chaibi, F. Pereira Dos Santos, A. Bresson, A. Landragin, and P. Bouyer. Light-pulse atom interferometry in microgravity. *Eur. Phys. J. D*, 53:353, 2009.

[66] https://de.wikipedia.org/wiki/Fallturm_Bremen (CC BY-SA 3.0).

[67] http://www.esa.int/spaceinimages/Images/2015/05/Air_Zero-g, Deutsches Zentrum für Luft- und Raumfahrt (CC-BY 3.0).

[68] http://www.dlr.de/rd/desktopdefault.aspx/tabid-9337/#gallery/23664, Deutsches Zentrum für Luft- und Raumfahrt (CC-BY 3.0).

[69] http://spaceflight.nasa.gov/gallery/images/shuttle/sts-133/html/s133e010447.html, NASA (public domain).

[70] http://coldatomlab.jpl.nasa.gov/mission/.

[71] J Grosse, S. T. Seidel, D. Becker, M. D. Lachmann, M. Scharringhausen, C. Braxmaier, and E. M. Rasel. Design and qualification of an UHV system for operation on sounding rockets. *Journal of Vacuum Science & Technology A*, 34:031606, 2016.

[72] V. Schkolnik, O. Hellmig, A. Wenzlawski, J. Grosse, A. Kohfeldt, K. Döringshoff, A. Wicht, P. Windpassinger, K. Sengstock, C. Braxmaier, M. Krutzik, and A. Peters. A compact and robust diode laser system for atom interferometry on a sounding rocket. *Appl. Phys. B*, 122:217, 2016.

[73] T. Könemann, W. Brinkmann, E. Göklü, C. Lämmerzahl, H. Dittus, T. van Zoest, E. M. Rasel, W. Ertmer, W. Lewoczko-Adamczyk, M. Schiemangk, A. Peters, A. Vogel, G. Johannsen, S. Wildfang, K. Bongs, K. Sengstock, E. Kajari, G. Nandi, R. Walser, and W. P. Schleich. A freely falling magneto-optical trap drop tower experiment. *Appl. Phys. B*, 89:431, 2007.

[74] Vogel et al. Bose-Einstein condensates in microgravity. *Appl. Phys. B*, 84:663, 2006.

[75] van Zoest et al. Bose-Einstein Condensation in Microgravity. *Science*, 328:1540, 2010.

[76] Müntinga et al. Interferometry with Bose-Einstein Condensates in Microgravity. *Phys. Rev. Lett.*, 110:093602, 2013.

[77] S. Abend, M. Gebbe, M. Gersemann, H. Ahlers, H. Müntinga, E. Giese, N. Gaaloul, C. Schubert, C. Lämmerzahl, W. Ertmer, W. P. Schleich, and E. M. Rasel. Atom-Chip Fountain Gravimeter. *Phys. Rev. Lett.*, 117:203003, 2016.

[78] Waldemar Herr. *Eine kompakte Quelle quantenentarteter Gase hohen Flusses für die Atominterferometrie unter Schwerelosigkeit.* Dissertation, Leibniz Universität Hannover, 2013.

[79] Jan Rudolph. *Matter-Wave Optics with Bose-Einstein Condensates in Microgravity.* Dissertation, Leibniz Universität Hannover, 2016.

[80] J. Rudolph, W. Herr, C. Grzeschik, T. Sternke, A. Grote, M. Popp, D. Becker, H. Müntinga, H. Ahlers, A. Peters, C. Lämmerzahl, K. Sengstock, N. Gaaloul, W. Ertmer, and E. M. Rasel. A high-flux BEC source for mobile atom interferometers. *New J. Phys.*, 17:065001, 2015.

[81] Alexander Grote. *Ultracold 87 Rb: from quantum metrology to two-photon ionisation.* Dissertation, Universität Hamburg, 2016.

[82] Tammo Sternke. *in preparation.* Dissertation, Universität Bremen, 2017.

[83] C.J. Pethick and H. Smith. *Bose–Einstein Condensation in Dilute Gases.* Cambridge University Press, 2002.

[84] F. Dalfovo, S. Giorgini, L. P. Pitaevskii, and S. Stringari. Theory of Bose-Einstein condensation in trapped gases. *Rev. Mod. Phys.*, 71:463, 1999.

[85] Eugene P. Gross. Structure of a Quantized Vortex in Boson Systems. *Il Nuovo Cimento*, 20:454, 1961.

[86] Lev P. Pitaevskii. Vortex Lines in an Imperfect Bose Gas. *Soviet Physics JETP*, 13:451, 1961.

[87] Y. Castin and R. Dum. Bose-Einstein Condensates in Time Dependent Traps. *Phys. Rev. Lett.*, 77:5315, 1996.

[88] Sandro Stringari. Collective Excitations of a Trapped Bose-Condensed Gas. *Phys. Rev. Lett.*, 77:2360, 1996.

[89] V. Pérez-García, H. Michinel, J. Cirac, M. Lewenstein, and P. Zoller. Low Energy Excitations of a Bose-Einstein Condensate: A Time-Dependent Variational Analysis. *Phys. Rev. Lett.*, 77:5320, 1996.

[90] Jakob Reichel. *Atom chips*. Wiley-VCH, 2011.

[91] David E. Pritchard. Cooling Neutral Atoms in a Magnetic Trap for Precision Spectroscopy. *Phys. Rev. Lett.*, 51:1336, 1983.

[92] H. Ammann and N. Christensen. Delta Kick Cooling: A New Method for Cooling Atoms. *Phys. Rev. Lett.*, 78:2088, 1997.

[93] W. Ketterle and D. E. Pritchard. Atom cooling by time-dependent potentials. *Phys. Rev. A*, 46:4051, 1992.

[94] Rudolph et al. Degenerate Quantum Gases in Microgravity. *Microgravity Sci. Technol.*, 23:287, 2010.

[95] Zentrum für angewandte Raumfahrt und Mikrogravitation. ZARM Drop Tower Bremen - User Manual, 2009.

[96] K. Dieckmann, R. Spreeuw, M. Weidemüller, and J. Walraven. Two-dimensional magneto-optical trap as a source of slow atoms. *Phys. Rev. A*, 58:3891, 1998.

[97] Thorben Könemann. *Konzeption, Entwicklung und Umsetzung von atomoptischen Fallturmexperimenten für den Einsatz unter Schwerelosigkeit am Fallturm Bremen*. Dissertation, Universität Bremen, 2009.

[98] M. Keil, O. Amit, S. Zhou, D. Groswasser, Y. Japha, and R. Folman. Fifteen years of cold matter on the atom chip : promise , realizations , and prospects. *Journal of Modern Optics*, 63:1840, 2016.

[99] R. Folman, P. Krüger, and J. Schmiedmayer. Microscopic atom optics: from wires to an atom chip. *Advances in Atomic, Molecular and Optical Physics*, 48:263, 2002.

[100] J. Reichel, W. Hänsel, and T. W. Hänsch. Atomic Micromanipulation with Magnetic Surface Traps. *Phys. Rev. Lett.*, 83:3398, 1999.

[101] Manuel Popp. *Compact, low-noise current drivers for atom chips*. Dissertation, Leibniz Universität Hannover, 2017.

[102] I. Geisel, K. Cordes, J. Mahnke, S. Jöllenbeck, J. Ostermann, J. Arlt, W. Ertmer, and C. Klempt. Evolutionary optimization of an experimental apparatus. *Appl. Phys. Lett.*, 102:214105, 2013.

[103] D. A. Smith, S. Aigner, S. Hofferberth, M. Gring, M. Andersson, S. Wildermuth, P. Krüger, S. Schneider, T. Schumm, and J. Schmiedmayer. Absorption Imaging of Ultracold Atoms on Atom Chips. *Optics Express*, 19:8471, 2011.

[104] M. Gilowski, C. Schubert, M. Zaiser, W. Herr, T. Wübbena, T. Wendrich, T. Müller, E. M. Rasel, and W. Ertmer. Narrow bandwidth interference filter-stabilized diode laser systems for the manipulation of neutral atoms. *Opt. Commun.*, 280:443, 2007.

[105] W. Zeller, L. Naehle, P. Fuchs, F. Gerschuetz, L. Hildebrandt, and J. Koeth. DFB Lasers Between 760 nm and 16 mum for Sensing Applications. *Sensors*, 10:2492, 2010.

[106] T.-P. Nguyen, M. Schiemangk, S. Spießberger, H. Wenzel, A. Wicht, A. Peters, G. Erbert, and G. Tränkle. Optimization of 780 nm DFB diode lasers for high-power narrow linewidth emission. *Appl. Phys. B*, 108:767, 2012.

[107] G. Bjorklund, M. Levenson, W. Lenth, and C. Ortiz. Frequency Modulation (FM) Spectroscopy. *Appl. Phys. B*, 32:145, 1983.

[108] taken from datasheet.

[109] M. Schiemangk, K. Lampmann, A. Dinkelaker, A. Kohfeldt, M. Krutzik, C. Kürbis, Al. Sahm, S. Spießberger, A. Wicht, G. Erbert, G. Tränkle, and A. Peters. High-power, micro-integrated diode laser modules at 767 and 780 nm for portable quantum gas experiments. *Appl. Opt.*, 54:5332, 2015.

[110] S. Spießberger, M. Schiemangk, A. Sahm, A. Wicht, H. Wenzel, A. Peters, G. Erbert, and G. Tränkle. Micro-integrated 1 Watt semiconductor laser system with a linewidth of 3.6 kHz. *Optics Express*, 19:7077, 2011.

[111] Max Schiemangk. *Ein Lasersystem für Experimente mit Quantengasen unter Schwerelosigkeit*. Dissertation, Humboldt-Universität zu Berlin, 2017.

[112] Malte Schmidt, Marco Prevedelli, Antonio Giorgini, Guglielmo M. Tino, and Achim Peters. A portable laser system for high precision atom interferometry experiments. page 8, jul 2010.

[113] Christoph Grzeschik. *Aufbau eines Rubidium–Ramanlasersystems für Atominterferometrie unter Schwerelosigkeit*. Diploma thesis, Humboldt-Universität zu Berlin, 2010.

[114] R. Hui, A. D'Ottavi, A. Mecozzi, and P. Spano. Injection Locking in Distributed Feedback Semiconductor Lasers. *IEEE Journal of Quantum Electronics*, 27:1688, 1991.

[115] Thijs Wendrich. *lasus.iqo.uni-hannover.de.* internal documentation, Leibniz Universität Hannover.

[116] K. G. Libbrecht and J. L. Hall. A low-noise high-speed diode laser current controller. *Rev. Sci. Instrum.*, 64:2133, 1993.

[117] Daniel A. Steck. Rubidium 87 D Line Data, 2001.

[118] Kai Lampmann. *Charakterisierung der mechanischen Stabilität optischer Komponenten für weltraumtaugliche Lasersysteme.* Bachelor thesis, Humboldt-Universität zu Berlin, 2010.

[119] Kai Lampmann. *Design , Aufbau und Test von Schlüsselkomponenten eines Lasersystems für Experimente mit Quantengasen auf einer Forschungsrakete.* Master thesis, 2012.

[120] Max Schiemangk. *Entwicklung ultrastabiler Lasersysteme für Experimente mit Quantengasen unter Schwerelosigkeit.* Diploma thesis, 2007.

[121] personal communication with Hauke Müntinga.

[122] T. G. Tiecke. Properties of Potassium, 2011.

[123] J. Catani, P. Maioli, L. De Sarlo, F. Minardi, and M. Inguscio. Intense slow beams of bosonic potassium isotopes. *Phys. Rev. A*, 73:033415, 2006.

[124] D. M. Farkas, E. A. Salim, and J. Ramirez-Serrano. Production of Rubidium Bose-Einstein Condensates at a 1 Hz Rate. *arXiv:1403.4641*, 2014.

[125] W. Petrich, M. H. Anderson, J. R. Ensher, and E. A. Cornell. Behavior of atoms in a compressed magneto-optical trap. *J. Opt. Soc. Am. B*, 11:1332, 1994.

[126] J. Dalibard and C. Cohen-Tannoudji. Laser cooling below the Doppler limit by polarization gradients: simple theoretical models. *Journal of the Optical Society of America B*, 6:2023, 1989.

[127] V. Schkolnik, B. Leykauf, M. Hauth, C. Freier, and A. Peters. The effect of wavefront aberrations in light-pulse atom interferometry. *Appl. Phys. B*, 120:311, 2015.

[128] G. Reinaudi, T. Lahaye, Z. Wang, and D. Guéry-Odelin. Strong saturation absorption imaging of dense clouds of ultracold atoms. *Optics Letters*, 32:3143, 2007.

[129] T. Kinoshita, T. Wenger, and D. S. Weiss. All-optical Bose-Einstein condensation using a compressible crossed dipole trap. *Phys. Rev. A*, 71:011602(R), 2005.

[130] J. C. Camparo and R. P. Frueholz. A dressed atom interpretation of adiabatic rapid passage. *J. Phys. B: At. Mol. Phys.*, 17:4169, 1984.

[131] Paul Berman, editor. *Atom Interferometry*. Academic Press, 1997.

[132] Mark Kasevich, David Weiss, Erling Riis, Kathryn Moler, Steven Kasapi, and Steven Chu. Atomic velocity selection using stimulated Raman transitions. *Physical Review Letters*, 66(18):2297–2300, may 1991.

[133] A. Louchet-Chauvet, T. Farah, Q. Bodart, A. Clairon, A. Landragin, S. Merlet, and F. P Dos Santos. The influence of transverse motion within an atomic gravimeter. *New J. Phys.*, 13:065025, 2011.

[134] F. M. H. Crompvoets, R. T. Jongma, H. L. Bethlem, J. A. van Roij, and G. Meijer. Longitudinal Focusing and Cooling of a Molecular Beam. *Phys. Rev. Lett.*, 89:093004, 2002.

[135] S. Goldberg, D. Strasser, O. Heber, M. L. Rappaport, A. Diner, and D. Zajfman. Phase-space manipulation of stored ions using the d-kick method. *Phys. Rev. A*, 68:043410, 2003.

[136] T. Aoki, T. Kato, Y. Tanami, and A. Morinaga. Delta-kick cooling using the loffe-Pritchard potential. *Phys. Rev. A*, 73:063603, 2004.

[137] T. Kovachy, J. M. Hogan, A. Sugarbaker, S. M. Dickerson, C. A. Donnelly, C. Overstreet, and M. A. Kasevich. Matter wave lensing to picokelvin temperatures. *Phys. Rev. Lett.*, 114:143004, 2015.

[138] E. Giese, W. Zeller, S. Kleinert, M. Meister, V. Tamma, and A. Roura. The interface of gravity and quantum mechanics illuminated by Wigner phase space. In *International School of Physics "Enrico Fermi"*, page 171, 2014.

[139] S. H. Myrskog, J. K. Fox, H. S. Moon, H. A. Kim, J. B. Kim, and A. M. Steinberg. Modified "delta kick cooling" for studies of atomic tunneling. *arXiv:quant-ph/9812031*, 1999.

[140] J. Söding, D. Guéry-Odelin, P. Desbiolles, F. Chevy, H. Inamori, and J. Dalibard. Three-body decay of a rubidium Bose–Einstein condensate. *Appl. Phys. B*, 69:257, 1999.

[141] Jean-Francois Schaff. *Shortcuts to adiabaticity for ultracold gases*. Thesis, Université Nice Sophia Antipolis, 2012.

[142] E. Torrontegui, S. Ibáñez, S. Martínez-Garaot, M. Modugno, A. Campo, D. Guéry-Odelin, A. Ruschhaupt, X. Chen, and J. G. Muga. Shortcuts to Adiabaticity. *Advances in Atomic, Molecular and Optical Physics*, 62:117, 2013.

[143] J. F. Mennemann, D. Matthes, R. M. Weishäupl, and T. Langen. Optimal control of Bose-Einstein condensates in three dimensions. *New J. Phys.*, 17:113027, 2015.

[144] X. Chen, A. Ruschhaupt, S. Schmidt, A. Del Campo, D. Guéry-Odelin, and J. G. Muga. Fast optimal frictionless atom cooling in harmonic traps: Shortcut to adiabaticity. *Phys. Rev. Lett.*, 104:063002, 2010.

[145] S. Kulas, C. Vogt, A. Resch, J. Hartwig, S. Ganske, J. Matthias, D. Schlippert, T. Wendrich, W. Ertmer, E. M. Rasel, M. Damjanic, P. Weßels, A. Kohfeldt, M. Luvsandamdin, E. Schiemangk, C. Grzeschik, M. Krutzik, A. Wicht, A. Peters, S. Herrmann, and C. Lämmerzahl. Miniaturized Lab System for Future Cold Atom Experiments in Microgravity. *Microgravity Sci. Technol.*, 2016.

[146] A. Adams, L. D. Carr, T. Schäfer, C. D. Errico, M. Zaccanti, and M. Fattori. holographic duality Feshbach resonances in ultracold 39 K. *New J. Phys.*, 9:223, 2007.

[147] T. Kishimoto, J. Kobayashi, K. Noda, K. Aikawa, M. Ueda, and S. Inouye. Direct evaporative cooling of K into a Bose-Einstein condensate. *Phys. Rev. A*, 79:031602(R), 2009.

[148] G. Modugno, G. Ferrari, G. Roati, R. J. Brecha, A. Simoni, and M. Inguscio. Bose-Einstein Condensation of Potassium Atoms by Sympathetic Cooling. *Science*, 294:1320, 2001.

[149] S. Aubin, S. Myrskog, M. H. T. Extavour, L. J. Leblanc, D. McKay, A. Stummer, and J. H. Thywissen. Rapid sympathetic cooling to Fermi degeneracy on a chip. *Nature Physics*, 2:384, 2006.

[150] M. Landini, S. Roy, L. Carcagn, D. Trypogeorgos, M. Fattori, M. Inguscio, and G. Modugno. Sub-Doppler laser cooling of potassium atoms. *Phys. Rev. A*, 84:043432, 2011.

[151] personal communication with Tim Kovachy.

[152] personal communication with Wolfgang Zeller.

[153] A. O. Jamison, J. N. Kutz, and S. Gupta. Atomic interactions in precision interferometry using Bose-Einstein condensates. *Phys. Rev. A*, 84:043643, 2011.

[154] J. M. Hogan, D. M. S. Johnson, and M. A. Kasevich. Light-pulse atom interferometry. In *Proceedings of the International School of Physics Course CLXVIII*, page 411, 2009.

List of Figures

Acknowledgements

I would like to express my deep gratitude to all the people that I worked with. First of all I would like to thank the QUANTUS-2 team consisting of Christian Deppner, Alexander Grote, Jan Rudolph, Tammo Sternke and Waldemar Herr. I was happy to share my inspiration as well as my motivation for making this experiment work with them. Even in the tough times during the preparation of the complete experiment as well as the strenuous drop tower campaigns with prolonged stays in a hotel far from home and friends, working with this team was always a pleasure. I wish all the best to the follow-up team members Merle Cornelius, Peter Stromberger and Julia Pahl and hope that they will experience the same spirit.

During the construction phase of the laser system as well as the qualification campaigns with the catapult test capsule, I was happy to work together with Kai Lampmann, Wojciech Lewoczko-Adamczyk and especially Max Schiemangk, who produced all the micro-integrated MOPA modules. They helped me to delve into the technical side of the laser system and provided a solid foundation that would withstand the drop tower environment and allow to achieve the scientific results presented in this thesis. I would like to thank Thijs Wendrich for helping me with the compact laser system electronics. Even at late hours in the lab in Hannover, he had the patience to help me with the integration and debugging of his prototype electronics. Further help with the electronics was provided by Sebastian Grede, Klaus Palis and Matthias Schoch. Mechanical components had to be often machined within a short time frame. My thanks are therefor going out to Thorsten Rausche and Christoph Kaiser at the workshop of the institute here in Berlin as well as the ZARM workshop in Bremen for their professional work.

During the drop tower campaigns our team could always rely on the expertise of the ZARM drop tower operations and service team. I would like to thank all of them, especially our personal flight assistants Ludger Burlage and Matthias Meyer as well as Deputy Technical Director Ulrich Kaczmarczik and Deputy Scientific Director Thorben Könemann who always kept an eye on the flight schedule for us.

I express my gratitude to Robin Corgier for providing the theory and calculation of the ramps for the optimized BEC transport. Cordial thanks go to Prof. Dr. Reinhold Walser who prepared the decomposition package for the analysis of the lensed atomic ensembles.

Furthermore, I want to express my deep thankfulness to Holger Ahlers, Dennis Becker, Naceur Gaaloul, Martina Gebbe, Sven Herrmann, Maike Diana Lachmann,

Hauke Müntinga, Manuel Popp, Dennis Schlippert, Stephan Seidel and the rest of the QUANTUS team. Thanks to their cordiality, I felt being a part of the family right from the beginning. I thank the head of the project Prof. Dr. Ernst Rasel for leading the collaboration and helping to form the QUANTUS-2 team. Also, I would like to thank the German Space Agency for the funding and especially Rainer Forke and Rainer Kuhl for constantly motivating us to push science into space. Many thanks go to Robin Corgier, Alexander Grote, Markus Krutzik, Vladimir Schkolnik and Prof. Dr. Reinhold Walser for proofreading my thesis in parts or as a whole.

I would like to thank my colleagues in Berlin, especially Aline Dinkelaker, Klaus Döringshoff, Christian Freier, Markus Krutzik, Moritz Nagel, Vladimir Schkolnik but also all the other members of the QOM and NANO group that made for a pleasant atmosphere. I am deeply indebted to my supervisor Prof. Achim Peters, who not only gave me the opportunity to work together with all these fine people and be part of this exciting collaboration, but also for giving me enough freedom to focus on my research.

Finally, all this would not have been possible without the endless support from my lovely parents. I also want to thank my friends and especially my brother who inspired me to study physics and who has been a companion since the very beginning.

Last, I want to thank Cate for being close to me all the time. Sei la mia vita!

Erklärung

Hiermit erkläre ich, dass ich die vorliegende Dissertation selbstständig und nur unter Verwendung der gemäß §7 Absatz 3 der Promotionsordnung der Humboldt-Universität zu Berlin vom 18.11.14 angegebenen Hilfen und Hilfsmittel angerfertigt habe.

Christoph Grzeschik, Berlin den 02.03.2017